

MASTER THESIS

Mitigating heat accumulation in a mid-size urban area: Applying micrometeorological flow-resolving simulations to assess climate effects of urban planning measures



Leyla Sungur

Student number: 1574910

supervised by

Prof. Dr. Christoph Thomas

Dr. Wolfgang Babel

Abstract

A multitude of demands is placed upon modern cities. To secure a save environment, cities should have a moderate urban climate which is linked to a series of micrometeorological processes. At night, cities can develop into an urban heat island. Strong anticyclonic influences increase these urban effects and cause cities to warm disproportionately high. Due to its heterogeneous structure, high differences can also show within cities during the diurnal cycle. These urban heat effects are stressful for the human body and cause health risks. The objective of this thesis was to validate the urban atmosphere LES model PALM4U by comparing against observation during the heat wave in 07.2019 and apply a series of simplified urban mitigation strategies. It was hypothesized that the simulation of PALM4U would show similar urban heat effects as in comparison to fine-grained observations from a sensor network in the simulation domain from previous studies. To investigate the effectiveness of city planning measures for heat mitigation, two scenarios were tested. It was expected that the addition of water inside the investigation area would induce lower air temperature at small spatial scale. It was furthermore expected that city air temperatures would increase under drought stress vegetation in those areas which normally benefit from evapotranspiration of green space. The results showed a replicability of the bioclimatic conditions through PALM4U. Both, perceived and air temperature showed a mean spatial difference of + 1K between the city and the surroundings. The urban heat island effect was strong with maximum afternoon temperature deviations of + 5.1 K for the inner-city. The addition of water surfaces led to the accumulation of cool temperature surfaces during daytime. For the diurnal cycle of the simulation, there was no impact on temperature on spatial scale. For the nocturnal cycle, the addition of water surfaces showed a small mitigating impact on the temperature and on spatial scale. This spatial scale varied in size dependent upon location. The application of drought stress caused stronger effects on air temperature during nighttime (+ 0.5 K). The spatial increase of air temperature for both, day- and nighttime was even distributed on the scale of the entire domain. Perceived temperature showed a concentration of heat for the core inner-city area during nighttime. As a local effect, cold air masses from the surroundings had a larger spatial effect on the cooling of air temperatures during nighttime than during daytime. It was concluded that the LES model approach proved to be a useful tool to investigate changes in urban planning.

Zusammenfassung

Das städtische Klima ist an eine Reihe mikrometeorologischer Prozesse gekoppelt und lokal sehr unterschiedlich. Bei warmen Temperaturen kann nachts ein urbaner Wärmeinsel Effekt entstehen. Starke antizyklonale Strömungseinflüsse verstärken solche urbanen Effekte und erwärmen diese zusätzlich, es können auch innerhalb der Stadt hohe räumliche Unterschiede entstehen. Das Ziel dieser Arbeit war es, das städtische Atmosphären-LES-Modell PALM4U durch den Vergleich mit Beobachtungen während der Hitzewelle am 07.2019 zu validieren und eine Reihe von vereinfachten Maßnahmen anzuwenden, welche das Stadtklima kühlen sollen. Es wurde erwartet, dass die Simulation von PALM4U ähnliche urbane Hitzeeffekte zu vergangenen Studien zeigen wird. Es wurden zwei Szenarien entwickelt. Zum Einen wurde erwartet, dass die Verdopplung der Wassermenge innerhalb des Untersuchungsgebietes eine Absenkung der Lufttemperatur auf kleiner räumlicher Skala bewirkt. Des Weiteren wurde erwartet, dass die Zuführung von Trockenstress sämtlicher Vegetation im Untersuchungsgebiet Lufttemperaturen innerhalb der Stadt in den Bereichen ansteigen lässt, die normalerweise von der Evapotranspiration von Grünflächen profitieren. Die Ergebnisse zeigten eine realistische Wiedergabe der bioklimatischen Bedingungen von PALM4U. Sowohl die gefühlte, als auch die Lufttemperatur zeigten eine mittlere räumliche Differenz von + 1K zwischen Stadt und Umland. Maximale Temperaturabweichungen am Nachmittag erreichten eine Differenz von + 5,1 K für die Innenstadt. Die Verdopplung von Wasserflächen führte zur Akkumulation kühler Temperaturflächen innerhalb des Modells. Tagsüber wurde kein Einfluss auf die vorherrschende Temperatur festgestellt. Für den nächtlichen Zyklus war ein leicht mildernder Einfluss auf die Temperatur zu beobachten. Die räumliche Skala hierfür variierte in ihrer Größe, in Abhängigkeit vom Standort. Die Anwendung von Trockenstress verursachte stärkere Auswirkungen auf die Lufttemperatur während der Nacht als am Tag (+ 0,5 K). Der räumliche Abweichung der Lufttemperatur war sowohl tagsüber als auch nachts gleichmäßig auf der räumlicher Skala der gesamten Stadt verteilt. Die gefühlte Temperatur zeigte eine Hitzekonzentration über den Stadtkern während der Nacht. Kalte Luftmassen aus dem Umland brachten einen größeren räumlichen Einfluss auf die Abkühlung der Lufttemperaturen in der Stadt während der Nacht als während des Tages. Zusammenfassend kann festgehalten werden, dass die LES-Simulation ein zuverlässiges Werkzeug zur Untersuchung urbaner Effekte darstellt.

Contents

Abstract	I
Zusammenfassung	III
1. Introduction	1
1.1. Motivation	1
1.2. State of the art research in urban climate effects and the urban heat island	3
1.3. Bayreuth as model city for mid-sized cities in Northern Bavaria	6
2. Objectives and research question	7
3. Methods	11
3.1. Large eddy simulation modeling for turbulent flows and its applicability for urban areas	11
3.2. PALM4U	14
3.2.1. Principles of PALM4U	14
3.2.2. PALM4U setup for Bayreuth	16
3.3. Data implementation to simulate heat effects in Bayreuth	18
3.4. Technical composition and adjustment of the domain	23
3.5. Synoptic forcing and micrometeorological conditions during heat wave 07.25.2019 – 07.28.2019 in Bayreuth	30
3.5.1. Observations from MiSKOR network	30
3.5.2. Near-surface weather as simulated by PALM4U	33
3.6. Net radiation and energy balance in cities: radiation- and energy transfer	37
3.7. Perceived temperature, potential temperature and air temperature to determine heat stress	42
3.8. Application of scenarios	43
4. Results and Discussion	50
4.1. Temperature distribution and anomalies in and around Bayreuth	50
4.2. PALM4U reproduction of physical magnitudes and micrometeorological conditions	56

4.3. Tested Scenarios	66
4.3.1. Scenario A	67
4.3.2. Scenario C	73
5. Conclusions	82
Acknowledgements	85
Bibliography	86
Appendices	93
A. PALM4U Model Description	93
B. Additional Figures and Tables	99

List of Figures

1. Bavaria covers the most southeastern region in Germany and holds a number of secondary mountain ranges. The south hosts its capital and becomes increasingly mountainous, bordering the Alps. The region of Bayreuth is located in Northern Bavaria. It is located in proximity to the mountain range of Fichtelgebirge in the northeast of the city of Bayreuth. The surroundings of Bayreuth are hilly, encompassing the Fichtelgebirge in the northeast and the Frankonian Switzerland in the southwest, where the river Roter Main originates 10 km from the city at 581 m NN. The city itself is divided by a ringroad marking the old downtown from the rest of the city. 7
2. Schematic showing the PALM4U submodel components that have been used for this study. Each submodel hosts different pieces of information and corresponding computation code for the model. PALM4U is composed of a set of the necessary, but also simulation-dependent submodels which can be activated by using their variables and placing their namelist in the parameter namelist file. 17
3. The structure of data for a simulation run with PALM4U can be divided into 3 sections: The preparation of input data for PALM4U, the execution and technical implementations to execute the run and the process of output generation and analysis. The hatching in grey symbolises the key points of adjustment for the computation of the scenarios compared to the base run. 18

4. The input data set of the static driver consists of several steps of data preparation and transformation under the application of various software. The hatched line in grey indicates the key steps where changes for the computation of scenarios are conducted. Data originates from the ADBV and was prepared suitably to be passed on into the PALM4U model. Scripts originating from the DLR had to be re-written or adjusted to undertake further processing steps, and the data rearranged into NetCDF formatted data. The merge routine in python format is responsible for combining all information gathered into one and again arranges the data into a priority scheme after which the single layers are ordered. It finally compiles the domains out of this data which comprise all information for the static driver. 21
5. This map represents a) the domain of 20 m resolution (covering an area of 16.2 km in x-direction and 13.5 km in y-direction) and b) the intended domain of 5 m resolution (covering 8.1 km in x-direction and 8.1 km in y-direction) which is part of the root domain. The intended inner domain was anticipated to resolve the inner-city structures of c) where the Hofgarten and the Maxstraße are located. At the same time, it shall encompass all residential and city structure areas of Bayreuth. The root domain however, was meant to serve as adjustment zone for the LES to LES nesting. In the adjusted version the root domain is used only, still encompassing b) and c) but at a resolution of 20 m. 23
6. Overview of the root domain in 20 m resolution by a scale of 1:72 000. This map displays all shapefile layers categorized after A4 that are requested by PALM. The composition of these layers is based on the prioritization scheme applied on the python routine, merging the single layers to one single NetCDF. 26

7.	Ensemble of the static driver input data of 20 m resolution as it is requested by the PALM4U model for further computation. Every input represents a single NetCDF files that originated from the shapefiles with data from the Amt für Digitalisierung und Vermessung (ADBV). a) vegetation type, b) water type, c) pavement type and d) building height, e) topography, f) soil type, g) building type, h) building ID. The legend labels show the bulk PALM code for the particular land-use class. Detailed images of building type and building ID are provided in the appendix (cf. Fig. B3).	27
8.	Schematic of the static driver for the inner domain of 5 m resolution to be nested into the root domain. Every domain needs to be equipped with its own static driver (cf. Fig. 7) that, depending on the chosen nesting approach, the domains may run seperately or in dependency from one another. As the child domains' geography is a compound of the root domain (cf. Fig. 5), both static drivers produce a very similar image. Slight differences are generated by the resolution size. The same files are shown as in 7.	28
9.	Original shapefile-cutout of the Maxstraße, Bayreuth.	29
10.	Implementation of the domain in a) shapefile format, b) 1 m resolution, c) 5 m resolution and d) 20 m resolution.	29
11.	20 m resolution domain after the adjustments and alterations of the static driver were carried out. Street canyon structures were forced by overlaying the pavement surface layer on top of the LOD2 housing layer.	30
12.	Mean of micrometeorological conditions between 07.25.2019 00:00 and 07.29.2019 00:00 from MiSKOR measurements in 10 minute intervalls. This graphic illustrates a) the prevailing potential temperature, b) wind-speed and c) incoming shortwave radiation, as a spatial mean over all 15 measurement stations of the Minderung staedtischer Klima- und Ozonrisiken (MiSKOR) network, d) incoming shortwave radiation for those stations that are located at an exposed site, namely Mistel, WilhelminenAue, St. Johannis, Eichelberg and Karstadt (cf. Fig. B2). The grey band indicates the standard deviation from every respective parameter.	32

13.	Wind roses for the mean of the period from 07.25.2019 00:00 to 07.28.2019 00:00. Windspeed and wind direction were extracted from the MiSKOR measurement sites at a) Maxstraße, b) Hofgarten, c) Kaemmereigasse and d) Wilhelminenaue, recorded in 10 minute means of instantaneous data.	33
14.	Schematic of a) mean potential temperature in Kelvin, b) mean windspeed in ms^{-1} and c) wind direction in degree averaged along the western, northern, eastern and southern side of the domain for the period from 07.25.2019 10:00 to 07.28.2019 00:00. The data was computed by a one dimensional spatial mean taken along the coordinates (E-UTM: 682524 - 688024, or N-UTM: 5532546 - 5537026) at the range of the domain, where the city of Bayreuth is located. The colours refer to the corresponding side of domain, whereas the black line indicates the respective mean of the MiSKOR measurement network data of Fig. 12.	34
15.	Time height cross sections of potential temperature (K) and specific humidity profile ($kgkg^{-1}$) for every domain boundary. The data was computed by a one-dimensional spatial mean taken along the coordinates (E-UTM: 682524 - 688024, or N-UTM: 5532546 - 5537026) at the range of the domain, where the city of Bayreuth is located.	36
16.	Schematic of parameters and mechanisms relevant for urban heating after (Spies, 2019). External factors that determine the potential for urban heating are presented in the upper part. The lower part illustrates city-internal, spatially variable factors responsible for site-specific heating. These are mainly given by the urban design.	40
17.	Map visualizing scenario A for the enlargement of the water surface of the Roter Main. A comparison between the base run and the scenario is shown. A second snippet shows the Annecy square which becomes flooded in scenario A.	44
18.	Visualization of scenario A (cf. Fig.17) in NetCDF, 20 m resolution, input into PALM. The legends display the bulk land-use type codes for PALM4U which belong to the files.	45
19.	Map of scenario B representing the city of Bayreuth with exclusively white roof painted housing.	46

20.	Visualization of scenario B (cf. Fig.19) in NetCDF, 20 m resolution, input into PALM. The legends display the bulk land-use type codes for PALM4U which belong to the files.	46
21.	Visualization of scenario C in shapefile format. The maps on the left site depict the cutout of the domain that is used for the analysis. The snippets on the right picture the versions C.1 and C.2 and the corresponding cut out of the base run.	47
22.	Visualization of scenario C (cf. Fig.21) in NetCDF, 20 m resolution, input into PALM. The legends display the bulk land-use type codes for PALM4U which belong to the files.	48
23.	Cross Sections in xz and yz dimension depicted from a domain cutout of the core area of Bayreuth. The white points indicate the coordinates where the profiles are taken.	49
24.	Overview of a) perceived temperature in °C at 16:00 CET, b) perceived temperature in °C at 4:30 CET, c) air temperature in Kelvin at 16:00 CET, d) air temperature in Kelvin at 4:30 CET. The plot area corresponds to the entire domain of the simulation.	51
25.	Overview of a) perceived temperature in °C at 16:00 CET, b) perceived temperature in °C at 4:30 CET, c) air temperature in Kelvin at 16:00 CET, d) air temperature in Kelvin at 4:30 CET. The plot area resembles a cutout of the entire domain of the simulation (cf. Fig. 23.	53
26.	Overview of a) the mean spatial deviation of perceived temperature in °C at 16:00 CET, b) the mean spatial deviation of perceived temperature in °C at 4:30 CET, c) the mean spatial deviation of air temperature in Kelvin at 16:00 CET, d) the mean spatial deviation of air temperature in Kelvin at 4:30 CET. The spatial mean was computed by neglecting the extent of Fig. 25 from Fig 24. This value was then subtracted from each pixel of Fig. 24 and plotted with a scale of the maximum difference values. The plot area resembles the entire domain of the simulation.	54

27.	Overview of a) perceived temperature in °C at 16:00 CET, b) perceived temperature in °C at 4:30 CET, c) air temperature in Kelvin at 16:00 CET, d) air temperature in Kelvin at 4:30 CET. The plot area resembles a cutout of the entire domain of the simulation.	55
28.	Overview of physical magnitudes of the output data for the base simulation of Bayreuth in 20 m resolution. a) perceived temperature in °C for the simulation at 16:00 CET, b) latent heat flux in Wm^{-2} simulated at 16:00 CET, c) sensible heat flux in Wm^{-2} simulated at 16:00 CET, d) perceived temperature in °C for the simulation at 4:30 CET, e) latent heat flux in Wm^{-2} simulated at 4:30 CET, f) sensible heat flux in Wm^{-2} simulated at 4:30 CET, g) outgoing longwave radiation flux in Wm^{-2} simulated at 16:00 CET, h) outgoing longwave radiation flux in Wm^{-2} simulated at 4:30 CET, i) outgoing shortwave radiation flux in Wm^{-2} simulated at 16:00 CET. A cutout of Bayreuth is presented.	57
29.	Simulated time height cross section and corresponding 2d profiles of the Ecological Botanical Garden. The profile was computed above a homogeneous grassland surface. The time period shows the 26-hour interval of 07.25.2019 from 10:00 CET to 07.26.2019 12:00 CET. The height is referenced to 0 NN from the lowest point of the domain, the profile data starts at the respective height of the profile location. The range of height is selected until the height, where the profiles develop a stable boundary layer. a) potential temperature in Kelvin, b) specific humidity in kgkg^{-1} , c) windspeed in ms^{-1} , d) wind direction in degree.	60
30.	Simulated time height cross section and corresponding and 2d profiles of St. Georgen. The profile was computed above a homogenous grassland surface. The time period shows the 26-hour interval of 07.25.2019 from 10:00 CET to 07.26.2019 12:00 CET. The height is referenced to 0 NN from the lowest point of the domain, the profile data starts at the respective height of the profile location. The range of height is selected until the height, where the profiles develop a stable boundary layer. a) potential temperature in Kelvin, b) specific humidity in kgkg^{-1} , c) windspeed in ms^{-1} , d) wind direction in degree.	64

31. Simulated time height cross-section and corresponding and 2d profiles of the Wilhelminenaue floodplain. The profile was computed above a homogenous grassland surface. The period shows the 26-hour interval of 07.25.2019 from 10:00 CET to 07.26.2019 12:00 CET. The height is referenced to 0 NN from the lowest point of the domain, the profile data starts at the respective height of the profile location. The range of height is selected until the height, where the profiles develop a stable boundary layer. a) potential temperature in Kelvin, b) specific humidity in kgkg^{-1} , c) windspeed in ms^{-1} , d) wind direction in degree. 65
32. Overview of absolute and difference magnitudes for scenario A. For the difference magnitudes d) - f), the base run matrix is subtracted from the scenario matrix. For the difference magnitudes g) - i), the spatial mean is calculated across the depicted cutout. a) perceived temperature in $^{\circ}\text{C}$ for the simulation at 16:00 CET, b) latent heat flux in Wm^{-2} simulated at 16:00 CET, c) sensible heat flux in Wm^{-2} simulated at 16:00 CET, d) Δ perceived temperature in $^{\circ}\text{C}$ for the simulation at 16:00 CET, e) Δ latent heat flux in Wm^{-2} simulated at 16:00 CET, f) Δ sensible heat flux in Wm^{-2} simulated at 16:00 CET, g) $\widehat{\Delta}$ perceived temperature in $^{\circ}\text{C}$ for the simulation at 16:00 CET, h) $\widehat{\Delta}$ latent heat flux in Wm^{-2} simulated at 16:00 CET, i) $\widehat{\Delta}$ sensible heat flux in Wm^{-2} simulated at 16:00 CET. The cutout represents the core of Bayreuth from the entire simulated domain. 67

33. Overview of absolute and difference magnitudes for scenario A at 4:30 CET. For the difference magnitudes d) - f), the base run matrix is subtracted from the scenario matrix. For the difference magnitudes g) - i), the spatial mean is calculated across the depicted cutout. a) perceived temperature in °C for the simulation at 4:30 CET, b) latent heat flux in Wm^{-2} simulated at 4:30 CET, c) sensible heat flux in Wm^{-2} simulated at 4:30 CET, d) Δ perceived temperature in °C for the simulation at 4:30 CET, e) Δ latent heat flux in Wm^{-2} simulated at 4:30 CET, f) Δ sensible heat flux in Wm^{-2} simulated at 4:30 CET, g) $\hat{\Delta}$ perceived temperature in °C for the simulation at 4:30 CET, h) $\hat{\Delta}$ latent heat flux in Wm^{-2} simulated at 4:30 CET, i) $\hat{\Delta}$ sensible heat flux in Wm^{-2} simulated at 4:30 CET. The cutout represents the core of Bayreuth from the entire simulated domain. 70
34. Schematic of the simulated change of magnitudes and their simulated spatial variability for scenario A. a) spatial variability of perceived temperature in °C for 16:00 CET, b) spatial variability of the latent heat flux in Wm^{-2} for 16:00 CET, c) spatial variability of the sensible heat flux in Wm^{-2} for 16:00 CET, d) spatial variability of perceived temperature in °C for 4:30 CET, e) spatial variability of the latent heat flux in Wm^{-2} for 4:30 CET, f) spatial variability of the sensible heat flux in Wm^{-2} for 4:30 CET, g) potential temperature difference of profiles taken at the Wilhelminenaue, h) potential temperature difference of profiles taken at the Annecy Square, i) potential temperature difference of profiles taken at the Roter Main. For the spatial variability magnitudes a) - f), the spatial mean is calculated across the depicted cutout and subtracted from the matrix of scenario A. For the difference magnitudes g) - i), the base run matrix is subtracted from the matrix of scenario A. The profiles were taken above water surface. 72
35. Comparison of simulated air temperature in Kelvin at 16:00, 20:30 and 04:30 CET for the base run and the scenarios. For scenario C, C.2 is taken as reference. The schematic depicts the cutout of the domain of range E-UTM: 682524 - 688024, N-UTM: 5532546 - 5537026 (cf. Fig. 23). . . . 74

36. Overview of total and difference magnitudes for scenario C.2. For the difference magnitudes d) - f), the base run matrix is subtracted from the scenario matrix of C.2. For the difference magnitudes g) - i), the spatial mean is calculated across the depicted cutout. a) perceived temperature in °C for the simulation at 16:00 CET, b) latent heat flux in Wm^{-2} simulated at 16:00 CET, c) sensible heat flux in Wm^{-2} simulated at 16:00 CET, d) Δ perceived temperature in °C at 16:00 CET, e) Δ latent heat flux in Wm^{-2} at 16:00 CET, f) Δ sensible heat flux in Wm^{-2} at 16:00 CET, g) Δ perceived temperature in °C at 16:00 CET, h) Δ latent heat flux in Wm^{-2} at 16:00 CET, i) Δ sensible heat flux in Wm^{-2} at 16:00 CET. The cutout represents the map of 21. 75
37. Difference magnitudes for the area and profiles between scenario C.2 and C.1. Scenario C.1 is subtracted from C.2. A) perceived temperature in °C simulated at 16:00 CET, b) latent heat flux in Wm^{-2} simulated at 16:00 CET, c) sensible heat flux in Wm^{-2} simulated at 16:00 CET, d) potential temperature profile in K at the Hofgarten, e) potential temperature profile in K at the Wilhelminenaue, f) potential temperature profile in K at the Maxstraße, g) specific humidity profile in K at the Hofgarten, h) specific humidity profile in K at the Wilhelminenaue, i) specific humidity profile in K at the Maxstraße. The cutout represents the map of 21. 76
38. Overview of the spatial distribution of the difference magnitudes for scenario C.2. Scenario C.2 represents all vegetated land surfaces as bare soil, except for the Hofgarten. For the difference magnitudes, the base run matrix is subtracted from the scenario matrix of C.2. The spatial mean is calculated for the difference magnitudes accross the depicted cutout. a) perceived temperature in °C for the simulation at 16:00 CET, b) latent heat flux in Wm^{-2} simulated at 16:00 CET, c) sensible heat flux in Wm^{-2} simulated at 16:00 CET, d) perceived temperature in °C at 04:30 CET, e) latent heat flux in Wm^{-2} at 04:30 CET, f) sensible heat flux in Wm^{-2} at 16:00 CET. The cutout represents the map of 21. 79

39.	Overview of absolute and difference magnitudes for scenario C.2 at 4:30 CET. For the difference magnitudes d) - f), the base run matrix is subtracted from the scenario matrix of C.2. For the difference magnitudes g) - i), the spatial mean is calculated across the depicted cutout. a) perceived temperature in °C, b) absolute latent heat flux in Wm^{-2} , c) absolute sensible heat flux in Wm^{-2} , d) Δ perceived temperature in °C, e) Δ latent heat flux in Wm^{-2} , f) Δ sensible heat flux in Wm^{-2} , g) Δ perceived temperature in °C, h) Δ latent heat flux in Wm^{-2} , i) Δ sensible heat flux in Wm^{-2} . The cutout represents the map of Figure 21.	80
A1.	Parameter namelist file steering the PALM4U Bayreuth simulation. Only parameters that deviate from the defaults need to be listed in the file. . .	98
B2.	Schematic after (Spies, 2019): Locations of the permanent meteorological measurements in Bayreuth. Highly sealed sites (orange): 1 Markt, 2 Kaemmereigasse, 3 St. Georgen, 6 Spinnerei, and 11 Karstadt; Vegetated sites (green): 7 Mistel, 8 Hofgarten, 9 Wilhelminenaue, and 10 Roehrensee; Housing areas (blue): 4 Altstadt and 5 Birken; Rural reference site: 12 EBG (map: OpenStreetMap)	99
B3.	Map of Detail for a) the static driver-building height, b) the static driver-building type. The building height stores information of the Level of detail 2 (LoD2) data, building type is a necessary information to steer the urban surfac module. Building type stores information about the age of the buildings.	100
B4.	Profile of specific humidity at one random exemplary location of each side of the model domain. The profiles show a more distinct form of the Urban boundary layer (UBL) than in Fig.15.	101
B5.	Simulated time height cross section of the very east of Bayreuth. The profile was computed above a cropland surface. The time period shows the 26-hour interval of 07.25.2019 from 10:00 CET to 07.26.2019 12:00 CET. The height is referenced to 0 NN from the lowest point of the domain, the profile data starts at the respective height of the profile location. a), b) potential temperature in Kelvin, c), d) specific humidity in kgkg^{-1} , e), f) windspeed in ms^{-1} , g) wind direction in degree	102

B6.	Simulated time height cross section of Bayreuth- Eichelberg. The profile was computed above a homogenous grassland surface. The time period shows the 26-hour interval of 07.25.2019 from 10:00 CET to 07.26.2019 12:00 CET. The height is referenced to 0 NN from the lowest point of the domain, the profile data starts at the respective height of the profile location. a), b) potential temperature in Kelvin, c), d) specific humidity in kgkg^{-1} , e), f) windspeed in ms^{-1} , g) wind direction in degree	103
B7.	Simulated time height cross section of the Mistelbach. The profile was computed above a homogenous water surface. The time period shows the 26-hour interval of 07.25.2019 from 10:00 CET to 07.26.2019 12:00 CET. The height is referenced to 0 NN from the lowest point of the domain, the profile data starts at the respective height of the profile location. a), b) potential temperature in Kelvin, c), d) specific humidity in kgkg^{-1} , e), f) windspeed in ms^{-1} , g) wind direction in degree	104
B8.	Simulated time height cross section of the very western part of Bayreuth. The profile was computed above a cropland surface. The time period shows the 26-hour interval of 07.25.2019 from 10:00 CET to 07.26.2019 12:00 CET. The height is referenced to 0 NN from the lowest point of the domain, the profile data starts at the respective height of the profile location. a), b) potential temperature in Kelvin, c), d) specific humidity in kgkg^{-1} , e), f) windspeed in ms^{-1} , g) wind direction in degree	105
B9.	Simulated time height cross section of absolute profiles taken for scenario A. The profiles of a) - f) were computed above a water surface. a) potential temperature in Kelvin above the Wilhelminenaue, b) potential temperature in Kelvin above the flooded Annecy square, c) potential temperature in Kelvin above the Roter Main, d) specific humidity in kgkg^{-1} above the Wilhelminenaue, e) specific humidity in kgkg^{-1} above the flooded Annecy square, f) specific humidity in kgkg^{-1} above the Roter Main. The time period shows the 26-hour interval of 07.25.2019 from 10:00 CET to 07.26.2019 12:00 CET. The height is referenced to 0 NN from the lowest point of the domain, the profile data starts at the respective height of the profile location.	106

B10. Differences of xy cross section data between scenario C.1 and C.2 and absolute profiles at 4:30 CET. For a)-c) C.1 is subtracted from C.2. a) perceived temperature in °C, b) latent heat flux in Wm^{-2} , c) sensible heat flux in Wm^{-2} , d) potential temperature Wilhelminenaue in Kelvin, e) potential temperature Hofgarten, vegetated, in Kelvin, f) potential temperature Hofgarten, bare soil, in Kelvin. The cutout represents the map of the Hofgarten in Fig. 21.	107
B11. Difference in perceived temperature in °C between the scenario and the base run for the simulation times of 16:00, 20:30, and 4:30 CET. The difference results from the subtraction of the base run from the scenario. Scenario A describes the changes induced by increasing the amount of water surface, scenario C.1 involves the application of the drought stress including the Hofgarten, scenario C.2 involves the application of drought stress excluding the Hofgarten.	108
B12. Difference of latent heat flux in Wm^{-1} between the scenario and the base run for the simulation times of 16:00, 20:30, and 4:30 CET. The difference results from the subtraction of the base run from the respective scenario.	109
B13. Difference of sensible heat flux in Wm^{-1} between the scenario and the base run for the simulation times of 16:00, 20:30, and 4:30 CET. The difference results from the subtraction of the base run from the respective scenario.	110
B14. Difference of the potential temperature in Kelvin between the scenario and the base run for the simulation times of 16:00, 20:30, and 4:30 CET. The difference results from the subtraction of the base run from the respective scenario.	111
B15. Difference of the outgoing longwave radiation flux in Wm^{-1} between the scenario and the base run for the simulation times of 16:00, 20:30, and 4:30 CET. The difference results from the subtraction of the base run from the respective scenario.	112
B16. Difference of the outgoing shortwave radiation flux in Wm^{-1} between the scenario and the base run for the simulation times of 16:00, 20:30, and 4:30 CET. The difference results from the subtraction of the base run from the respective scenario.	113

B17. Simulated time height cross section of absolute profiles taken for scenario C. The profiles were taken from a homogenous surface, a) potential temperature in Kelvin above the Wilhelminenaue, b) specific humidity in kgkg^{-1} above the Wilhelminenaue, c) potential temperature in Kelvin above the Maxstraße, d) specific humidity in kgkg^{-1} above the Wilhelminenaue, e) potential temperature in Kelvin above the Hofgarten, f) specific humidity in kgkg^{-1} above the Hofgarten (short grass), g) potential temperature in Kelvin above the Hofgarten (bare soil), h) specific humidity in kgkg^{-1} above the Hofgarten (bare soil). The time period shows the 26-hour interval of 07.25.2019 from 10:00 CET to 07.26.2019 12:00 CET. The height is referenced to 0 NN from the lowest point of the domain, the profile data starts at the respective height of the profile location. 114

List of Tables

2.	Setup of the root domain and its nested inner domain	22
A1.	Resampling method	93
A2.	Alignment of Landuse-Layers	93
A5.	List of parameter stored in the dynamic driver	93
A3.	List of minimum required COSMO-D2 parameter to initiate the dynamic driver	97
A4.	List of PALM4U classification	97
B6.	Computed Bowen Ratios for C.1, C.2 and the base run	99

List of Abbreviations

T	(K)	Air temperature
ADBV		Amt für Digitalisierung und Vermessung
AUHI		Atmospheric urban heat island
CFD		Computational fluid dynamics
COSMO-DE2		Consortium for small-scale modeling
DLR		Deutsches Zentrum für Luft- und Raumfahrt
DNS		Direct numerical simulation
DWD		German meteorological Service
ECBG		Ecological Botanical Garden
INIFOR		Mesoscale interface for initializing and forcing PALM
LES		Large eddy simulation
QSWS	(Wm ⁻²)	Latent heat flux
LoD2		Level of detail 2
LSM		Land surface model
MiSKOR		Minderung staedtdischer Klima- und Ozonrisiken
MOST		Monin-Obukhov similarity sheory
NetCDF		Network common data form
PERCT	(°C)	Perceived temperature
RANS		Reynolds average Navier Stokes
SHF	(Wm ⁻²)	Sensible heat flux
SGS		Subgrid scale
SUHI		Surface urban heat island

UBL	Urban boundary layer
UHI	Urban heat island

List of Symbols

Symbol	Unit	Description	Value
T	K	Absolute air temperature	
a_{ij}		Amplitude tensor	
Ω	rads^{-1}	Angular velocity of the earth	0.729×10^{-4}
Q_F	Wm^{-2}	Anthropogenic heat flux density	
T_{rural}	$^{\circ}\text{C}$	Average rural temperature surrounding an urban area	
T_{urban}	$^{\circ}\text{C}$	Average temperature urban area	
p	kgm^{-3}	Basic state density of dry air	
BO		Bowen Ratio	0-1
x_i	m	Coordinate on the cartesian grid ($x_1 = x, x_2 = y, x_3 = z$)	
f_i	s^{-1}	Coriolis parameter	
Δx	m	Equidistant grid spacing in x-direction	
Δy	m	Equidistant grid spacing in y-direction	
ux	m^3	Density of sensible heat/latent heat	
ρ	kgm^{-3}	Density of dry air (basic state)	
d	m	Diameter	
Π		Exner function	
ET	mms^{-1}	Evapotranspiration	
ρ	kgm^{-3}	Fluid density	
P	Pa	Fluid pressure	
u	u	Fluid velocity vector	
ϕ	Degree	Geographical latitude	
$u^{g,i}$	ms^{-1}	Geostrophic wind components ($u_{g,1} = u, u_{g,2} = v_g$)	
g	ms^{-2}	Gravitational acceleration	9.81
nx	pixel	Grid points in x direction	
ny	pixel	Grid points in y direction	
nz	pixel	Grid points in z direction	

Symbol	Unit	Description	Value
Δ	m	Grid spacing	
G	Wm^{-2}	Ground heat flux	
Fh	Wm^{-2}	Heat flux in z -direction	
$K \downarrow$	Wm^{-2}	Incoming shortwave radiation	
μ	m^2s^{-1}	Kinematic viscosity of air	1.461×10^{-5}
δ		Kronecker delta	
∇^2		Laplacian operator	
ρ^e	hPa	Modified perturbation pressure	
Q^*	Wm^{-2}	Net all-wave radiation flux	
ΔQ_A	m^2	Net heat advection	
ΔQ_S	J	Net heat storage	
$I \uparrow$	Wm^{-2}	Outgoing longwave radiation	
s	kgm^{-3}	Passive scalar	
ρ^*	hPa	Perturbation pressure	
π		Pi	3.14159
ρ_θ	kgm^{-3}	Potential density	
$theta$	K	Potential temperature	
P_r		Prandtl number in RANS parameterization	1
P	mm	Precipitation	
F	N	Random forcing term in parameterization of wave breaking	
ρ_0	hPa	Reference air pressure	1000
$\theta_{v,ref}$	K	Reference state of virtual potential temperature	
d	m	Resolution	
dx	m	Resolution in x -direction	
N_{Re}		Reynolds number	
ω	s^{-1}	Rotation of velocity	
χ_s	$\text{kgkg}^{-1}\text{s}^{-1}$	Sink term of s	
χ_{qv}	$\text{kgm}^{-3}\text{s}^{-1}$	Source term of q_v	
S_0	Wm^{-2}	Solar constant	1368

Symbol	Unit	Description	Value
X_{qv}		Source term of water mixing ratio	
\hat{T}	K	Spatial temperature distribution	
l_v	Jkg^{-1}	Specific latent heat of vaporization	2.5×10^6
R_d	$\text{Jkg}^{-1}\text{K}^{-1}$	Specific gas constant for dry air	287
R_v	$\text{Jkg}^{-1}\text{K}^{-1}$	Specific gas constant for water vapor	461.51
cp	$\text{Jkg}^{-1}\text{K}^{-1}$	Specific heat capacity of dry air at constant pressure	1005
P_0	mbar	Standard reference pressure	1000
u^s	ms^{-1}	Stokes drift velocity	
ΔS		Storage Change	
R	m^3s^{-1}	Streamflow	
e	$\text{m}^{-2}\text{s}^{-2}$	Subgrid-scale turbulent kinetic energy	
ΔT	K	Temperature Difference	
k	$\text{Jm}^{-1}\text{s}^{-1}\text{K}^{-1}$	Thermal conductivity	
t	s	Time	
E	Jm^{-2}	Total heat energy of surface layer	
Q_H	Wm^{-2}	Turbulent Sensible Heat Flux	
Q_E	Wm^{-2}	Turbulent Latent Heat Flux	
u_{*j}		Unscaled turbulent motions	
T_{UHI}	K	Urban Heat Island Effect	
V	ms^{-1}	Velocity	
u^i	ms^{-1}	Velocity components ($u_1 = u, u_2 = v, u_3 = \omega$)	
θ_v	K	Virtual potential temperature	
k		Von Kármán constant	0.4
qv	kgkg^{-1}	Water vapor mixing ratio	
U_s	ms^{-1}	Wave amplitude in Stokes drift parameterization	
$a\lambda$		Wavelength dependent absorbing capacity	
ϵ_λ		Wavelength dependent emissivity	
λ_{max}	μm	Wavelength with maximum power	

1. Introduction

1.1. Motivation

Global population growth and urbanization processes have led to increasing numbers of city residents worldwide. The degree of urbanization is expected to amount to above 60% of the global population by the year 2030 and exceed six billion people in 2050 (UN, 2018). By then, the overall population is expected to reach between 8.7 and 10.8 billion people (UN, 2018). Cities of today will need to cope with this increase in population, satisfying the rising infrastructural demands and displaying a healthy environment at the same time. Thus, urban areas evolve to play a crucial role for human wellbeing. Due to urban adaptations in response to high population density, heat effects are a growing environmental concern in cities around the world (Makido et al., 2019). The Urban heat island (UHI) effect was first recorded in an international comprehensive scientific work by (Landsberg, 1981) and (Oke, 1982), and further explained by subsequent studies (Shem and Shepherd, 2009; Peng et al., 2012; Debbage and Shepherd, 2015). It illustrates modified climate conditions compared to its surrounding area (Oke, 1982). The intensity of the UHI is generally defined as urban-rural temperature difference:

$$\delta T_{UHI} = T_{urban} - T_{rural} \quad (1)$$

Changed radiation patterns, reduced wind speed (Ossenbruegge and Bechtel, 2010), elevated rainwater discharge (Armson et al., 2013), lower plant transpiration and air humidity are reasons for the adjustments of the net energy balance to the net surface energy balance of an urban area and, at the same time, reasons for rising temperatures in cities (Rötzer et al., 2019). The surface energy balance of an urban area is written as

$$Q^* + Q_F = Q_H + Q_E + \Delta Q_s + \Delta Q_A \quad (2)$$

(Oke and Cleugh, 1987). Moreover, these impacts intensify as urban migration increases and other factors such as climate change are progressing. Global warming has driven more frequent, severe, and longer lasting excessive heat events worldwide (Mukherjee and Mishra, 2021). Future climate scenarios of Earth System Models depict the substantial increase in range of frequency and severity of drought and heat extremes. Therefore, adaption strategies are particularly effective in urban areas, where the infrastructural

setting exacerbates heat extremes on the one hand, and where the majority of people live on the other hand.

The importance of urban effects for society arises from the magnitude with which these patterns influence global population. Makido et al. (2019) claim that extreme heat events of the past have created major disturbances including infrastructure damage, economic loss, as well as human illness and death. The latter two have been shown to disproportionately impact vulnerable populations, such as the elderly, low-income and those with pre-existing health conditions. Each 1K increase of the temperature doubles the risk of death for elderly people (Buchin et al., 2016). Under very hot and humid conditions, the ability of the human body to regulate the core temperature and dissipate heat via sweat evaporation is reduced, provoking heat stress (Parsons, 2002). This is a health risk especially for people with respiratory or cardiovascular diseases. Additionally, there is an increased risk of pre-term birth during heat waves (Kloog, 2019). Other meteorological variables such as strong radiation or low wind speed can exacerbate heat stress. Urban residents are particularly vulnerable as they are exposed to a greater risk of heat stress and a higher mortality during a heatwave (Clarke, 1972; Hayhoe et al., 2010) compared with rural residents by reason of the UHI effect induced in urban areas. Coates et al. (2014) claim that extreme heat is the leading weather-related cause of death in highly urbanized countries such as the United States or Australia. The severe heat wave in Europe from August 2003 for example contributed to the death of around 40,000 people (García-Herrera et al., 2010). The compound stress that forms from urbanization, climate and climate change requires adaptation to these factors to become a priority in urban policies.

Due to the high amount of affected population worldwide a broad range of actors is needed to combat urban heat effects. Ensuring our built environment to be conducive towards safety and comfort is a critical political topic that does not only need attention within the frame of single cities, but moreover requires scientific guidance for policy makers on global, regional and local scales. On local scales, taking action is easier as concerned areas are smaller and thus transformation is expected to take place much faster. Research on local scale is most efficient, as the UHI depends on a series of factors such as geographical position, population size, topography, building geometry, building material and anthropogenic heat release (Mehrotra et al., 2019). Cities that share their

climate zone and do have equal numbers of population do not necessarily show a similar magnitude of the UHI effect. Cities can achieve extraordinary high or low effects due to their spatial and topographical setting or because they produce extreme anthropogenic heat release. Out of this urgency, the importance of city climate for human wellbeing is recognized by political authorities and state-owned institutions, cooperating with research institutions. Since cities are constantly growing and transforming in response to the residents' needs, a foresighted climate friendly infrastructure is not easy to establish. This is a niche for research to assess local climate effects and develop mitigation strategies by means of urban planning measures to counter heat stress in urban areas.

The city of Bayreuth (Bavaria, Germany) is expected to be one example for a mid-size urban area likely to suffer from elevated inner-city UHI effects in relation to its size. This expectation is based on findings by further research activity from Isabel Spieß and Andreas Tschuschke. The research project MiSKOR; 'Mitigation of urban climate and ozone risks' is investigating urban climate effects within Bayreuth. Its goal is to help the city council to undertake political decisions regarding future city planning measures. Not only will the city council be addressed to make use of these results, this thesis also shall also serve to benefit from less heat stress in summer time, ensuring a comfort temperature which contributes towards diminishing health risks as described above. Analyzing micrometeorological conditions in the city of Bayreuth, the use of high resolution urban climate simulation technology integrates in a series of recent applied models of the UHI in other cities (Feinberg, 2020; Juruš et al., 2016; Zhu et al., 2017). Today, building-resolving simulations are commonly used for this purpose and several models have been established in the scientific society (Maronga et al., 2019). Hence, this thesis combines the application of numerical simulation as a common methodology in environmental sciences, research on microclimate as part of natural sciences, and a transdisciplinary approach covering the environmental and societal interface.

1.2. State of the art research in urban climate effects and the urban heat island

The urban heat island is a very well-studied phenomenon. The first scientist ever to note such impact of anthropogenic climate modification was Luke Howard in 1833 (Mills, 2008). Howard's work recognized the effect of a city on its local climate, but the technical

methods he applied in his pioneer work were not scientifically documented. It was picked up by Chandler who advanced the measures of urban climate which resulted in a series of publications (Chandler, 1962, 1964; Chandler, 1967). The studies of Landsberg (1981) and Oke (1973, 1982) showed first process-based approaches and advanced the scientific knowledge about urban climate back in their day by analyzing its physical aspects and quantifying the relation between the degree of urban development and magnitude of the UHI. These authors did certainly provide a base for emerging studies and a growing scientific interest in this topic which has increased over the last decades as a consequence of the continuous concern about human thermal comfort, increment in energy demand, climate change impacts and their mitigation (Hebbert and Jankovic, 2013; Mills, 2014). Today, the UHI is one of the most studied effects in urban climatology (Memon et al., 2009; Rizwan et al., 2008; Stewart et al., 2011). Science has evolved from UHI studies on single cities to assessment and comparison of drivers or effects at global scale. Nowadays, UHI studies are so established as foundations to provide information for planning and policy making purposes, that they are commissioned by many city councils (Gonçalves et al., 2018). Latest progress includes adaptation constraints for individual urban areas over all continents (Cardoso et al., 2017; Sima et al., 2016) and the assessment of single UHI driving forces in individual cities (Edmondson et al., 2016; Liu and Morawska, 2020; Wang et al., 2016). Traditionally, two main approaches have been used to quantify urban climate effects. Creating a measurement network by on-site meters or vehicle-mounted sensors between urban and suburban or rural area reflects the Atmospheric urban heat island (AUHI). Here, representativeness remains questionable due to heterogeneous urban surface properties and comparatively insufficient data sources to reflect them (Hu and Brunsell, 2013; Spies, 2019; Tschuschke, 2019). Another approach is to investigate the remotely sensed urban heat island which is observed using thermal infrared data that allow us to retrieve land surface temperature. As close relationships between the near surface air temperatures and land surface temperature have been found, the Surface urban heat island (SUHI) is a reliable indicator of the AUHI. Furthermore, satellite remote sensing overcomes problems of in-situ measurements with wider sources, broader coverage, and steadier periodicity (Hu and Brunsell, 2013). However, remote sensing has its own limitations. The accuracy of land surface temperature products is highly dependent upon the cloud-screening algorithm (Hu and Brunsell, 2013; Letzel et al., 2008; Li and Wang,

2018; Xie and Castro, 2008, 2009). Thus, availability of data for a desired spatial domain and in preferred resolution can become difficult. Another issue for this approach is the measure and modeling of surface emissivities. A recent uncertainty analysis by Majozi et al. (2021) showed that the overall uncertainty of evaporation can reach 80 %. Among land surface and air temperatures, surface emissivity contributed the most to the solar net radiation uncertainty prevailing in remote sensing modeling. The major drawback, however, are the drivers of urban climate, that are related to atmospheric dynamics and hence cannot be displayed. These include horizontal advection of air temperature by prevailing winds and katabatic flows (Gardes et al., 2020). Besides observation approaches, computational techniques have advanced significantly over the past decades, representing mathematic models that are able to simulate urban climate behaviour. Several previous studies statistically predict urban climate effects using predictors characterising local meteorological conditions and/or urban morphology (Bernard et al., 2017; Makido et al., 2016). Numerical model simulation has evolved as a reference for computationally cheap statistical models to predict urban effects. One of the first simulations of city-induced thermal circulations was conducted by Delage and Taylor (1970). Researchers started making use of Computational fluid dynamics (CFD) models for simulating the city scale region (Veena et al., 2020). Urban climate models are especially useful to simulate demand oriented practical actions and enable to test changes in city infrastructure or input parameters. Hence, they also allow utilization for future or modified scenarios which is a big asset compared to observational measures. CFD models have been an emerging field for research globally and are widely used for urban thermal depiction today (Back et al., 2021; Wong et al., 2021). As Martilli (2007) already summarized, the rapid growth of urban populations is still continuing and the exponential increase of computational power is still rising, together with the scientific knowledge of the dynamics and thermodynamics of the urban atmosphere. This circuit has triggered a positive feedback between model applications, model development, and experimental campaigns, a feedback that is fundamental to the evolution of urban flow-resolving modeling (Martilli, 2007). There are two main types of such models: Large eddy simulation (LES) and Reynolds average Navier Stokes (RANS) both capture CFD. The ability of CFD models to reproduce microscale (e. g. building scale) airflow behaviour in urban areas has been tested extensively in the last years (Martilli and Santiago, 2009). LES models have proven

to be the best practise tool for city subgrid scale processes (Yang, 2014).

1.3. Bayreuth as model city for mid-sized cities in Northern Bavaria

This thesis aims at recording the urban effects, in particular air temperature hot spots, in a mid-size European area and identifying potential pathways for their mitigation. Furthermore, it will assess a set of realistic urban planning measures with the purpose to create a healthier climate for city inhabitants. This will be conducted by utilising numerical simulations using LES projection technology. The objective of this thesis is to investigate the location-specific changes in microclimate and turbulent transport by simulating selected structural changes in the land-use and land surface within the urban body of the city of Bayreuth. Bayreuth is located in northern Bavaria, Germany (cf. Fig. 1). It is situated at 344 m NN, within a wide valley surrounded by several hills with the largest elevation being the Schneeberg with 1.053 NN. Bayreuth has nearly 75000 inhabitants and an area of 67 km², being a medium-sized town (LfStat, 2019) in a rural area. Climate statistics show an annual average air temperature of 8.0 °C (1981-2010) and an average annual precipitation of 725 mm (1981-2010), measured at the Ecological Botanical Garden (ECBG) of Bayreuth (Mikrometeorologie, 2021). In the temperate zones, temperature and precipitation are negatively correlated at seasonal time scales during the warm season, favoring the occurrence of summers that are warm and mostly dry (Zscheischler and Fischer, 2020). High temperatures and deficits of precipitation both derive from anticyclonic conditions which preclude convection and lead to clear-sky conditions. Even the UHI seems to be more intense for some European cities under anticyclonic situations (Zak et al., 2020). The hot summer of 2018 in Germany is such an example, posing many challenges with regard to water shortages and yield losses, but also endangering human health. Quantifying the effects of such extremely hot and dry conditions is important for adaptation planning in urban design. Due to its location in a circular-shaped deep valley, the UHI for Bayreuth is assumed to reach higher magnitudes than other cities of its size. Few studies have been performed for mid-sized urban areas, while focus has been almost exclusively concentrated on large metropolitan areas. A network of 15 measurement stations placed throughout the city was implemented as part of the MiSKOR project and revealed an inner-city air temperature range of to up to 4.8K. For further details, the reader is referred to the work of (Lueers and Thomas, 2021).

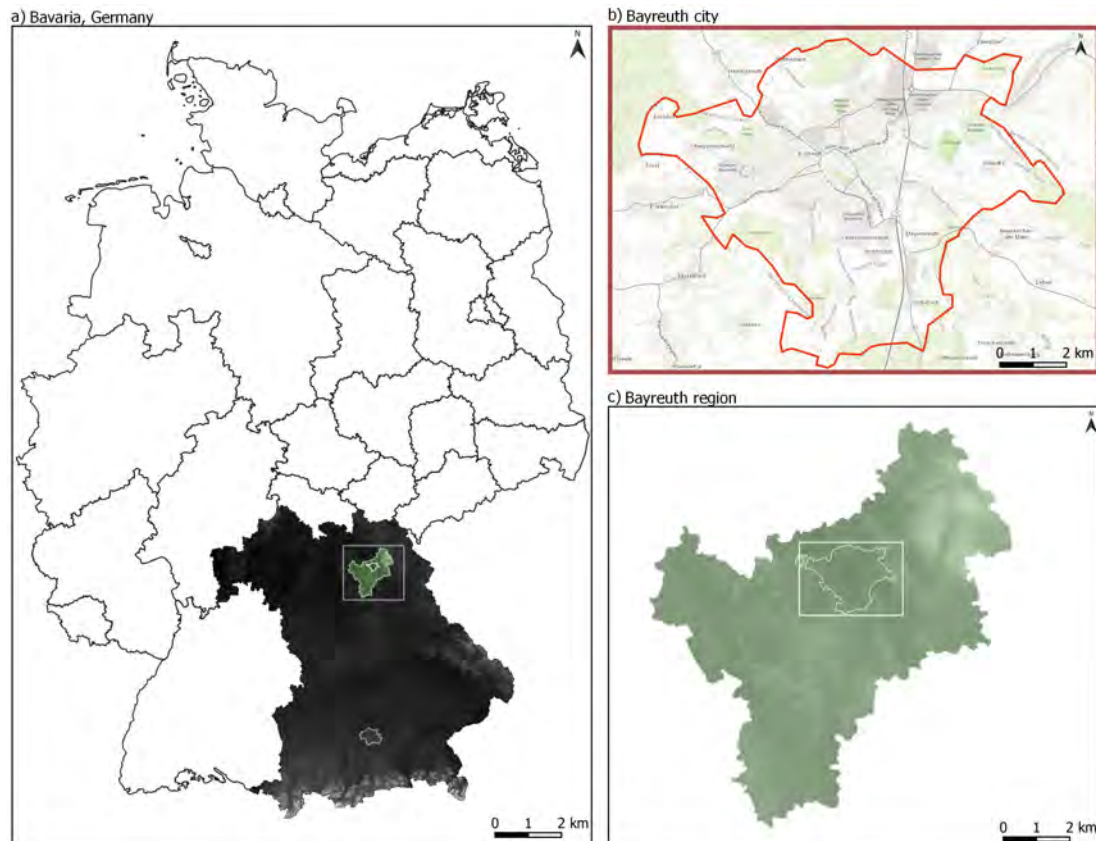


Figure 1: Bavaria covers the most southeastern region in Germany and holds a number of secondary mountain ranges. The south hosts its capital and becomes increasingly mountainous, bordering the Alps. The region of Bayreuth is located in Northern Bavaria. It is located in proximity to the mountain range of Fichtelgebirge in the northeast of the city of Bayreuth. The surroundings of Bayreuth are hilly, encompassing the Fichtelgebirge in the northeast and the Franconian Switzerland in the southwest, where the river Roter Main originates 10 km from the city at 581 m NN. The city itself is divided by a ringroad marking the old downtown from the rest of the city.

2. Objectives and research question

To complement the experimental findings on the work of the MiSKOR project, a modeling approach is chosen to illustrate and map the distribution of heat and further bioclimatic parameters within Bayreuth in a first step and compare it to a set of three scenarios, each resembling a city adaptation measurement. The first scenario shall replicate a cityscape with white roofs only, a second scenario shall investigate the effect of expanse of water on the surface energy balance by enlarging the water surface by a factor of 2. Thirdly, the effect of drought stress on city vegetation during a heat period shall be implemented. These scenarios are chosen based on their rather simple and easy technical

degree of practical implementation. Furthermore, already existing considerations by the city council are included, which encompasses a recultivation of the Roter Main, and an attempt has been made to translate them into simulation scenario A. An anticyclonic fennoscandian high leading to clear-sky conditions between 07.25.2019 and 07.26.2019, forming to a cyclonic fennoscandian high from 07.27.2019 until 07.28.2019 represented the warmest period in 2019 measured by air temperature. This period was chosen as input time period to show maximum effects during simulation.

The research is guided by the following research questions:

1. Does the computer simulation represent the biophysical responses in a meaningful fashion? Are the biophysical conditions generally meaningful?
2. What effect does a doubling of the water surface area within the investigation area have on the city air temperature? What spatial extent does this effect cover?
3. What effect does a white coat of paint on building roofs and exterior walls increasing the surface albedo have? What spatial extent around the modified surfaces does it cover?
4. What effect does drying of soil and vegetation, and the resulting drought stress have on city air temperatures? What spatial extent does it cover?
 - a) Including the Hofgarten
 - b) Excluding the Hofgarten

For each research question a hypothesis has been formed based on the current state of knowledge:

- i *PALM4U will show similar urban effects as the observations, taken by the MiSKOR project, have revealed.*

It is expected that the LES model is able to reproduce a biophysically meaningful representation of the city of Bayreuth in terms of physical output magnitudes through the implementation of original data considering synoptic forcing conditions and topography, building, and land-use data.

- ii *An enlargement of the water surfaces of the Roter Main will induce lower air temperature under anticyclonic weather conditions with small advective forcing at*

small spatial scale. The spatial impact on air temperature is expected to be larger for the Wilhelminenaue than the inner-city area by the Roter Main. The relative change of absolute temperature is expected to be higher for the inner-city area than the Wilhelminenaue.

This hypothesis is expected as the pavement surface will be exchanged for the water surface. The contribution of the landuse change from pavement to water in combination with an elevated amount (and daily period) of evapotranspiration over water is expected to influence the air temperature. The latent heat flux, which is the measure of the evapotranspiration, of the surface energy balance will be higher within the modified area, and is expected to prevent the air from heating up. As a consequence, the sensible heat flux will be lower resulting in the assumption that the Bowen ratio is smaller than before the manipulation. The Wilhelminenaue represents a highly vegetated area around the Roter Main compared to the inner-city area. Thus, the Bowen ratio is expected to be smaller at the Wilhelminenaue, but at the same time cooling effects on air temperature are expected to have a larger spatial impact on its surrounding area than the regulated discharge at the inner-city will. The relative amount of cooling of air temperature is expected to be higher for the inner-city area.

- iii *The implementation of white roofs in PALM4U for the respective domain of Bayreuth and during anticyclonic weather conditions with small advective forcing leads to less heating of the buildings and the surface, which in turn leads to a lower air temperature within the spatial extent of the entire urban area.*

Increasing the albedo of roof surface by approximately $\Delta 0.63$ through a white coat of paint will cause more incoming shortwave solar radiation to be reflected from the surface in the investigation area. This effect is especially pronounced under clear-sky conditions, where less backscattering of aerosol particles is expected. Increasing the roof albedo will show effect on nearly each grid cell that has urban area land cover. Therefore, a decrease of the mean air and surface temperature in Bayreuth is expected. Concerning the air temperature range within the city, highest differences are expected at the inner-city inside the Wittelsbacherring, in the neighbourhood of the train station and the industrial area north of Bayreuth.

- iiii *Drought stress will induce higher air temperatures in city quarters which normally*

benefit from evapotranspiration from vegetation. Drought stress simulations including the Hofgarten will cause higher Bowen ratios in the inner-city than drought stress simulations excluding the Hofgarten.

It is expected that drought stress of plants relates directly to lower transpiration of plants. Therefore, the latent heat flux in the surface energy balance is expected to be lower for drought stress scenarios. In response, a large corresponding increase in sensible heat flux will lead to much higher Bowen ratios. Consequently, the much-enhanced sensible heat flux leads to strongly rising air temperatures.

3. Methods

3.1. Large eddy simulation modeling for turbulent flows and its applicability for urban areas

Micro- and mesoscale meteorology is of particular interest for urban climate analysis: many weather phenomena with direct impact on human activities occur at this scale. Urban roughness, heat, pollution, and moisture effects on the atmospheric boundary layer (characterized as UBL) have important mesoscale implications (Nazarian et al., 2020). Numerical simulations of urban areas help to display this interplay of meteorological conditions. Hence, micro- and mesoscale models are important for the field of research of urban climate analysis and help to predict and manage urban heat distribution. However, local climate processes cannot be modeled using the regional mesoscale models due to their coarser spatial resolution hence urban heterogeneities cannot be resolved (Martilli, 2007). The anthropogenic processes occurring therein interact with the planetary boundary layer and produce a complex modeling problem. High-resolution modeling with fine grid resolution is imperative to resolve the unsteady and heterogeneous urban flow field. A system of non-linear partial differential equations can describe atmospheric motion (Galmarini et al., 2009). These equations are derived from thermodynamics and fluid mechanics called the Navier-Stokes equations. As an amplification of the Euler Equation, the Navier-Stokes Equation (cf. 3) introduced and improved viscosity to the computation of incompressible elastic fluids:

$$\frac{\partial u}{\partial t} + u \times \nabla u = -\frac{\nabla P}{\rho} + \nu \nabla^2 u \quad (3)$$

. As the majority of flows is turbulent, eligible CFD models are numerical models that solve the Navier-Stokes equations over small domains (few hundreds of meters at maximum), at high resolution (meters or less), and explicitly resolve buildings (Baklanov et al., 2009). However, complete solutions are obtained only for the case of simple two-dimensional flows. Complex vortices and turbulence that occur in three-dimensional fluid flows have proven yet insolvable to any but approximate numerical analysis methods up to this date. The most accurate attempt to represent turbulence flows in models would be the Direct numerical simulation (DNS), in which the full Navier-Stokes Equation is resolved. All scales, including the scale of smallest dissipative eddies called Kolmogorov-

microscale, need to be resolved by the numerical grid. This implies that all scales of eddy flows must be captured. Thus a very fine grid resolution is needed, resulting in very high computational effort. No modeling is required to capture the small-scale eddies, therefore no modeling bias prevails and the highest possible accuracy is reached. Due to this, DNS is only applied to very simple geometry and low Reynolds number flows (Yang, 2014) up until today. The Reynolds number is used to determine whether a fluid is laminar or turbulent, correlating the inertia forces to the viscous forces (Rehm et al., 2008).

$$N_{Re} = \frac{Vd}{\mu} \quad (4)$$

There is no exact Reynolds number that indicates the switch from laminar to turbulent flow. However, based on Reynolds' work the flow regime is typically divided into three cases: at values of 2000 and below, the flow profile is parabolic, between 2000 and 4000 the flow is in the transition region and a Reynolds number greater than 4000 indicates turbulent flow (LaNasa and Upp, 2014). Turbulent flow is three-dimensional and because increasing Reynolds numbers require smaller time steps, computational effort also increases. For this reason DNS is very unlikely to be applied for turbulent flows in the near future (Yang, 2014). Instead, it serves fundamental research to help understand turbulent flow behaviour. On the other hand, the before mentioned RANS approach parameterizes the turbulence and solves only the averaged quantities. This is especially useful for steady fluid flow leading to a great reduction in computational time (Martilli, 2007; Yang, 2014). There are different approaches for RANS modeling (direct modeling and modeling of Reynolds stress tensor via differential equation), but all are missing a satisfying overall validity for each flow type. Anyhow, RANS modeling has been the backbone in industrial CFD applications during the last decades (Yang, 2014) due to their modest computing requirements. The downside of ensemble average fields in modeling is that it lacks precision and thus fails to predict the flow behaviour plausibly. LES tries to fill this gap. It was first proposed by Smagorinsky (1963) for atmospheric flow prediction. The development until 1980 was rather slow, showing simple applications that were also used to serve engineering purposes (Schumann, 1975). LES gained use-cases and popularity when the computing power increased drastically throughout the 1990's and allowed the scientific community to operate increasingly complex flow simulations. This eventually led to the transition from RANS to LES technology as it became clear that RANS methods would not be able to handle complex turbulence flow problems

(Yang, 2014) and thus would not further develop for microscale usage. LES models solve time-dependent and spatially filtered Navier-Stokes equations and can parameterize effects of sub-grid features (Martilli, 2007). The prognostic equations for momentum, temperature, humidity, and other scalar quantities (such a chemical species) are solved and compared to RANS whereas LES does not conduct time- or ensemble-averaging. Used as microscale models, LES is able to explicitly resolve large eddies as far as small eddies by the principle of a separation of scales: large scale motions (large eddies) are computed directly whereas small scale motions (small eddies/ subgrid scale features) and their effect on large eddies are modelled. The small vortices originate out of the decay of the large vortices and thus lose information about boundary conditions or geometries, becoming more homogenous and isotropic. Due to this, model equations conceived for these rather independent small scale motions of boundary conditions are more favorable than within the RANS-context. At the same time they are significantly different to the DNS approach, saving much computational costs (Yang, 2014). Therefore, LES is not as computationally expensive as DNS but more accurate than RANS technology since it can capture in full detail large eddies which contain most of the turbulent energy and are responsible for most turbulent mixing and momentum transfer. However, its goal to combine the advantages of DNS and RANS only works with deductions regarding accuracy and numerical costs. LES ranges in the middle of both methods.

LES is state of the art for large domain runs at fine grid spacings. Therefore it is well suitable for modeling urban areas where individual elements in the urban canopy layer such as buildings, streets and trees are resolved individually (Li and Wang, 2018; Xie and Castro, 2009; Xie and Castro, 2006). To simulate urban climate, models need to have an adequate representation of the influence of the city on the exchanges with the atmosphere above. Here, the transport amount of subgrid scale features is very little due to quite neutral and convective stability conditions which accommodates the LES approach. Today, urban microscale models such as PALM/PALM-4U (Maronga et al., 2015; Maronga et al., 2019) are able to simulate city quarters at a grid spacing of 1 m and entire cities at 10 m.

3.2. PALM4U

3.2.1. Principles of PALM4U

The realisation of this study has been achieved by the use of the urban LES model PALM4U which was developed by the PALM group at the Institute of Meteorology and Climatology of Leibniz University Hannover, Germany (Maronga et al., 2015). PALM has been applied for approximately 20 years for simulating the atmospheric and oceanic boundary layer. Version 6, which is used for this study, has been equipped with so called PALM4U components to suit urban boundary layer related research and practical urban design (PALM4U) (Maronga et al., 2015). The PALM model system thus consists of the PALM core model and the PALM4U components. This section gives an overview of the PALM/PALM4U core governing equations and principles. The model is capable of solving two types of equations. First, non-hydrostatic, filtered, incompressible Navier–Stokes equations in Boussinesq-approximated form. It also solves the filtered Navier-Stokes Equation, based on a spatial scale separation approach of resolved scales and Subgrid scale (SGS) after Schumann (1975). Third, an anelastic approximation, in which the flow is treated as incompressible but allowing for density variations with height, while variations in time are not permitted (Maronga et al., 2015; Maronga et al., 2019; Raasch and Schroeter, 2001). Subsequently, PALM can simulate atmospheric phenomena taking place throughout the entire troposphere. By default, there are the following seven prognostic quantities: a passive scalar, the potential temperature, the subgrid-scale turbulent kinetic energy, the velocity components on a Cartesian grid, and the water vapor mixing ratio. Consequently, PALM computes the equation for the conservation of mass, momentum, thermal internal energy, moisture, and another arbitrary passive scalar quantity, as

$$\frac{\partial u_{j\rho}}{\partial x_j} = 0 \quad (5)$$

$$\frac{\partial \bar{u}_i}{\partial t} = -\frac{1}{\rho} \frac{\partial \rho \bar{u}_i \bar{u}_j}{\partial x_j} - \varepsilon_{ijk} f_j \bar{u}_k + \varepsilon_{i3j} f_3 u_{g,j} - \frac{\partial}{\partial x_i} \left(\frac{\pi^*}{\rho} \right) + g \frac{\bar{\theta}_v - \theta_{v,ref}}{\theta_{v,ref}} \delta_{i3} - \frac{1}{\rho} \frac{\partial}{\partial x_j} \rho (\overline{u''_i u''_j} - \frac{2}{3} e \delta_{ij}) \quad (6)$$

$$\frac{\partial \bar{\theta}}{\partial t} = -\frac{1}{\rho} \frac{\partial \rho \bar{u}_j \bar{\theta}}{\partial x_j} - \frac{1}{\rho} \frac{\partial}{\partial x_j} (\overline{\rho u''_j \theta''}) - \frac{l_v}{c_p \pi} \chi_{qv} \quad (7)$$

$$\frac{\partial \bar{q}_v}{\partial t} = -\frac{1}{\rho} \frac{\partial \rho \bar{u}_j \bar{q}_v}{\partial x_j} - \frac{1}{\rho} \frac{\partial}{\partial x_j} (\overline{\rho u''_j q''_v}) + \chi_{qv} \quad (8)$$

$$\frac{\partial \bar{s}}{\partial t} = -\frac{1}{\rho} \frac{\partial \rho \bar{u}_j \bar{s}}{\partial x_j} - \frac{1}{\rho} \frac{\partial}{\partial x_j} (\overline{\rho u''_j s''}) + \chi_s \quad (9)$$

Here, $i, j, k \in 1, 2, 3$ (cf. Eq. 6). The reference state $\theta_{v,ref}$ (cf. Eq. 6) can either be set to be the horizontal average θ_v , the initial state 0_v , or a fixed reference value. The other parameters of the symbols are specified in the list of symbols. PALM refines these equations over the volume on a Cartesian grid.

PALM employs a 1.5 order turbulence closure after Deardorff or alternatively, a dynamic SGS closure following Mokhtarpoor and Heinz for LES mode (Deardorff, 1980; Maronga et al., 2015; Mokhtarpoor and Heinz, 2017). Besides, PALM can also be run in DNS mode and two turbulence closures based on the Reynolds-averaged Navier–Stokes (RANS) equations are available for RANS mode parameterizing the full spectrum of turbulence. Boundary conditions are transformed by a constant flux layer assumption between the surface and the first computational grid level, following Monin-Obukhov similarity theory (MOST) (Monin and Obukhov, 1954). PALM assumes MOST to be locally applicable even though this is not proven. Nevertheless, surface heterogeneities can be described at the surface which is why MOST is a common LES model standard today (Maronga et al., 2019). Cyclic or non-cyclic lateral boundary conditions are available after Neumann (cyclic) or Dirichlet (non-cyclic). Non-cyclic lateral boundary conditions according to Dirichlet are either laminar and possess inflow properties characterised by time dependent turbulence or are generated by a synthetic turbulence generator. Outflow properties are characterised by radiation or turbulence outflow. The model domain is discretized in space by use of finite differences and equidistant horizontal grid spacings. The topography is Cartesian and based on a mask method, which resolves obstacles such as buildings or mountain ranges. Therefore, PALM obtains following simplifications:

- The obstacle shape must be of a full grid size; grid cells can either represent to be fluid or obstacle to their entire extent.
- Obstacles are permitted at to be mounted at the bottom only.
- Obstacles must be fixed and are not allowed to move.

Processes that occur on larger scales that affect the considered LES scales like pressure gradients via the geostrophic wind, horizontal advection of scalars, or processes of subsidence have to be prescribed by additional sources (Maronga et al., 2019; Raasch and Schroeter, 2001). Besides, PALM is equipped with several optional models which can be hooked up for individual purposes. These are respectively in alphabetical order: a

1D model for precursor runs, an aerosol model, an atmosphere-ocean coupling tool, a biometeorology module, a bulk cloud model, a chemistry model, an indoor climate model, a lagrangian cloud model, a lagrangian particle model, a Land surface model (LSM), large-scale forcing and nudging, a multi agent system, a plant canopy model, radiation models, self nesting and offline nesting, an urban surface model, and a wind turbine add-on (Maronga et al., 2019).

In return, PALM4U is compound of several special components shipped in some of the above listed submodels of PALM. These have been developed especially to suit modern UBL research and practical city planning for urban microclimate (Maronga et al., 2019). PALM4U enfolds land and surface representation, a radiative transfer scheme, a holistic indoor model to predict indoor temperature, a chemistry module displaying concentration fields that may react with each other, a multi-agent system for biometeorological assessment to statistically represent typical population groups, evaluation of biometeorological thermal indices and a nesting and coupling to the large scale model output of COSMOS.

3.2.2. PALM4U setup for Bayreuth

The previous section showed that PALM allows simulating various aspects of the boundary layer physics, whereas the PALM4U components have been added to suit explicitly state-of-the-art research within the UBL. The submodels used for this simulation approach can be seen in Figure 2. An initialization and runtime module are part of any run as they steer basic model operations and keep settings for input and output files. The modules steer in particular the LSM which encompasses information about land-use data for an area of 218 km² of Bayreuth and surroundings, for which cartographic basis was provided by the state office for geodesy of Bavaria ADBV. The static driver covers the information of the LSM and consists of a multi-layer soil model, predicting soil temperature and moisture content, and a solver for the energy balance at the surface. The LSM is linked to the nesting module where one root domain in 20m resolution, covering Bayreuth and surroundings, and one inner domain in 5 m resolution, covering the city core, implement the information of the LSM in a one way nesting mode. The LSM also drives the urban surface module which simulates building surface interactions using a tile approach. It consists of a multi layer wall and soil model, predicting wall and soil temperature and

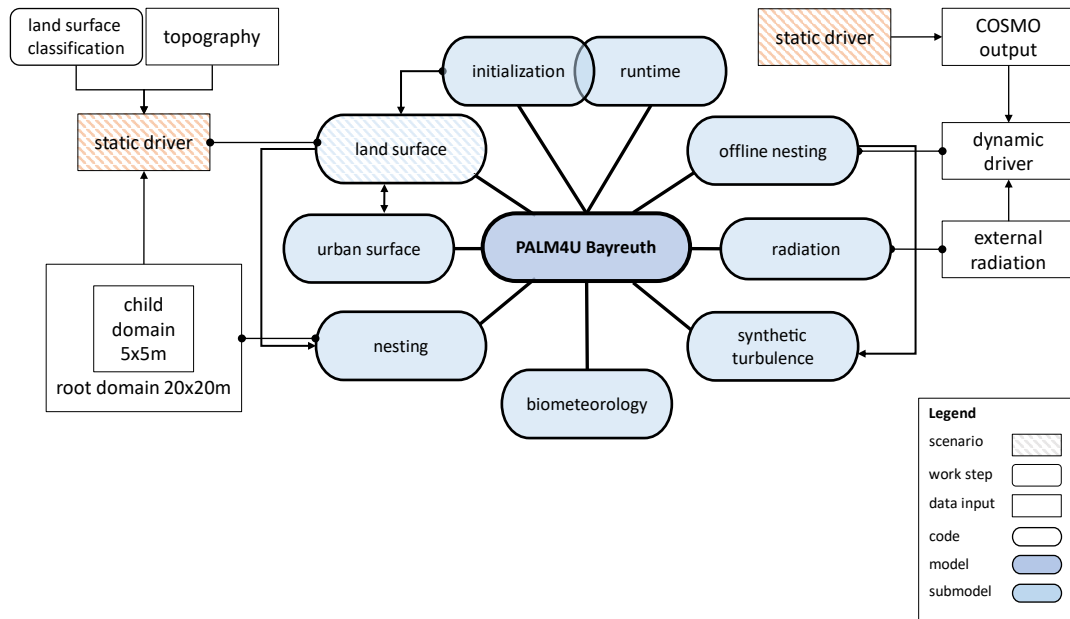


Figure 2: Schematic showing the PALM4U submodel components that have been used for this study.

Each submodel hosts different pieces of information and corresponding computation code for the model. PALM4U is composed of a set of the necessary, but also simulation-dependent submodels which can be activated by using their variables and placing their namelist in the parameter namelist file.

moisture content. A solver for the energy balance is applied to predict the temperature of the surface and the skin layer for each urban surface tile individually. In this simulation approach, a biometeorology module is added to enable the output of three thermal indices: Perceived temperature (PERCT), the universal thermal climate index, and the physiologically equivalent temperature, which all describe thermal stress of humans under the applied meteorological conditions.

The synoptic forcing conditions are provided externally. An offline nesting and radiation module are used that contain the process tool Mesoscale interface for initializing and forcing PALM (INIFOR). INIFOR allows PALM4U users to link the output data from the high resolution regional model Consortium for small-scale modeling (COSMO-DE2), designed by the German meteorological Service (DWD) for operational numerical weather prediction, to PALM. Together with the static driver and external radiation input by the radiation module, the dynamic driver is compiled.

3.3. Data implementation to simulate heat effects in Bayreuth

The composition of the model simulation designed for Bayreuth is exemplified in Figure 3. Input variables are distinguished between the static driver, the dynamic driver and the input parameter namelist. At first, a static driver needs to be developed. It

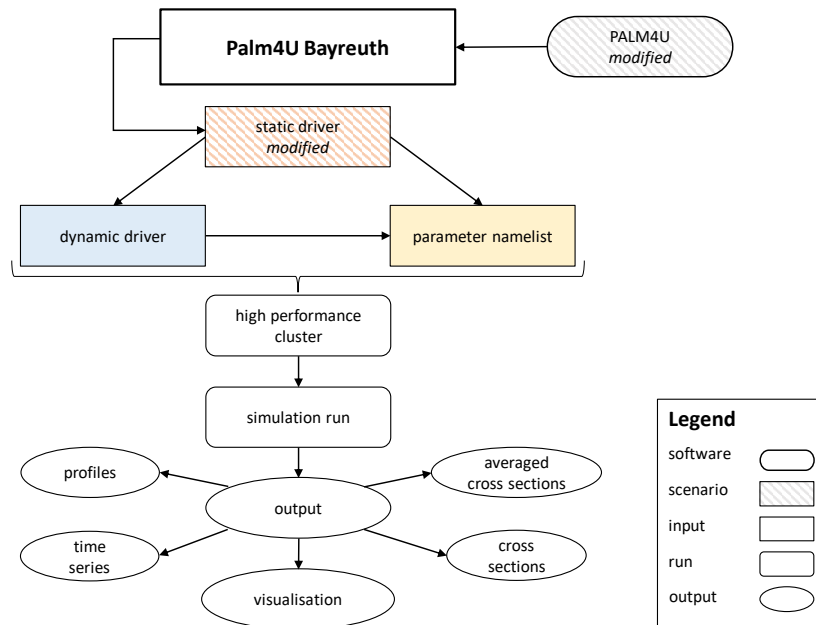


Figure 3: The structure of data for a simulation run with PALM4U can be divided into 3 sections: The preparation of input data for PALM4U, the execution and technical implementations to execute the run and the process of output generation and analysis. The hatching in grey symbolises the key points of adjustment for the computation of the scenarios compared to the base run.

encompasses the topography of Bayreuth as well as all additional necessary information files to identify and initialize all land- and urban-type surfaces in the model. In this study, the database consisted of digital terrain model (topographic map) that came as a shapefile with 1m resolution. Additionally, the database included land-use maps that distinguished vegetation, settlement areas, water bodies and areas dedicated to transportation. These four categories had a total of 36 more specific subcategories (cf. Tab. A4). The ADBV provided the data base for the simulation. LoD2 data in 1 m resolution was also acquired to reproduce the urban surface landscape of buildings in the model. Figure 4 shows in detail how the setup of the static driver works. A reclassification of proper land and water surfaces is necessary to implement PALM standard codes which define bulk parameters that can be read by the model for internal processing. The classes

settlement, water bodies, vegetation and recreation and transport set by the ADBV were reclassified into the PALM standard classes of water type, vegetation type and pavement type. A corresponding code was assigned for each subclass type. These codes assign the source scripts of PALM to compute main meteorological processes of the PALM source code. A soil type layer was added later in the processing. Detailed description of subcategories and their cartographic refurbishment can be checked in A4 in the appendix. One layer containing LoD2 building data was added in addition to the land-use cover, coded by a number for every building. A layer containing the building type, coded by the approximate age of the building, was also added. All other man-made structures such as bridges, sculptures or fountains, except buildings are ignored.

The data preparation process was guided by unix shell scripts provided by the Deutsches Zentrum für Luft- und Raumfahrt (DLR). In a first step, the shapefile data was georeferenced according the UTM WGS84 EPSG 25832 projection and clipped to the respective domain size by a reference shape of the topography domain size and rasterized. An alltouch-approach is used for the rasterization: as soon as one information partly touches one pixel cell, the whole pixel will be filled with this information. Shapefile data was converted to single NetCDF files in a second step. Afterwards, resampling was conducted to transfer the 1m resolution NetCDF files to a resolution of 20 m for the outer, larger domain of 218 km² and 5 m for the inner core domain of 65 km².

In regard to capturing the topographical effects on turbulence produced by the hilly area around Bayreuth, a 20 m resolution unit was chosen suitable to cover the whole domain. To simulate such a large domain by LES, the resolution needs to be able to resolve topographical features but also should not exceed computing power. The 5 m approach was defined for the simulation to resolve street canyons and detailed features of Bayreuth. To be able to do this, the inner domain was decreased to the approximate area of the city border of Bayreuth. The resampling method used for the aggregation of the new resolution varies per classification type (cf. tab. A1) and was computed per land-use type layer. The individual NetCDFs were then merged together into one single NetCDF file per domain, namely the static driver, comprising all information about the necessary input data by a python routine with its corresponding configuration file.

PALM requires exactly one piece of information per pixel and can therefore not process coordinates with missing information or multiple pieces of information. However, merging

with the alltouch approach causes the layers to overlap at many locations, which in turn leads to multiple pieces of information per coordinate. To avoid this, a prioritization scheme is applied inside the routine: building data, water bodies, pavement- and vegetation types were arranged in this exact order (cf. Tab. A2).

Finally, the final static driver consists of a spatial georeferenced topography information, serving as orographical ground base and setting the lowest point of the domain to 0 NN. In addition, a default soil type variable is set to a 'medium' grain size according to the European Centre for Medium-Range Weather Forecasts Integrated Forecasting System-classification. Spatial georeferenced variables of PALM4U land-use types (cf. tab. A4) are layed on top and subclassify the topographys' surface into respective codes that stand for the individual land cover. Variables that comprise building data (LOD2) complete the static driver. Additionally, the information about buildings for the static driver must also include a separate layer for the identification code for each building and an individual layer of information on the age of the buildings. Because this information is only needed to compute the inner-temperature of buildings, which was not part of this study, all buildings were set to a default age-class of 1950 - 2000. (Maronga et al., 2019).

The static driver feeds into the dynamic driver which is prepared separately. By including the dynamic driver into the model setup, changes in synoptic conditions can be considered. This is done by nesting the model domain within the larger-scale COSMO-DE2 model (offline nesting). Large scale synoptic forcing information of the atmosphere are transferred to PALM4U to steer internal processes. The meteorological fields of the velocity components, specific humidity and potential temperature, perturbation pressure, soil moisture and soil temperature for the simulation period were taken from the COSMO-DE2. The hourly COSMO-DE2 model output was converted from binary data to NETCDF format. The processing tool INIFOR then computed the resulting dynamic driver by interpolating the COSMO-DE2 grid and parameters into PALM-readable boundary data. This way, PALM can go without the need of measurement data. As there is no linkage possible between the radiation data provided by the COSMO-DE2 model and PALM4U, solar shortwave radiation data was acquired by the station in the ECBG, and added to the dynamic driver after compilation.

The COSMO-DE2-originated soil moisture in the dynamic driver revealed a sharp gradient later in the testrun. Therefore, soil moisture data had been extracted from the ECBG

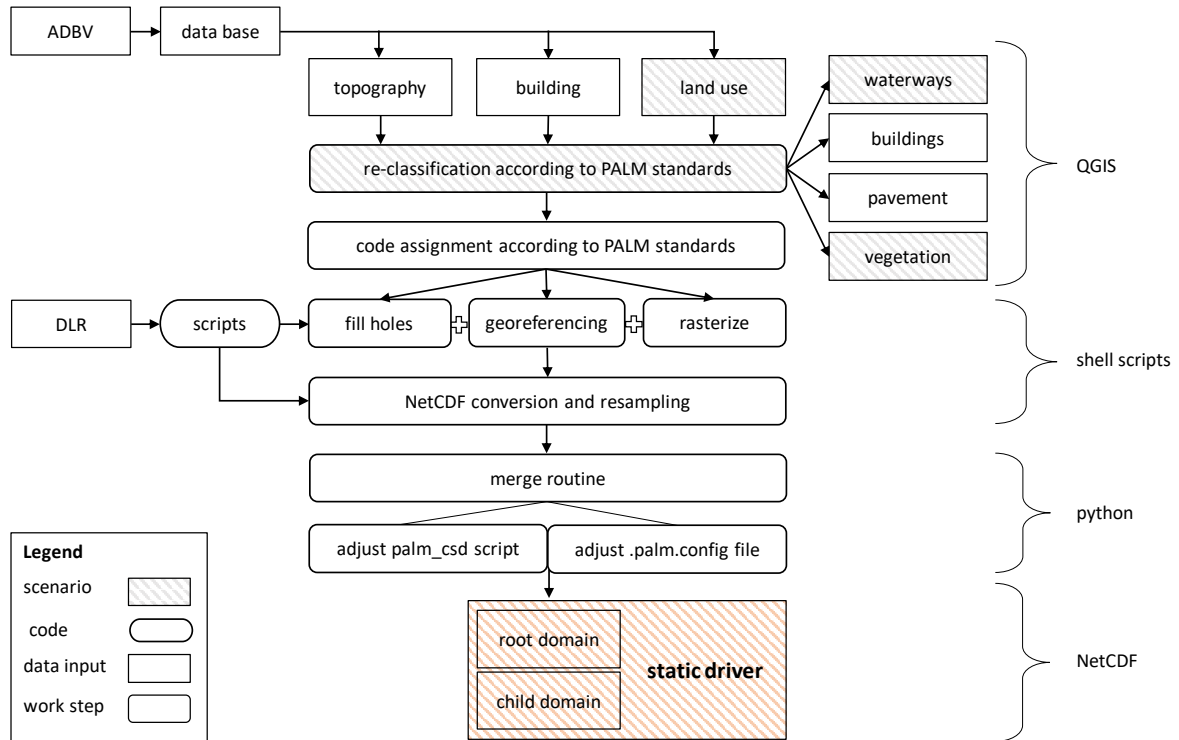


Figure 4: The input data set of the static driver consists of several steps of data preparation and transformation under the application of various software. The hatched line in grey indicates the key steps where changes for the computation of scenarios are conducted. Data originates from the ADBV and was prepared suitably to be passed on into the PALM4U model. Scripts originating from the DLR had to be re-written or adjusted to undertake further processing steps, and the data rearranged into NetCDF formatted data. The merge routine in python format is responsible for combining all information gathered into one and again arranges the data into a priority scheme after which the single layers are ordered. It finally compiles the domains out of this data which comprise all information for the static driver.

measurement station and overwritten with the original COSMO-DE2 data in the dynamic driver NetCDF. A switch of the soil type class inside the coarse COSMO-DE2 grid was not undertaken for the respective area in the PALM model due to a finer scale contemplation. This effect appears as a gradient for the finer scaled PALM model, leaving a faulty soil moisture gradient.

Once the drivers were created and stored as input data in PALM, a parameter namelist activated these and steered all remaining model processes (cf. Fig. A1). Its two mandatory namelist modules 'initialization parameters' and 'runtime parameters' set the extent, resolution, and height of the domain, link the connection to the initialization files of external forcing, set the parameters temporal output stamps and averaging interval, and

determine the total running time as well as the desired output format.

Table 2: Setup of the root domain and its nested inner domain

	Root domain	Inner domain	Unit
Resolution	20	5	m
X-direction	810	1620	pixel
Y-direction	675	1620	pixel
Z-direction	64	72	pixel
Z-height	3500	400	m
Origin	677024	681444	E-UTM
Origin	681444	5531006	N-UTM

The outer domain resembles the root domain. In z direction, a fixed height of 500 m is set. For z-values greater than 500, the grid was stretched by a factor of $d_z(k+1) = d_z(k) \times 1.08$. The inner domain is dislocated by 4420 cells from the lower left in x-direction and by 2980 from the lower left in y-direction of the root domain. There is no stretching applied for the inner domain. As mentioned before, each pixel of each domain covers information about topography, coordinates, and land-use type or building. The LSM consists of a solver for the energy balance of the earth's surface using a resistance parameterization for the surface fluxes and a multi-layer soil scheme. It is similar to the tiled ECMWF-scheme for surface exchanges over Land. For each surface element of the model grid, the equations of sensible heat flux, aerodynamic resistance, ground heat flux, thermal conductivity and latent heat flux are solved locally and respectively form the energy balance.

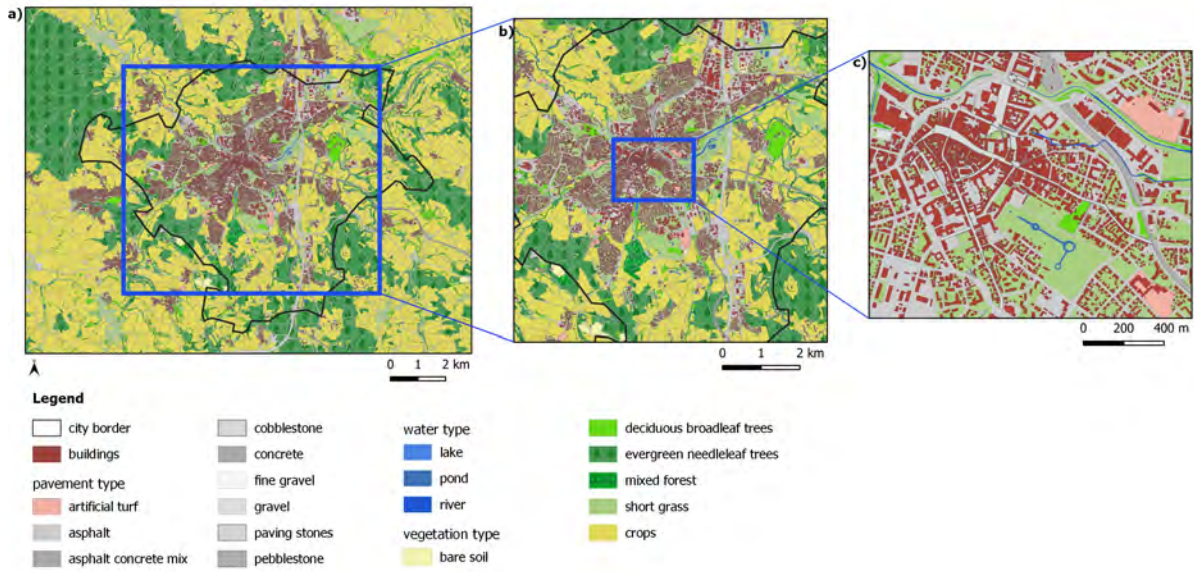


Figure 5: This map represents a) the domain of 20 m resolution (covering an area of 16.2 km in x-direction and 13.5 km in y-direction) and b) the intended domain of 5 m resolution (covering 8.1 km in x-direction and 8.1 km in y-direction) which is part of the root domain. The intended inner domain was anticipated to resolve the inner-city structures of c) where the Hofgarten and the Maxstraße are located. At the same time, it shall encompass all residential and city structure areas of Bayreuth. The root domain however, was meant to serve as adjustment zone for the LES to LES nesting. In the adjusted version the root domain is used only, still encompassing b) and c) but at a resolution of 20 m.

3.4. Technical composition and adjustment of the domain

While the buildup of the domains and their technical setup in PALM was achieved, the computation of the nested approach did not prove to be successful. The reason for this can be traced back to the interplay between the high computational request demanded by the LES PALM model and the limited resources available on the high performance cluster of the University of Bayreuth. Even though the cluster is technically equipped to offer the capacity for PALM model runs, the practical realisation exposed restrictions for a variety of reasons. To resolve eddies within street canyons, factors such as domain size in x, y and z direction, resolution and requested output data are decisive to determine the computing power needed. Boundary-layer processes encompass a wide scale of range. Therefore it would be required to consider both, the large model domain, including the surrounding orography, and a small grid size to resolve the effects of building structure of

Bayreuth. Hence, the use of nested child domains is very attractive for LES modeling, as this kind of simulation keeps the mesoscale processes on a coarser grid and refines the grid within the core city of Bayreuth. For the intended simulation LES - LES one-way coupling approach was chosen as focus needed to be put on the core city only. This way, an anteropulation step is omitted which saves computational costs compared to a two-way nesting where the child influences its root domain through anteropulation, mapping the fine-grid resolution back to the root domain. In the one-way resolution the parent domain is independent from the child simulation. In return, the decoupling of turbulence may lead to strong discontinuities. The technical composition of this study's domain evokes a row of individual conversions of physical processes needed in order to perform the simulation. The setup requires orography information and offline nesting to store boundary values provided through COSMO for all boundaries of the domain. The boundary data is interpolated linearly in time using non-cyclic boundary conditions. These are stored in the dynamic driver. The synthetic turbulence generator is required at lateral boundaries to initiate turbulence. Based on the prescribed time and length scales along each direction, unscaled turbulent motions are computed under the consideration of the amplitude tensor, based on the Reynolds stress tensor (Maronga et al., 2019). The calculated turbulence is then added to the mean inflow data of the velocity components (U_i)(cf. Eq. 10)

$$u_i = U_i + a_{ij}u_{*j} \quad (10)$$

and a mass flux correction suggested by Kim et al. (2013) is performed. In this case, the required length and time scales as well as the Reynolds stress tensor are not known from measurements and thus need to be parametrized. In PALM, only height dependent information of these variables is considered to estimate the turbulence statistics at the inflow boundaries. For a multiple-hour simulation, dynamic adjustment of the strength of the imposed turbulence is given, in respect of changing atmospheric stability. The pressure solver applies a multigrid scheme for solving the Poisson-Equation for non-cyclic boundaries. For the nested run, the physical settings vary slightly between root and inner domain, as the inner domain initiates from the root domain. The applied physical equations are stated in the parameter files of each run, once the variable deviates from its default setting.

The realisation of the nested model run is estimated to request a computational amplifi-

cation of factor 21.6 (cf. Eq. 11).

$$timestepfactor = \frac{dx_{root}}{dx_{child}} \times \frac{nx_{child}}{nx_{root}} \times \frac{ny_{child}}{ny_{root}} \times \frac{nz_{child}}{nz_{root}} \quad (11)$$

The high performance cluster of the university of Bayreuth revealed much inconvenience at the computation of simulations that requested more than 16 nodes. Originally, an estimation of 57 nodes, accessing 1368 cores was believed to be best practice. Consequently, a cutback to 16 nodes with 384 cores certainly increases the computing time. To overcome the aftereffect of running out of computing time, restart runs were enabled that split the model run into a job chain of n jobs. Once a run hits the given wall time limit of 50 hours, a following job is automatically initiated that can access the stored output data of the latest run. Still, the nested model setup did not overcome the process of initialization of the model setup by the time the wall time limit was reached and was not able to write any output data to be temporary stored. With regard to the limited performance available, it was decided to downsize the nested approach to an approach which comprises the coarser root domain only.

The city of Bayreuth is made up of many narrow alleys which cannot even be reproduced by the attempted 5 m resolution grid. For the coarser 20 m mesh, additional alleys are omitted and more are represented by very few pixel. As the coarser resolution showed no street canyons for almost the complete city of Bayreuth, further restructuring of the data had to be done. It was adapted as following: first, all larger paved squares and industrial areas were taken out from the raw data. In addition, small pathways were also excluded from the dataset to diminish the absolute amount of paved surfaces and decrease the relation of paved surfaces to all other surface types. Secondly, this land-use class was re-rasterized and transformed to NetCDF. Thirdly, the prioritization scheme was altered placing all waterways and paved surfaces above the other land-use types. This way, buildings can be suppressed by all paved streets large enough to be reproduced by the 20 m resolution, forming street canyons between the building areas. An altered static driver was computed and used as input for the recomputation of the dynamic driver. An altered parameter file neglects the nesting sections. This setup is certainly expected to output less and less detailed information about the inner-city range of heat effects. Still, the areas investigated by the research questions and hypothesis should be large enough to perform in this altered approach.

Figure 6 shows the site of Bayreuth in shapefile format. It displays the overlay of layers

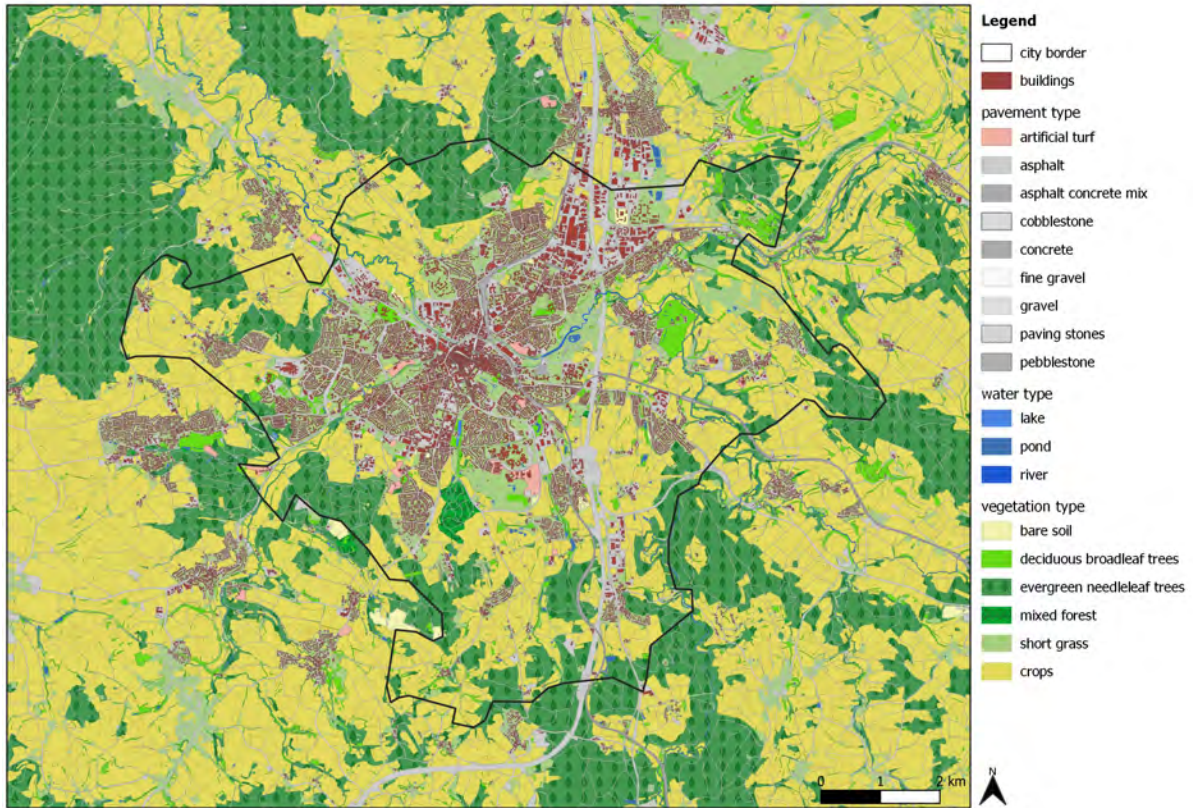


Figure 6: Overview of the root domain in 20 m resolution by a scale of 1:72 000. This map displays all shapefile layers categorized after A4 that are requested by PALM. The composition of these layers is based on the prioritization scheme applied on the python routine, merging the single layers to one single NetCDF.

and represents the distribution of land-use types. The shapefile format is useful for reclassification, while the actual files that enter the PALM4U model simulation appear as gridded NetCDF format (cf. Fig. 7). PALM4U requires differentiating of vegetation type, water type, pavement type, buildings in LoD2 format filtering out the building height, soil type, building type, a building number and topography. Every single class defined in PALM offers fixed subcategories after which the land-use data may be categorized. Table A4 provides a reclassification of beforehand class and category to the corresponding PALM provision, including a code given for each subcategory. The codes can be seen in the legends of Figure 7 and stimulate the source code of PALM4U to compute according to the individual setup. These codes are passed on together with the respective NetCDF files and then steer the development of micrometeorological conditions for each pixel within the investigation area. Slight differences stand out when comparing Figure 7 with Figure 8 which are caused by the change in resolution. The pictures of Figure 8 show a

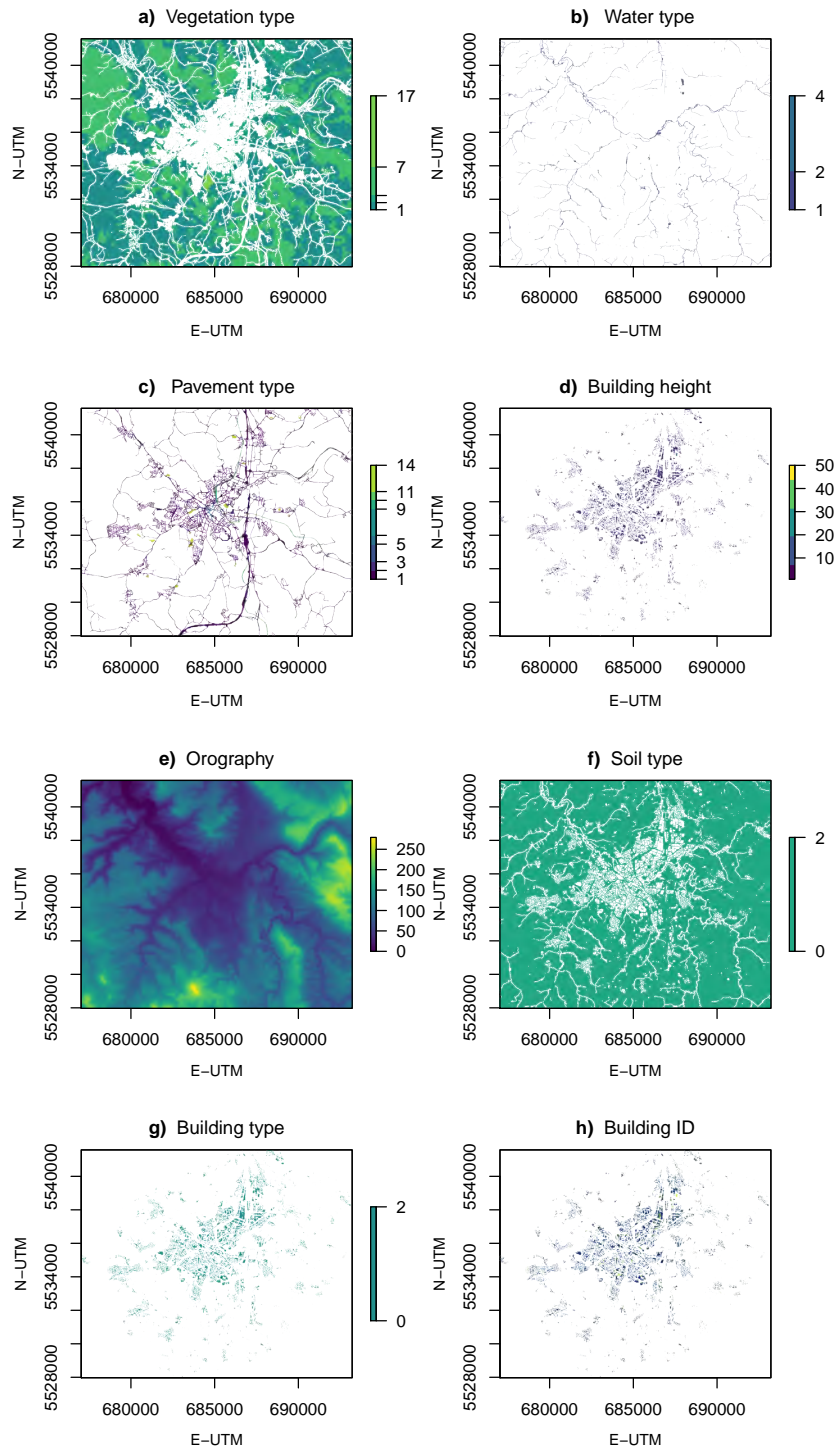


Figure 7: Ensemble of the static driver input data of 20 m resolution as it is requested by the PALM4U model for further computation. Every input represents a single NetCDF files that originated from the shapefiles with data from the ADBV. a) vegetation type, b) water type, c) pavement type and d) building height, e) topography, f) soil type, g) building type, h) building ID. The legend labels show the bulk PALM code for the particular land-use class. Detailed images of building type and building ID are provided in the appendix (cf. Fig. B3).

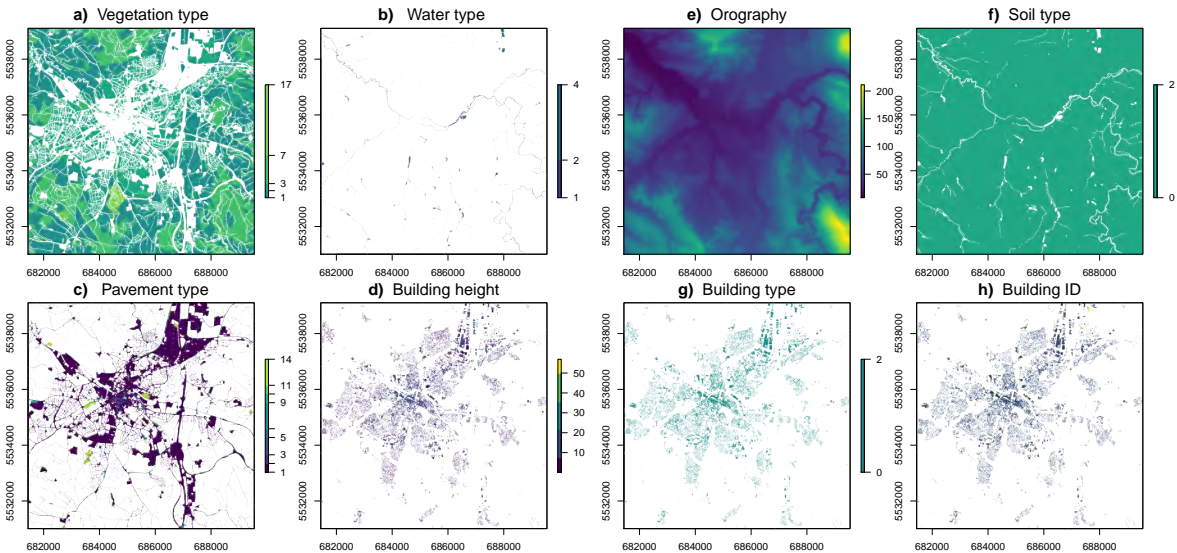


Figure 8: Schematic of the static driver for the inner domain of 5 m resolution to be nested into the root domain. Every domain needs to be equipped with its own static driver (cf. Fig. 7) that, depending on the chosen nesting approach, the domains may run separately or in dependency from one another. As the child domains' geography is a compound of the root domain (cf. Fig. 5), both static drivers produce a very similar image. Slight differences are generated by the resolution size. The same files are shown as in 7.

coherent structure for every layer representing the city infrastructure. The resolution of 20 m in Figure 7 was too coarse to represent street canyons. Instead, first test runs revealed buildings to cover most of the space within the Bayreuth city border. However, the existence of street canyons is indispensable for urban climate simulations. Therefore, minor changes were applied to make use of the dataset with the 20 m resolution. Most importantly, the adjustments in the prioritization scheme compared to the default of PALM4U (cf. tab. A2) are needed to create street canyons. By placing the pavement layer on top of the building layer, the streets of the static driver are able to suppress buildings. As a result, the cityscape of Bayreuth is kept at the same time. However, the amount of paved surfaces in the model became proportionally high. Due to this reason, larger paved squares such as in the industrial area north were manually removed as well as all minor paved roads predominantly in the surroundings of Bayreuth city. The resolution size of 20 m seems to be too coarse for the proper application of urban climate modeling, especially for small size towns such as Bayreuth that are made up of many narrow alleys. Restricted by computing capacity, there was no alternative to the 20 m resolution. The different resolutions result in differences in replicability (cf. Fig. 10) of

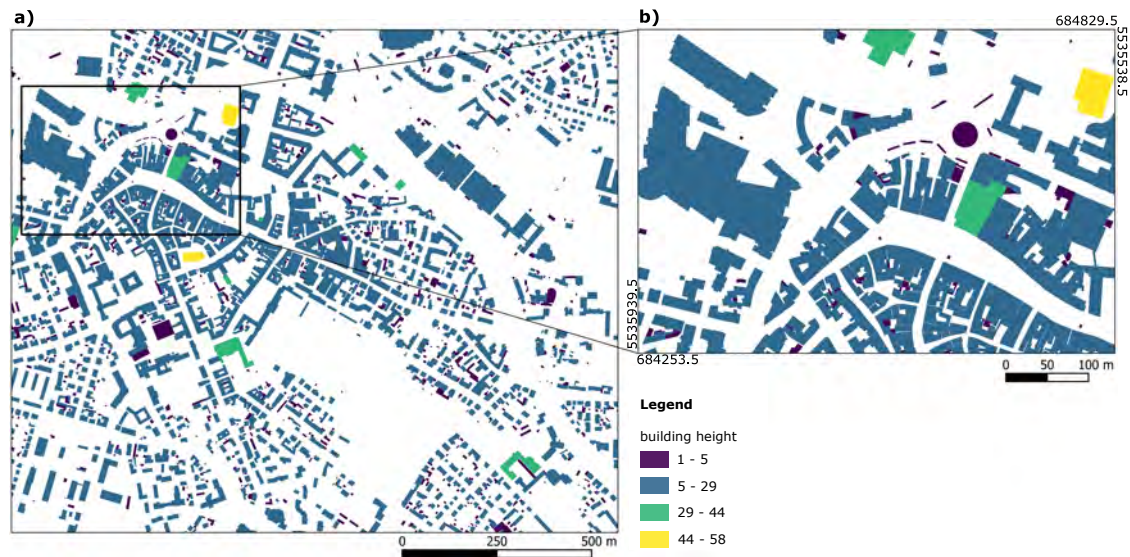


Figure 9: Original shapefile-cutout of the Maxstraße, Bayreuth.

the domain. The data originates from a non-resolution shapefile and was first converted into a 1 m raster resolution. The 5 m resolution is still capable of representing a realistic city image and resolve a street canyon shape of the city, the 20 m resolution domain is

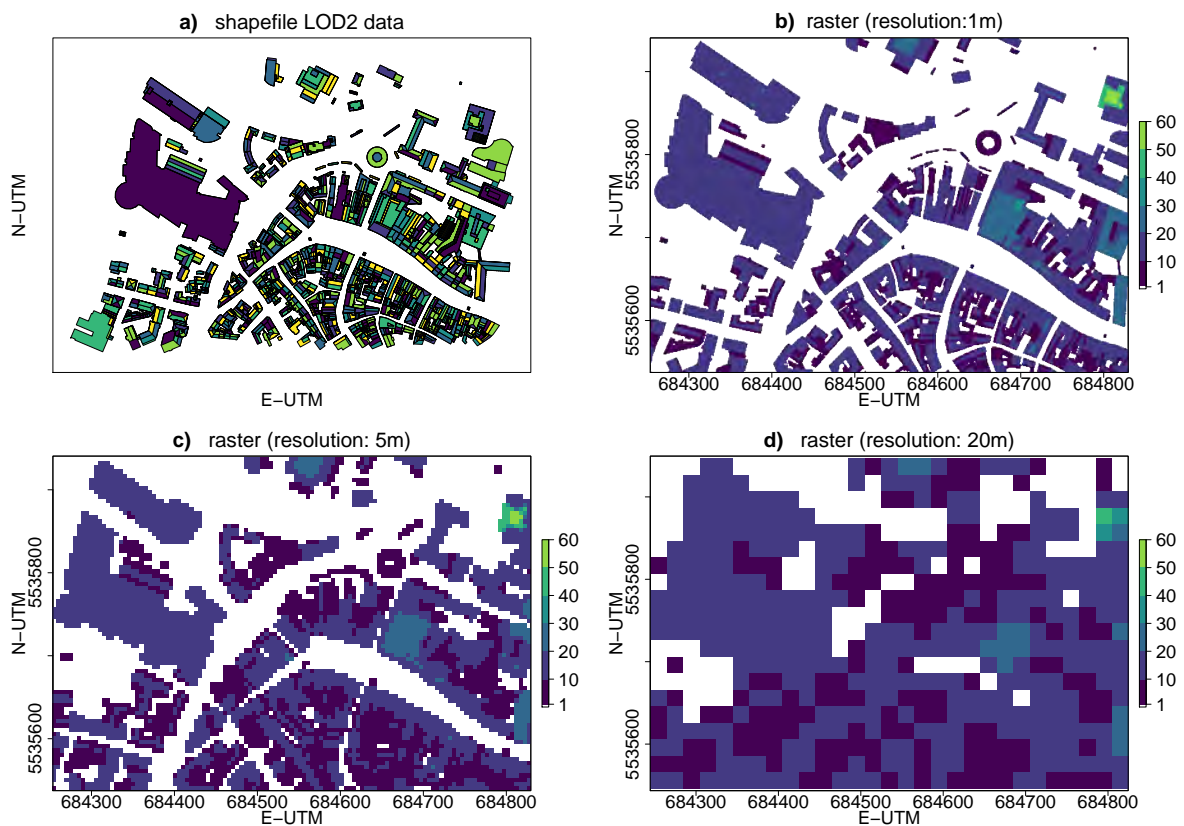


Figure 10: Implementation of the domain in a) shapefile format, b) 1 m resolution, c) 5 m resolution and d) 20 m resolution.

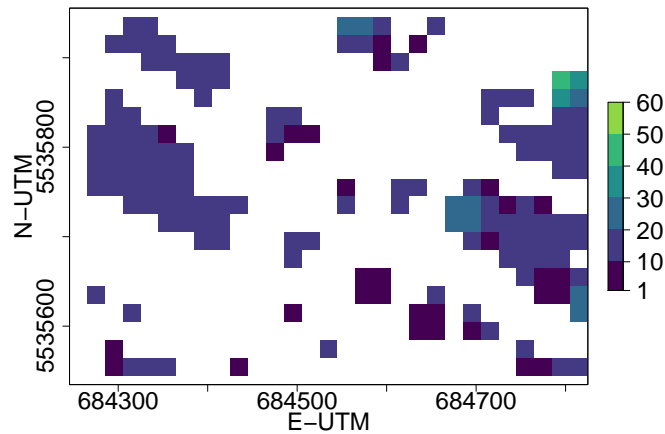


Figure 11: 20 m resolution domain after the adjustments and alterations of the static driver were carried out. Street canyon structures were forced by overlaying the pavement surface layer on top of the LOD2 housing layer.

more blurred and it is quite hard to recognize original shapes. The 5 m resolution was originally intended for the nested inner domain, which was then switched by the 20 m resolution for the current approach.

3.5. Synoptic forcing and micrometeorological conditions during heat wave 07.25.2019 – 07.28.2019 in Bayreuth

3.5.1. Observations from MiSKOR network

The choice of a suitable time period for the simulation of urban micrometeorological effects, in particular heat effects, was made using air temperature. The period with highest air temperatures in the year 2019 was taken. 2018 and 2019 were two years in a row with a very pronounced and long summer period. These effects were distinctive not only for Bayreuth but all Germany (Zscheischler and Fischer, 2020). A prolonged drought throughout the summer of 2019 led to agricultural crop failure in the Bayreuth region. For urban climatology, urban heat effects become most cognizable when temperatures are high and precipitation is low. The effect of urban temperatures rising several degrees above rural temperatures in surrounding areas is typically assessed through records of daily extreme temperatures (Dupuis and Trapin, 2020). The synoptic forcing situation was initiated by a high pressure ridge of air masses deriving from the southwest and expanding over Germany. Creating a high above ground for middle Europe, the transported hot

air was heated up further and became quite dry. The period itself can be divided into two sections: a) the days of 07.25.2019 and 07.26.2019, where the ridge grew very large and expanded up to Fennoscandia forming a completed high. Hot air from the land and undisturbed incoming radiation caused all time air temperature peaks for many weather stations in West-Germany. Conditions were anticyclonic and primarily autochthonous; b) the days of 07.27.2019 and 07.28.2019 were characterized by the fennoscandian high migrating slowly towards the Norwegian Sea, transforming to a cyclonic and primarily allochthonous forcing with little inflow of humid air.

The DWD published a deviation of daily mean air temperature of + 10 °C compared to the mean from the years 1961 - 1990, measured at weather stations in southern Germany for the days of 07.25.2019 and 07.26.2019 of July. For the 07.27. it is + 4 °C and for 07.28 0.8 °C. Thus, the 07.25 is the hottest day in 2019 not only regionwide but throughout Germany (DWD, 2019).

An investigation of the heat wave period between 07.25.2019 00:00 and 07.29.2019 00:00 was carried out for Bayreuth explicitly. Potential temperature, windspeed, wind direction and incoming shortwave radiation from the measurement stations of the MiSKOR project are examined in detail. The observations for 07.25. 00:00 - 07.26. 23:00 are significantly different from the 07.27. 00:00 to 07.28. 23:00. The potential temperature shows large diurnal variations of 20 K with a mean peak reaching up to 312 K. The peak is at noon and standard deviation is the smallest slightly offset after this peak. The mean of the windspeeds appears to be quite low and shows an increasing trend towards the afternoon, before it abruptly diminishes in the evening. It is smallest during the nocturnal cycle. The incoming shortwave radiation overall mean for all stations shows very large deviations from the mean. This finding is caused by the fact that the 15 measurement stations are placed in very diverse locations in the city of Bayreuth. Therefore they do not have equal exposure to unobstructed sky. For this reason, a second graph of incoming shortwave radiation (cf. Fig. 12 bottom) was generated with stations that are placed at an exposed site in the open-space. These include the sites of Mistel, Wilhelminenaue, St. Johannis, Eichelberg and the Karstadt roof. Standard deviation is very little and a clear peak just before noon is pronounced. The second half (07.27. 00:00 to 07.28. 23:00) of the heat wave is distinctly different from the first days DWD. Potential temperature diurnal variations are < 10K. There is no distinctive peak in temperature for the cyclonic half of

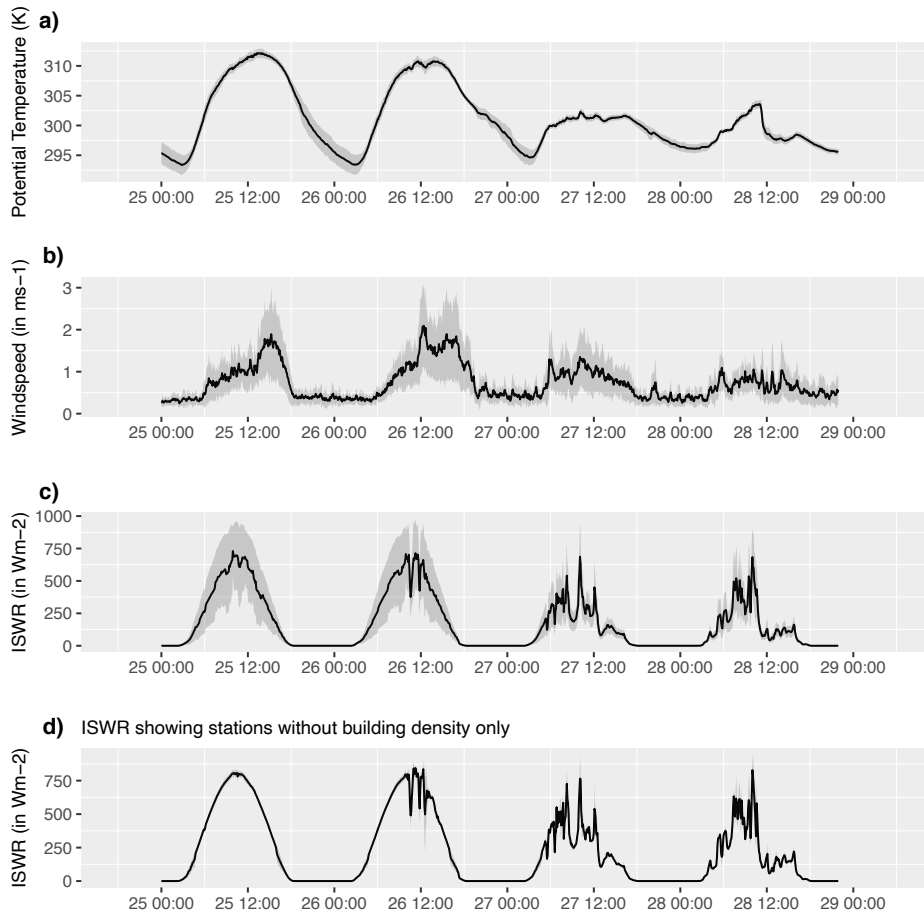


Figure 12: Mean of micrometeorological conditions between 07.25.2019 00:00 and 07.29.2019 00:00 from MiSKOR measurements in 10 minute intervals. This graphic illustrates a) the prevailing potential temperature, b) windspeed and c) incoming shortwave radiation, as a spatial mean over all 15 measurement stations of the MiSKOR network, d) incoming shortwave radiation for those stations that are located at an exposed site, namely Mistel, WilhelminenAue, St. Johannis, Eichelberg and Karstadt (cf. Fig. B2). The grey band indicates the standard deviation from every respective parameter.

the Fennoscandian high. Slight variability can be seen which underline the existence of the inflow of humid air. Mean windspeed is very low and does not show any clear peak. It is merely stronger for 07.27. 12:00-14:00, and more pronounced during the diurnal cycle for 07.28. The incoming shortwave radiation shows very similar behaviour between the mean of all stations and the exposed sites for the second half of the heat wave period. However, the magnitude of mean deviation is smaller.

The windroses in Figure 13 were chosen based on their relative location in the city. A comparison of the pedestrian zone 'Maxstraße' with the 'Hofgarten' (cf. Fig. B2) as recreation area and the very small and contorted 'Kaemmereigasse' (cf. Fig. B2) already

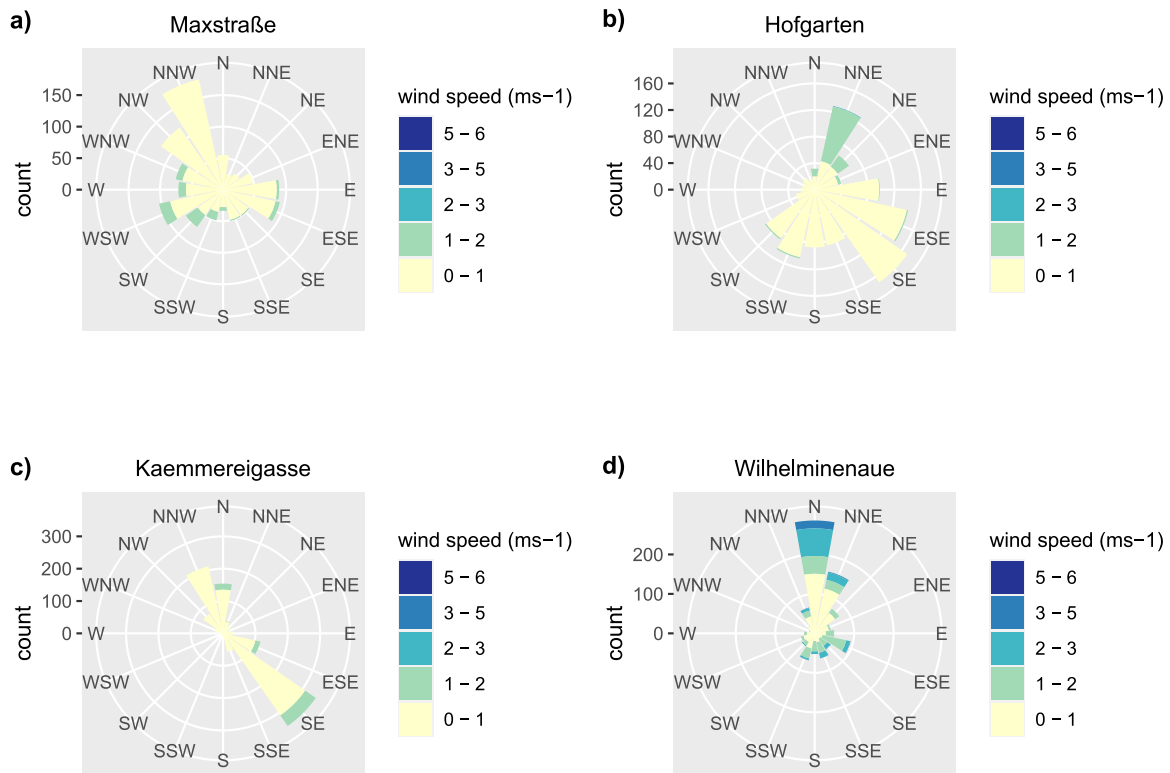


Figure 13: Wind roses for the mean of the period from 07.25.2019 00:00 to 07.28.2019 00:00. Windspeed and wind direction were extracted from the MiSKOR measurement sites at a) Maxstraße, b) Hofgarten, c) Kaemmereigasse and d) Wilhelminenaue, recorded in 10 minute means of instantaneous data.

represent three very different sites all located in the inner-city area of Bayreuth. Wind is a very locally influenced climate parameter which is reflected in Figure 13. Compared to the stations within the city, the station at the Wilhelminenaue is not impacted by nearby built-up area and located in the open space. Accordingly, the windspeed is slightly stronger (up to 5 ms^{-1}) at this station, whereas the stations within the city show weak windspeed ($0 - 2 \text{ ms}^{-1}$). Figure 12 demonstrates this high deviation.

3.5.2. Near-surface weather as simulated by PALM4U

The micrometeorological conditions from the identified heat wave period for the simulation period were translated into PALM4U by use of the INIFOR tool. PALM4U gets its synoptic forcing information via the dynamic driver which derives the data from the data assimilation process of COSMO-D2. An analysis is available for every full hour which implies that the dynamic driver data is generated from hourly means (cf. Fig. 14). Table A3 in the appendix lists all the variables that are requested from the COSMO-D2 and

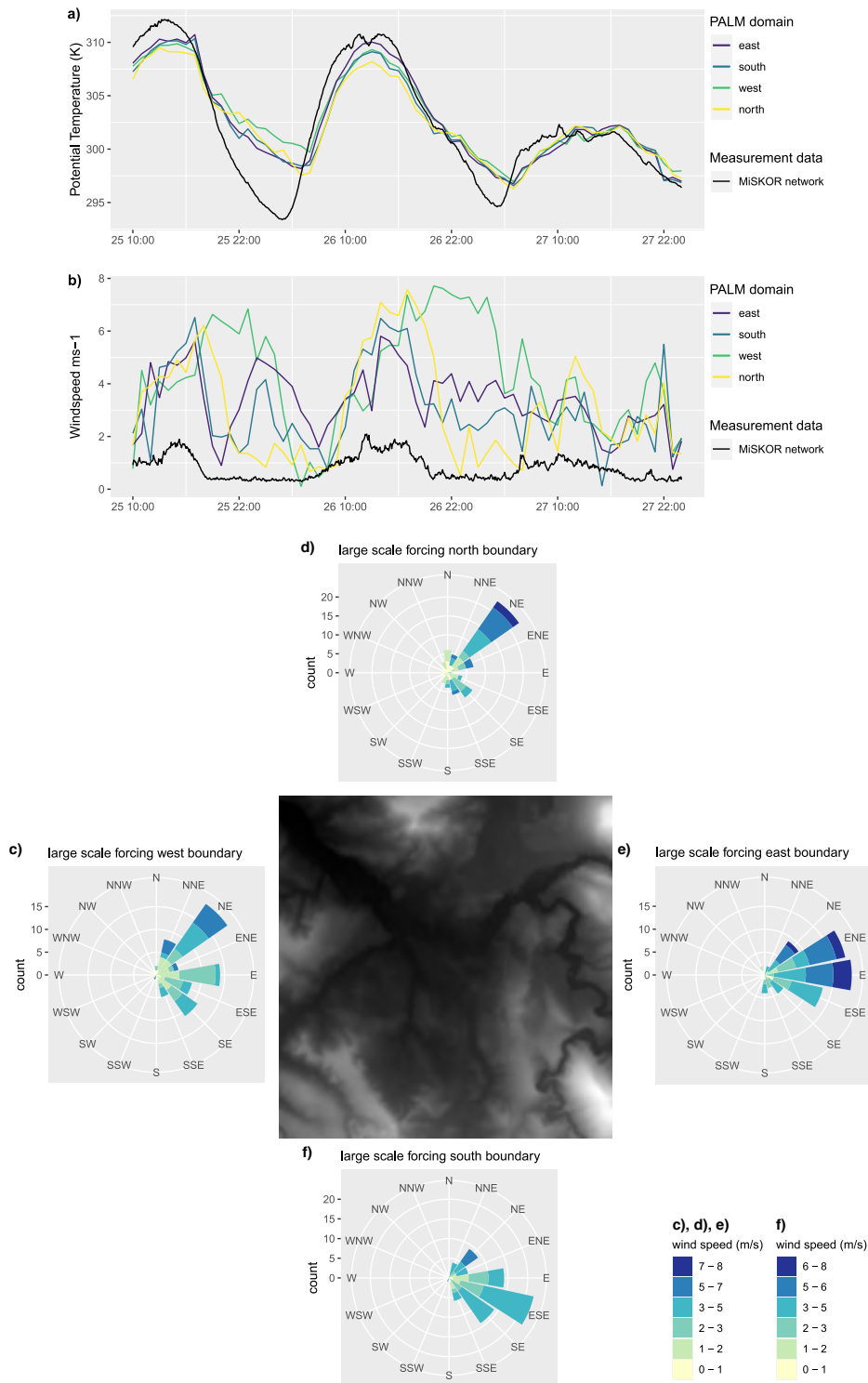


Figure 14: Schematic of a) mean potential temperature in Kelvin, b) mean windspeed in ms^{-1} and c) wind direction in degree averaged along the western, northern, eastern and southern side of the domain for the period from 07.25.2019 10:00 to 07.28.2019 00:00. The data was computed by a one dimensional spatial mean taken along the coordinates (E-UTM: 682524 - 688024, or N-UTM: 5532546 - 5537026) at the range of the domain, where the city of Bayreuth is located. The colours refer to the corresponding side of domain, whereas the black line indicates the respective mean of the Miskor measurement network data of Fig. 12.

Table A5 in the appendix lists the ones that are stored in the dynamic driver. Two input possibilities exist for the dynamic driver: First, the transfer of measurement data into the dynamic driver manually, or second, the offline nesting linkage to the COSMO model which is the approach chosen for this simulation. The forcing data for the PALM4U model is computed either as initial parameter and/or per each side of the domain boundary, including the top boundary. Incoming shortwave radiation is not considered for Figure 14, because this parameter was transferred from the measurement data. The data from the MiSKOR stations was measured from 4.5 m above NN height, whereas the lowest data point of data in the model is given in 10 m above NN. This refers to the lowest computational simulation height possible, as the parameter output is at mid cell size. For potential temperature, the amplitude of the diurnal variations of the PALM input data and the MiSKOR network are in agreement with each other (cf. Fig. 14). There is an offset for both maximum and minimum between the MiSKOR and the PALM data; the MiSKOR data is more pronounced by up to 5 K in its magnitude. However, the site of measurement (MiSKOR network) and simulation (PALM input data) vary since the MiSKOR network represents a mean of stations across and inside the city whereas the PALM input data is simulated at the boundaries of the domain. For windspeed, very similar behaviour is depicted. While diurnal variations and their amplitude match, the magnitude of the MiSKOR network is clearly lower than the PALM input data. A difference of 5ms^{-1} is shown. In consideration of the location offset of measurement stations and simulation location, a lower mean windspeed for the built-in and partly wind shielded inner-city MiSKOR network is reasonable. Wind directions range from northeast to southeast, which are the directions from where turbulence is hence forced into the model.

The profiles of the potential temperature and specific humidity are identical among the different boundaries (cf. Fig. 15). For this reason, a comparison for a random location was taken (Fig. B4), as this deviation can be caused by averaging over a topographical range of coordinates. Still, there is strong similarity among the four forcing boundaries.

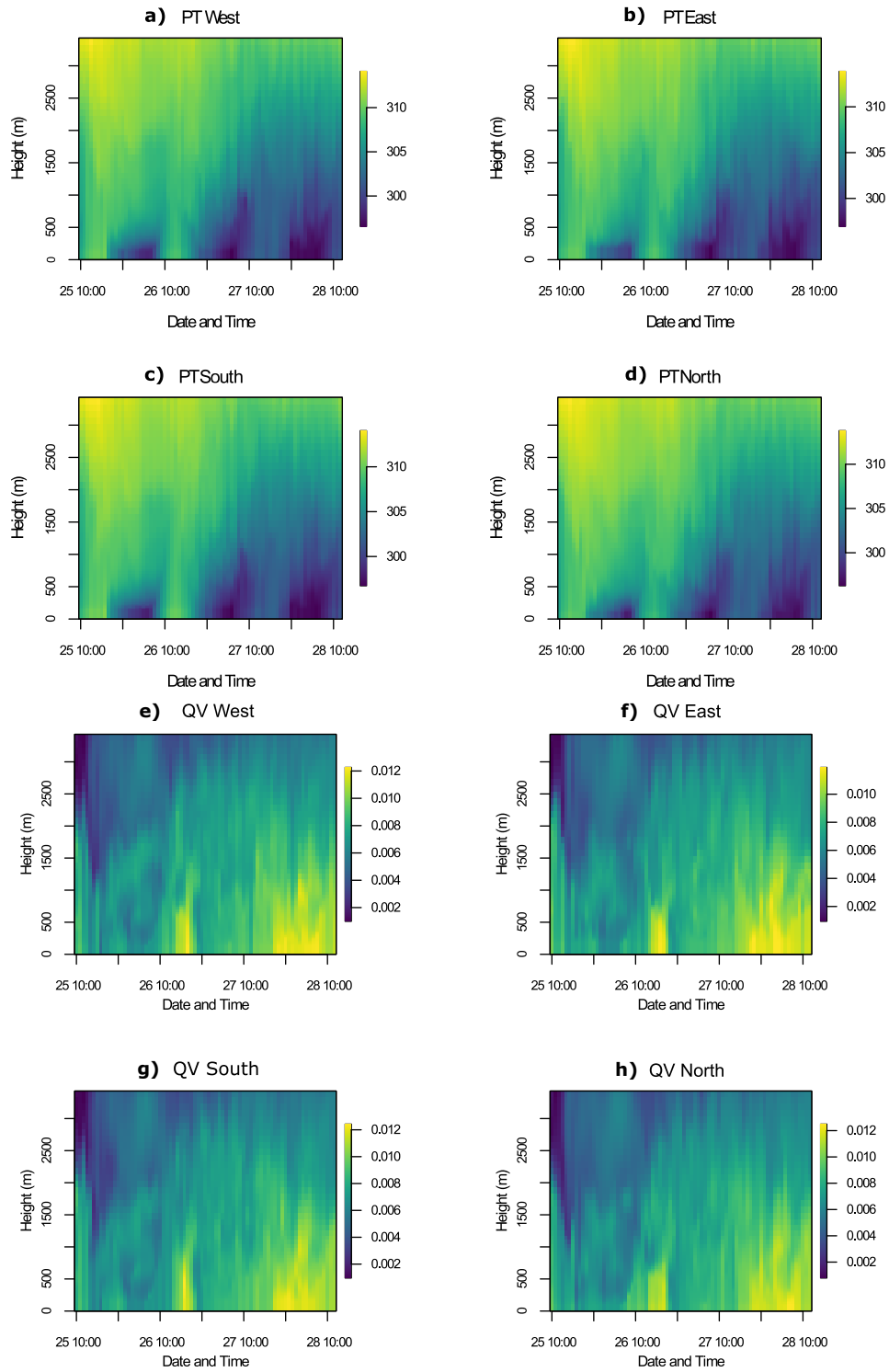


Figure 15: Time height cross sections of potential temperature (K) and specific humidity profile (kgkg^{-1}) for every domain boundary. The data was computed by a one-dimensional spatial mean taken along the coordinates (E-UTM: 682524 - 688024, or N-UTM: 5532546 - 5537026) at the range of the domain, where the city of Bayreuth is located.

3.6. Net radiation and energy balance in cities: radiation- and energy transfer

The exchange of energy between the earth's surface and the atmosphere involves four important processes, namely absorption and emission of electromagnetic radiation by the surface, thermal conduction of heat energy within the ground, turbulent transfer of heat energy towards or away from the surface, and evaporation of water or condensation of atmospheric water vapour onto the surface. The energy balance is the sum of all fluxes of energy passing each second through a horizontal surface of a unit area (Foken, 2017, p. 10) - these processes can be measured in energy flux densities. In comparison to Equation 2, the general energy balance for a surface layer of finite depth is written as

$$\frac{dE}{dt} = Q^* - G - Q_H - Q_E \quad (12)$$

For this thesis, the loss of energy by heat conduction through the lower boundary is negative, it is a positive number when it is directed away from the surface into the ground. Heat conduction within the soil follows the law of heat conduction by Fourier:

$$F_H = -k \frac{dT}{dz} \quad (13)$$

The value at the surface is denoted G_0 . For an infinite surface layer, the energy balance reduces to:

$$Q^* - G_0 - Q_H - Q_E = 0 \quad (14)$$

as the heat storages equals 0. When converting the Equation to $Q^* - G_0 = Q_H + Q_E$, the available energy of the quantity $Q^* - G_0$ is partitioned between the sensible and latent heat fluxes. This in turn can be quantified by taking the ratio of the sensible heat flux to latent heat flux.

$$BO = \frac{Q_H}{Q_E} \quad (15)$$

Equation 15 shows the non-dimensional Bowen ratio which depends on the availability of water at the surface. BO is small for surfaces where water is freely available and most of the energy gets transferred to the atmosphere in form of latent heat. BO is large for surfaces which are dry and where thermal energy gets transferred to the atmosphere, followed by an increase of surface air temperature, which leads to a relatively high sensible heat flux in the energy balance. Vegetation plays a crucial role for the Bowen ratio as it

disposes of water availability.

The energy balance at the surface is more complex than the budget at the top of the atmosphere, because fluxes of energy by conduction and by convection of heat and moisture through fluid motion need to be considered. The surface energy budget depends on local conditions of insolation, surface characteristics like wetness, vegetative cover and albedo, and on the characteristics of the overlying atmosphere. It is closely related to the hydrologic cycle as evaporation, which is part of the latent heat flux, is a key component in the budgets of both energy and water. Equation 16 shows the hydrologic balance Equation (Foken, 2017, p. 26)

$$P = ET + R - \Delta S \quad (16)$$

The latent heat flux equals the amount of heat extracted from or added to the surface as a result of sublimation or deposition over snow and ice surfaces. For surfaces where liquid water is available, the flux is a result of evaporation or condensation. Independently, temperature plays a pivotal role in the magnitude of the latent heat flux because of its influence on the moisture content of the air. Temperature differences are a major factor for the sensible heat flux as they drive the heat exchange between the surface and the air temperature above it. It is negative when the surface is warmer than the air, driving an upward heat transport, namely convection. However, it can also be directed towards the surface when the positive net radiation has set in and eventually cools the surface, becoming colder than the air above. At sufficiently small distance above the surface, in the order of one to several millimeters, sensible heat and latent heat exchange between the surface and air occur predominantly by molecular conduction. Higher in the atmosphere, turbulence occurs as eddies that vertically mix momentum, heat, and moisture. Turbulence is more effective in transporting scalars than molecular diffusion (Stull, 1988). Sensible heat flux and latent heat flux are dominated by turbulent exchange. That is why they are usually referred to as turbulent fluxes. Under statically stable conditions, wind shear drives the generation of turbulent heat exchange. Wind shear is enhanced over rough surfaces and can be provided by catabatic forcing. The generation and movement of turbulence and forcings in contrast depend on the environmental setting. Therefore, latent heat flux, sensible heat flux and ground heat flux can vary strongly between cities and rural areas. Besides, the net radiation flux determines the energy

balance significantly, also being subordinated by site-specific factors.

$$Q^{*s} = K \uparrow + K \downarrow + I \uparrow + I \downarrow \quad (17)$$

The net flux in Equation 17 is the sum of the downward shortwave direct and diffuse solar radiation, the reflected upward shortwave radiation, the upward longwave radiation emitted from the surface and the downward longwave radiation emitted from different levels of the atmosphere such as backscattering. The direct solar beam at the top of the atmosphere is formed of parallel rays that become attenuated when passing through the atmosphere due to absorption and scattering by molecules and aerosols, reducing the irradiance at the surface. Still, some of the scattered direct beam radiation also reaches the surface as diffuse solar radiation. At the surface, the surface albedo quantifies the fraction of downwelling radiation reflected by the surface of the Earth which is the reflected upward shortwave radiation. From Wien's displacement law,

$$\lambda_{max} = \frac{2997}{T} \quad (18)$$

and from Kirchhoff's law,

$$\epsilon_{\lambda} = a_{\lambda} \quad (19)$$

the electromagnetic energy within the wavelength range between 3 to 30 μ m is emitted by the surface, namely the upward longwave radiation. A very small fraction of it is reflected by the atmosphere, the reflected downwelling long wave radiation incident on the surface. The radiation balance changes over the day and throughout the year due to the incoming solar radiation, which is of major influence on the radiation balance, followed by the sky cloud cover. By global annual average, the radiation budget for the earth's surface is positive, indicating an excess of solar heating over longwave loss causing a net radiative gain called radiative forcing at the top of the atmosphere leading to increasing global near-surface temperatures. Instantaneous values, however, may be positive or negative depending on site conditions. Especially the conversion of a landscape to urban land cover implicates large changes to the local and regional energy and water balances and local surface radiation budget. The spatially variable urban design of cities changes the local climate by altering thermodynamics of the surface energy balance and its coupling with the boundary layer above. The development of urban heat effects is governed by urban geometry since it regulates the absorption and emission of heat,

modifying the temperature of the air in the urban boundary layer, as well as the surface temperatures. Urban design factors that relate to biometeorological differences can be referred to as internal factors (Oke, 1982), whereas temporally variable forcings which are not part of the city can be referred to as external forcings. Fig. 16 shows an illustration of external and internal factors by (Spies, 2019). Anticyclonic summer

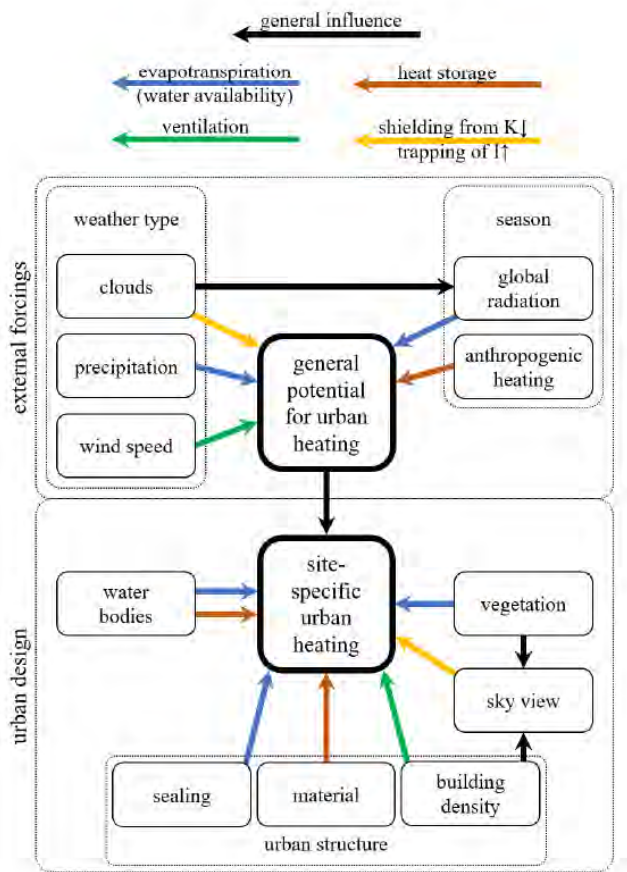


Figure 16: Schematic of parameters and mechanisms relevant for urban heating after (Spies, 2019). External factors that determine the potential for urban heating are presented in the upper part. The lower part illustrates city-internal, spatially variable factors responsible for site-specific heating. These are mainly given by the urban design.

weather conditions for example, usually amplify urban heat island effects and can cause or exacerbate heatwaves. The smallest intensities, in contrast, occur under turbulent, windy conditions, where the urban–rural temperature contrast is clearly suppressed owing to small differences in the corresponding energy budgets. Here, high wind speeds can diminish air temperature differences completely (Oke and Cleugh, 1987). Therefore, the most relevant non-local meteorological parameters are clouds and advection. Surface characteristics like albedo, the complete aspect ratio, roughness length or moisture

availability significantly control the energy balance partitioning of any surface. The city morphology of Bayreuth for example, includes buildings and surface types but it neglects trees, as their data acquisition through laser scanning points, classification and the technical incorporation into PALM4U would have required extensive labour resources. For cities such as Bayreuth, internal factors and external forcings partition the energy balance (cf. Eq. 2). In general, radiation fluxes above urban areas have similar magnitudes and diurnal behaviour to those of rural surfaces (Oke and Cleugh, 1987). On the contrary, urban areas change phases of the ground heat flux and sensible heat flux. The ground heat flux often peaks earlier and the surface heat flux often peaks later than in rural areas (Grimmond and Oke, 2002). Effects of building morphology on the exchange of longwave radiation is a major control for surface temperature, just as the building surface material is on the shortwave reflectance. Downwelling solar radiation is absorbed to a higher amount, because some of the reflected radiation is retrieved as incident radiation at the same time when a further fraction is absorbed. Building morphology is also responsible for reducing the transfer velocities that mediate the sensible heat flux. Thus, more energy is absorbed into the materials of an urban surface. Here, thermal admittance of building material is also of high importance, especially for nocturnal urban effects. Furthermore, shadowing leads to a limited sky view effect which also causes the emitted longwave radiation to be absorbed from itself. Anthropogenic factors included in (cf. Eq. 2) can be direct, such as emission of heat or exhausts, or indirect such as enhanced mixing due to traffic generated turbulence. Human induced drainage or irrigation pathways in cities affect the energy balance by regulating the availability of water spatially which has an impact on the latent heat flux. Another important factor are anthropogenically produced aerosols, that change radiative transfer and thus alter the radiative fluxes at the surface (Oke, 1982). Besides radiation and anthropogenic factors, the sensible and latent heat flux change significantly between the rural and urban energy budget. While the latent heat flux becomes typically smaller in urban areas, the sensible heat flux gets larger and can even maintain a positive flux direction throughout the night (Harman and Belcher, 2006). Sealing reduces the availability of water enormously, leading to managed water transports just as described above. In Bayreuth, the water resources are limited to the Roter Main, Mistel and Roehrensee. Vegetative water transport processes as evapotranspiration are highly relevant for sealed areas, but they are only stimulated

once precipitation or irrigation occurs. Sealed areas with little vegetation, such as the inner-city area in Bayreuth, show hardly latent heat flux values. Surface fabric may support the heating depending on the effective heat capacity, albedo, emissivity, thermal conductivity and the surface roughness. The surface temperatures in cities remain higher, yielding a greater longwave emittance. Besides, cities such as Bayreuth are typically aerodynamically rougher than the surroundings. Heat advection can then transport the climatic impact downwind of the urban area into the suburban and rural surroundings. Due to horizontal heat movement within the urban canopy layer and downwind mixing of elevated heat by turbulent eddies, heat advection is also present near-surface.

3.7. Perceived temperature, potential temperature and air temperature to determine heat stress

The redistribution of elements of the radiation and energy budget and thus the transition of the net surface energy balance to an urban surface energy balance clearly indicates the complex conditions of heat exchange within cities. The increasing frequency of extreme hot days is a risk to human health and provokes heat stress in the human body. Humans need an optimum body core temperature for an active metabolism despite changing external conditions, whereas the body surface temperature may vary considerably. Humans' perception of heat does not derive from high air temperatures only. Solar radiation, wind velocity, humidity as well as heat radiation from atmosphere and ground have a decisive influence. To be able to quantify this heat stress, numerous simple thermal indices were developed to describe the interaction and perception between the human body and its thermal environment. Often, these are not universally valid and cannot be applied to all climates, every season or every spatial scale. Commonly, the perceived temperature, given in K or °C, is designed for staying outdoors and is defined as the air temperature of a reference environment in which the thermal perception would be the same as in the actual environment (Staiger et al., 2012). In PALM4U, the human thermal comfort module calculates thermal indices by estimating the thermal perception of humans considering the conditions within the model domains. Human perception of temperature includes air temperature, wind speed, solar and thermal radiation and, during warm conditions, humidity (Staiger et al., 2012). The index of PERCT was chosen to be displayed in the simulations. It is computed using a parameterisation based on a two-node model. The

single equations that build up the model are stated by (Staiger et al., 2012). While air temperature is absolute, the potential temperature is the theoretical temperature (K) that an air parcel would acquire if adiabatically brought to a standard reference pressure P_0 , usually 1000 millibars:

$$\Theta = T \left(\frac{p_0}{p} \right)^{\frac{R}{c_p}} \quad (20)$$

In PALM4U, potential temperature and PERCT can be printed for output. Air temperature was calculated according to Equation 20 by use of the hydrostatic pressure given by PALM, averaged across the domain. Given the domain size of the simulation, the hydrostatic pressure is not expected to change in any influential way. The topographical differences in height were considered by the inclusion of the adiabatic temperature gradient per height. To assess the anomalies of temperature appearing within the city and the temperature deviations expected among the scenarios stated in the hypothesis, measures of air temperature and perceived temperature are chosen to serve as representative parameters. For profile data over time and height, potential temperature is a representative parameter. When looking at the relative changes of Δ PERCT and ΔT values, no significant difference is expected between Δ PERCT and ΔT (Fanger, 1970; Hoeppe, 1999; Staiger et al., 1997). For this reason, perceived temperature will be used as a reference temperature in this thesis since the severity of heat effects is reflected of humans' perception of heat.

3.8. Application of scenarios

The conducted analysis can be subdivided into the base run and the single scenario runs. The base run is the simulation of the realistic replication of the cityscape of Bayreuth. The scenarios represent altered base run simulations of city planning measurement approaches. Three scenarios (A, B, and C) were prepared and technically implemented. Therefore, they are applied as single scenarios to assess their individual impacts.

Scenario A describes a change in the amount of surface water and serves research question 2. Scenario A involves doubling the amount of runoff of the Roter Main throughout the whole domain. The input data has been changed according to Figure 4. A buffer around the Roter Main of the same size as the Roter Main was added. The water type layer was the last to top all other layers during the process of stacking all the single data pieces into a multiple layer NetCDF file. Like this, the water surface layer cannot be superposed

by the other layers which would result in a diminution of the water surface. Besides, the Annecy square was flooded within scenario A to increase the amount of water floating directly through the city.

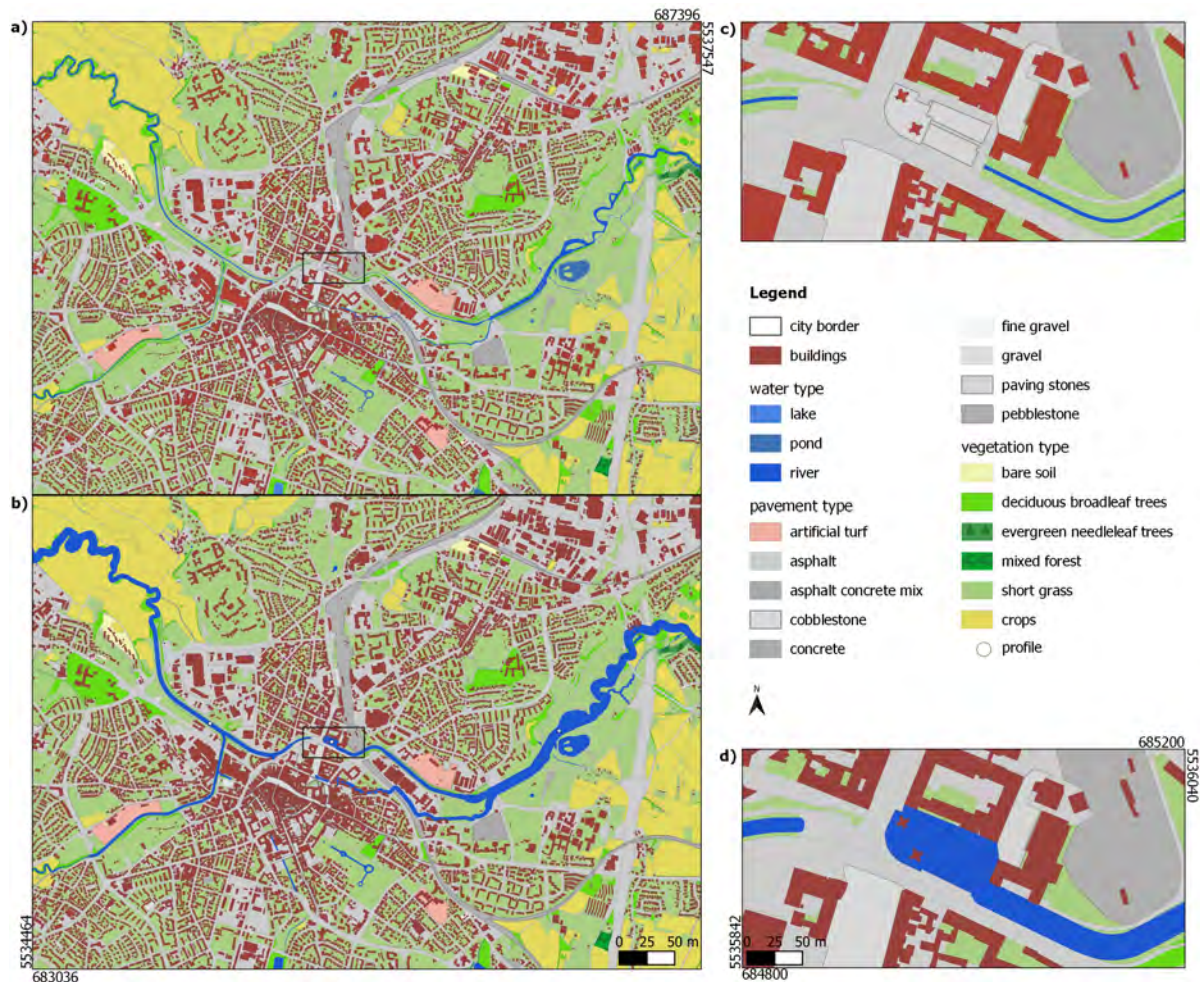


Figure 17: Map visualizing scenario A for the enlargement of the water surface of the Roter Main. A comparison between the base run and the scenario is shown. A second snippet shows the Annecy square which becomes flooded in scenario A.

Scenario B describes a change of outer wall and roof paint throughout the complete building area of Bayreuth. It serves research question 3 and shall imitate a white coat of paint of houses. The LOD2 dataset is both complex and powerful but yet, PALM4U offers no interplay or module tool to assign values or attributes to the already existing variables of the LOD2 dataset. Instead, scenario B was implemented by a change in the source code of PALM4U. A bulk parameter table, steered by the radiation module, was altered by an increase of 0.17 to 0.82 broadwave, shortwave, and longwave albedo for

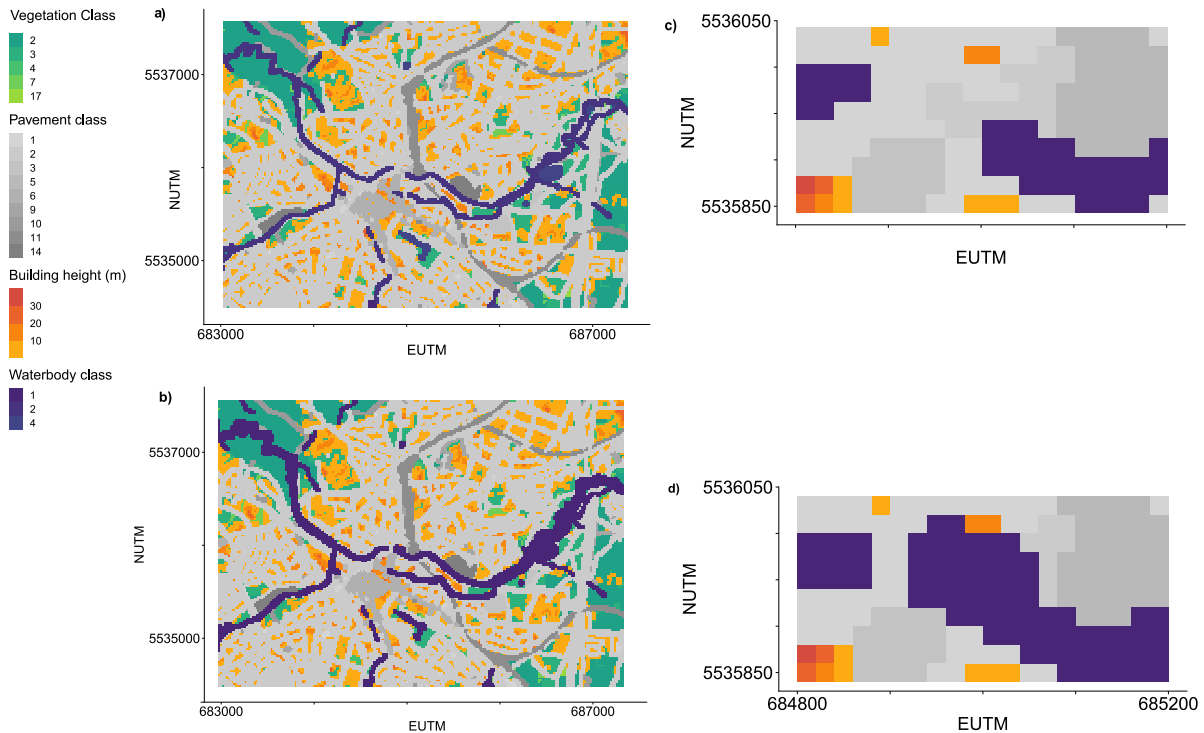


Figure 18: Visualization of scenario A (cf. Fig.17) in NetCDF, 20 m resolution, input into PALM. The legends display the bulk land-use type codes for PALM4U which belong to the files.

buildings. Accordingly, the albedo of 0.82 for houses shall imitate white houses including white walls and white roofs. To overwrite the source code implies a permanent change of the albedo. Thus, this scenario was computed last in a row, after the other scenario runs were completed. Especially the city quarters of 'Industriegebiet Nord', 'Hauptbahnhof' and the inner-city area stand out for their dense housing and were to be investigated in this scenario (cf. Fig. 19).

Scenario C describes the change evoked by the processes of transpiration and evapotranspiration. It shall investigate which spatial and absolute effects result from vegetated spaces in terms of steering the city climate of Bayreuth. It serves research question 4 and wants to identify, whether the Hofgarten as the main green inner-city corridor is capable of the provision of a cool spot, and on which scale this takes place. Therefore the scenario is split into C.1, which simulates a complete domain of drought stress, and C.2 which simulates a domain of drought stress except for the Hofgarten. This scenario is implemented by the change of land-use data classification, similar to scenario A. For the realization of this scenario, all vegetated land surfaces in the domain were switched from their original PALM4U classification code to one resembling 'bare soil'. In C.2, only the Hofgarten kept its original land-use type 'short grass'.

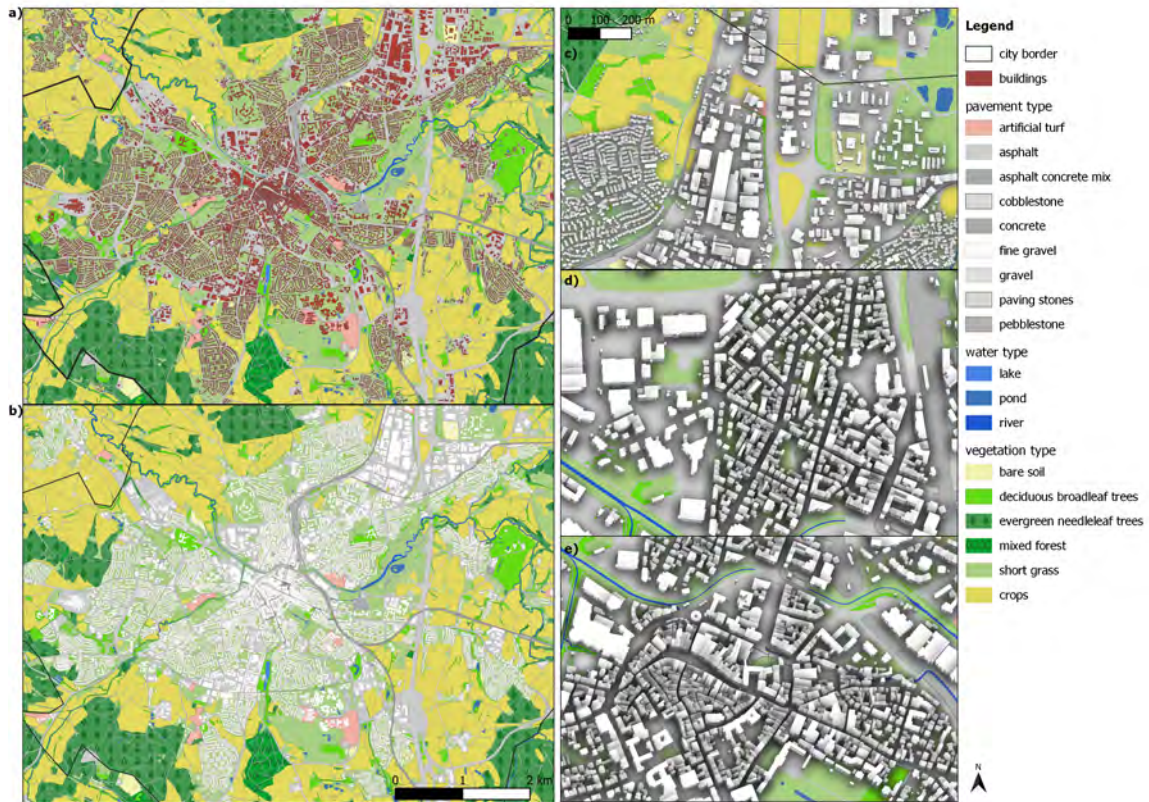


Figure 19: Map of scenario B representing the city of Bayreuth with exclusively white roof painted housing.

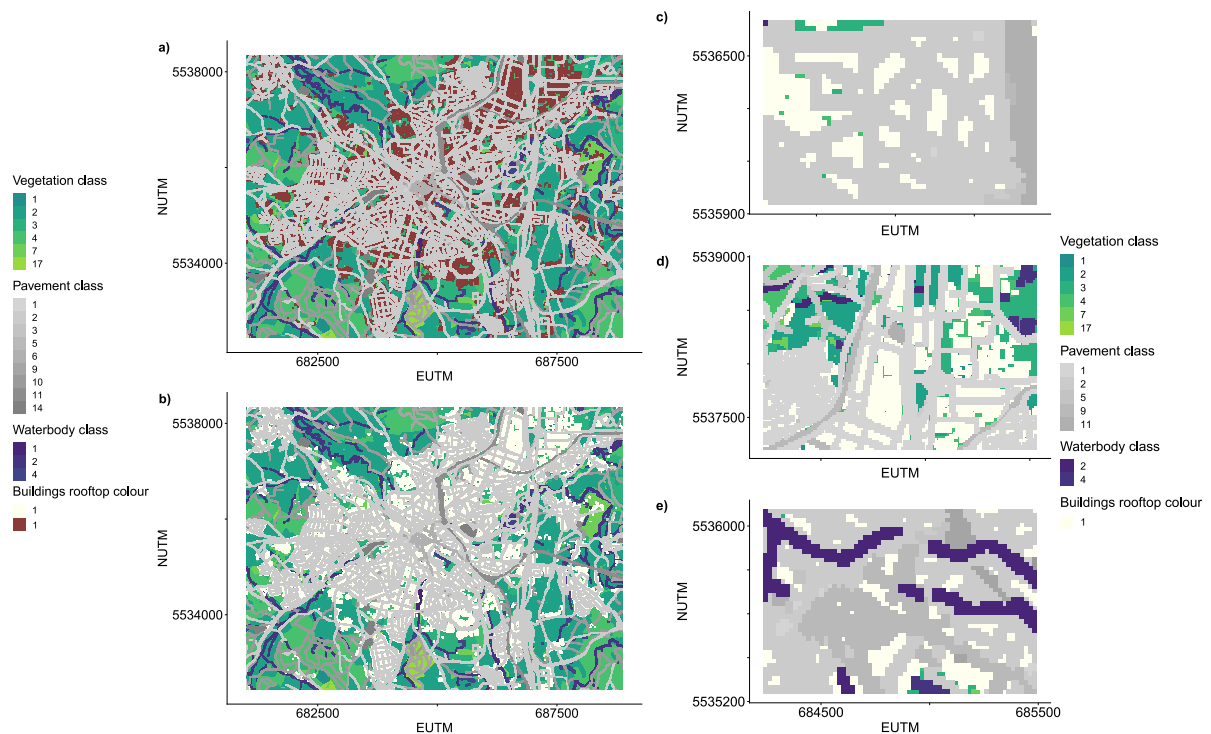


Figure 20: Visualization of scenario B (cf. Fig.19) in NetCDF, 20 m resolution, input into PALM. The legends display the bulk land-use type codes for PALM4U which belong to the files.

A spatial analysis was used for the examination and evaluation of the simulation

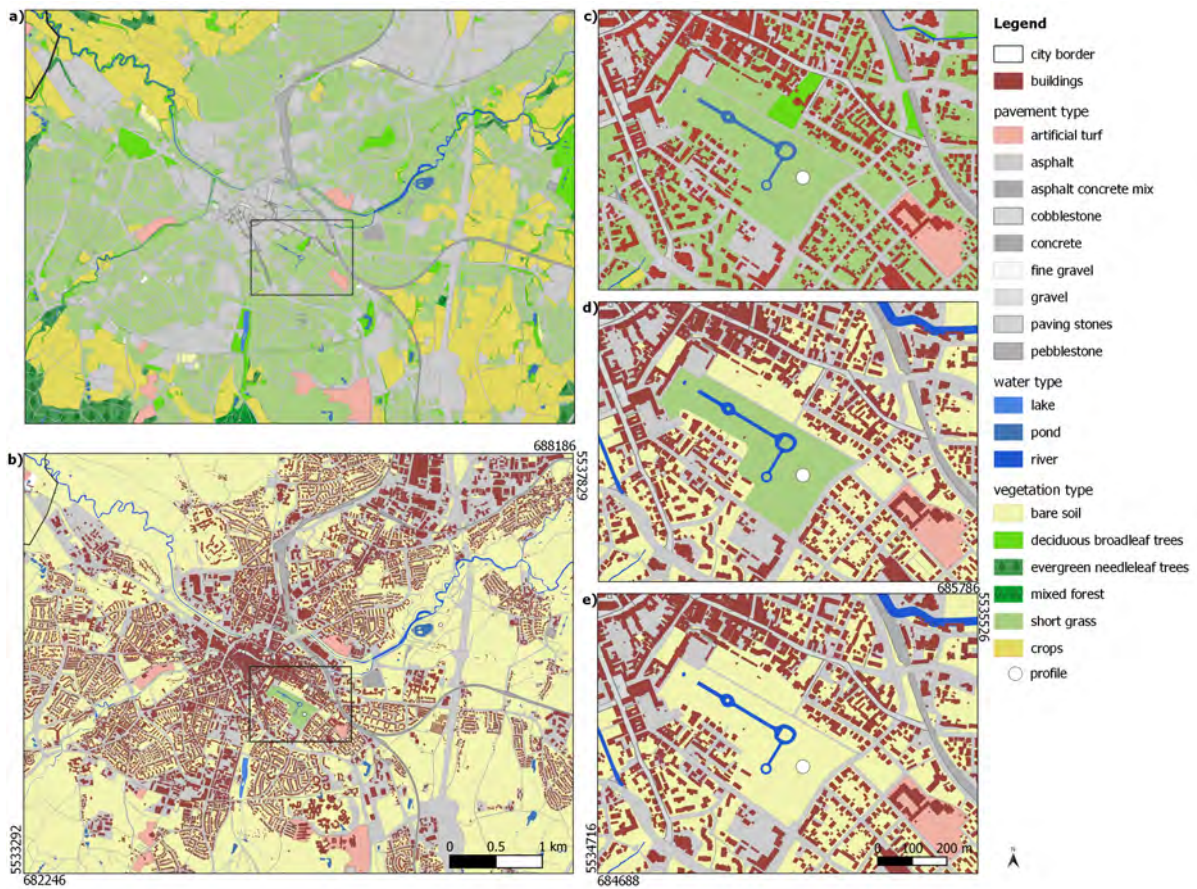


Figure 21: Visualization of scenario C in shapefile format. The maps on the left site depict the cutout of the domain that is used for the analysis. The snippets on the right picture the versions C.1 and C.2 and the corresponding cut out of the base run.

data. The most influential parameters and fluxes such as the air temperature, potential temperature, perceived temperature, specific humidity, latent heat flux, sensible heat flux, and the outgoing shortwave and longwave radiation are shown in the results of this thesis. To identify heat effects in the investigation area and for the applied scenarios, absolute- and difference plots were chosen. While the absolute figures show the respective absolute amount per parameter, the difference plots show the difference of the scenario - base run. To assess the differences of the respective parameters or fluxes on the spatial scale of the domain, a spatial difference was computed. To assess UHI effects by the spatial difference for the entire domain, a spatial mean value was calculated that excluded the area of the more densely populated city. The cropped extent resembles the extend of the Figure 23. The matrix of the spatial mean was then subtracted from the matrix of the entire domain. For the assessments of spatial differences in the simulations of the scenarios,

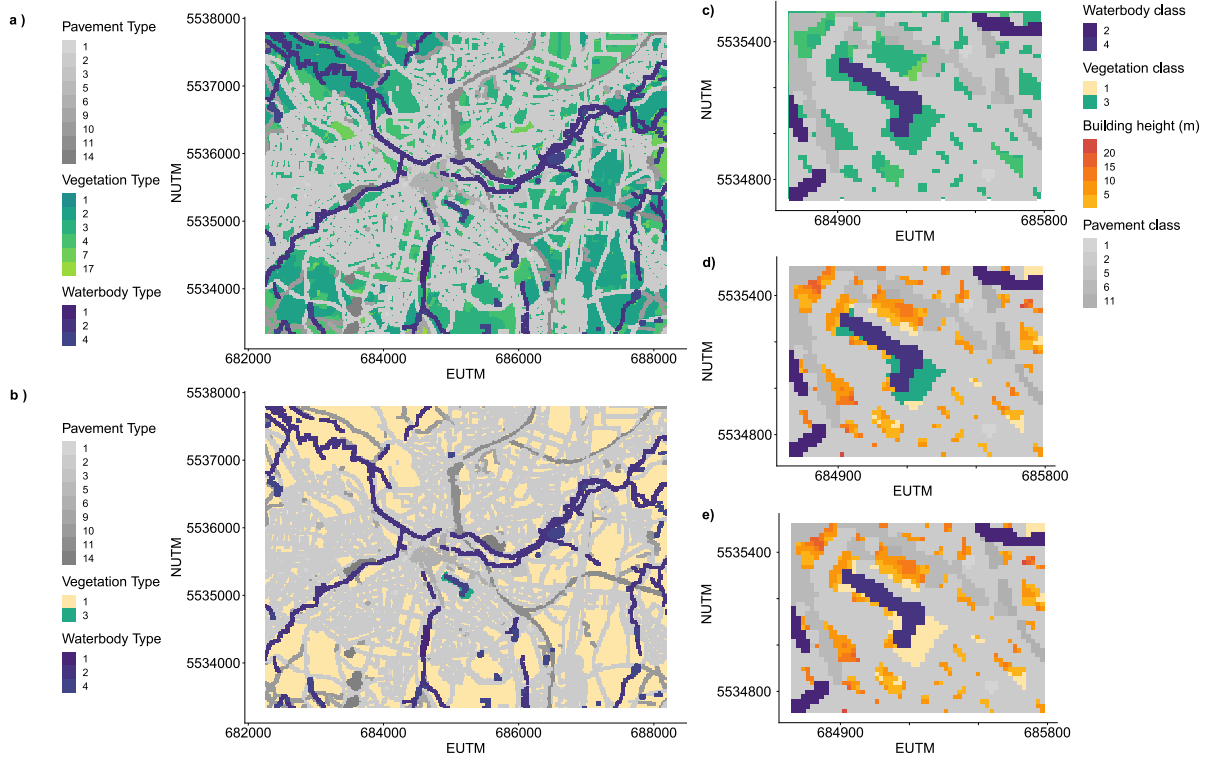


Figure 22: Visualization of scenario C (cf. Fig.21) in NetCDF, 20 m resolution, input into PALM. The legends display the bulk land-use type codes for PALM4U which belong to the files.

individual spatial means were calculated across the scenario cutouts and the spatial mean cutout matrix was subtracted from the cutout matrix of the particular scenario. Besides, time height cross-section profiles were computed over homogenous surfaces, to examine whether the stable boundary layer is adequately reproduced by PALM. A difference for the profiles of the scenarios was also calculated, subtracting the base run profiles of the respective locations by the profiles from the scenario simulations. PALM4U can give out three dimensional (3D) data, but the computing power and ram capacities are enormous. For this reason, the output of 3d data was neglected, and xy, yz, and xz cross-sections were taken instead. The xy surface can be plotted as the entire area, whereas the yz and xz dimensions appear in discrete cross-sections that had to be selected before the simulation process started (cf. Fig. 23). For the analysis of the xy cross-section output parameters, three times distributed over a 24-hour cycle were chosen from the full 26-hour simulation run: 16:00, 20:30, and 4:30 CET.

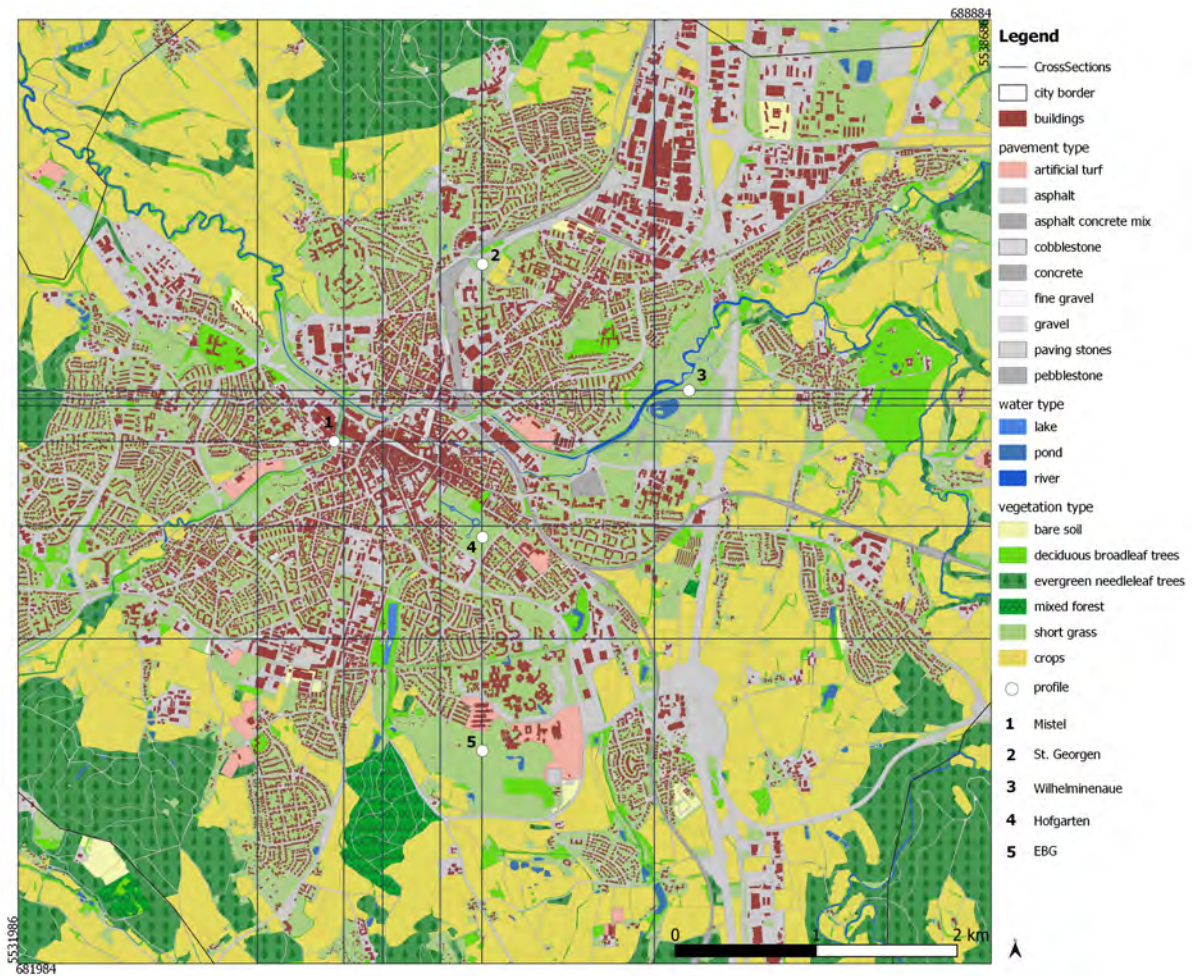


Figure 23: Cross Sections in xz and yz dimension depicted from a domain cutout of the core area of Bayreuth. The white points indicate the coordinates where the profiles are taken.

4. Results and Discussion

4.1. Temperature distribution and anomalies in and around

Bayreuth

The simulated perceived temperature of the xy cross-section from the base run shows a maximum of 40.0 °C at 16:00 (cf. Fig. 24). This maximum is located on the elevated hills in the northwest, east, southeast, and southwest of the domain (cf. Fig. 24). The perceived temperature maxima concentrate in the northern part of the industry area north of Bayreuth (cf. Fig. 24). For Bayreuth, no clear heating pattern is observed for perceived temperature. There is one hotspot in the northern part of the city (St. Georgen, cf. Fig. 25). Coolest spots are the locations offering water surfaces, especially the floodplain in the northeast (Wilhelminenaue, cf. Fig. 25). In addition, the Roehrensee lake and the Mistel river in the west of Bayreuth are depicted as cool spots. In the surroundings of Bayreuth, the eastern area adjacent to the highway shows a lower perceived temperature difference by approximately 8 K degrees. The simulated perceived temperature and air temperature spatially match in their minima and maxima. Maximum values are especially pronounced at the elevations in the northwestern and eastern surroundings. Air temperature reflects additional high values for the highway in south-north conjunction. Pavement surfaces reach 39 °C, which is higher than reflected by the perceived temperature (36 °C).

Minimum values are the water surfaces and areas already represented by the perceived temperature. For Bayreuth, maximum air temperature is also simulated for the particular locations where buildings are positioned.

During nighttime (cf. Fig. 24b, d) two large cold air pools form in the simulated perceived temperature. First, the floodplain of the Roter Main, situated in the northwest of Bayreuth, stores cold air and serves as drainage. Another distinctive assemblage of cold air masses is located east of Bayreuth, along the river bed of the Roter Main. Especially the floodplain of the Wilhelminenaue and the area at the east side of the highway keep cold air masses. The east boundary however, is perceived much warmer. The air temperature simulations during the night agree with the cold air pools located at the eastern floodplain of Wilhelminenaue and the river bed along the Red Main. The difference in air temperature variations is identical to the variations of perceived temperature ($\Delta 4$ K, cf. Fig. 25). More cold air pools are detected in Figure 25d and

the cold air pool of the floodplain in the northwest is not as large. Regarding Bayreuth, the model simulates a difference of 3 K between vegetated and paved surfaces for air temperature (cf. Fig. 25). The assessment of heating patterns is restricted by the given

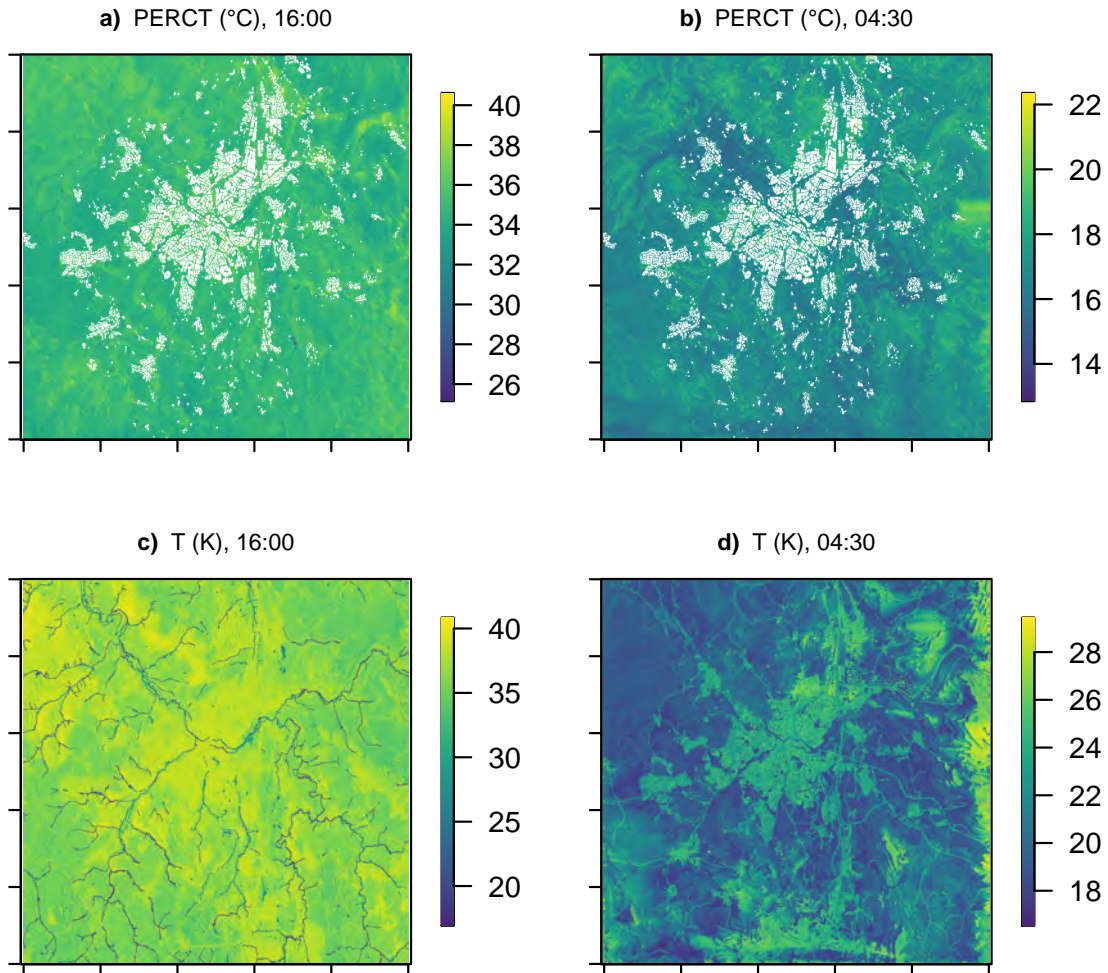


Figure 24: Overview of a) perceived temperature in °C at 16:00 CET, b) perceived temperature in °C at 4:30 CET, c) air temperature in Kelvin at 16:00 CET, d) air temperature in Kelvin at 4:30 CET. The plot area corresponds to the entire domain of the simulation.

resolution of 20 m, which is not suitable to resolve street canyons properly. Several of the canyons are represented by just a few pixels. These are hardly sufficient for PALM to develop turbulent flow feedback and generate an adequate reproduction of realistic conditions. Perceived and air temperature both are simulated for 10 m above the surface. The attempted height for perceived temperature computations from PALM is the cell level closest to 1.1 m above ground level surface ((Maronga et al., 2019). However, to reach a near surface value is only possible with a fine resolution grid. For this simulation,

the middle of the first cell size is located at 10 m. The hotspot in the north however, appears reasonable to show higher perceived and air temperatures since this part of the city is more elevated and does not offer much green space. Local impacts on the radiation balance (cf. Section 3.6) are expected. The heating potential of a site is controlled by the absorption, heat storage, and longwave emission of a surface, which are given by the material properties (cf. Section 3.6). St. Georgen has an old town square with dark cobblestone of a low albedo. Low albedo, in return, leads to a higher surface temperature. High surface temperatures are efficiently conducted into the ground by large heat conductivities. Heat capacity in the city is relatively small compared to wet soil which leads to a deep warming. This reservoir is then expected to increase surface and near-surface air temperatures at night.

When comparing the results, it has to be considered that the figures of perceived temperature do not display any building data in contrast to the plots showing air temperature. The air temperature was calculated from the output of the potential temperature and the virtual potential temperature in PALM4U. In contrast to the xy cross-section of perceived temperature, the building information is not spared in the air temperature cross-section of the surface. This also applies to all other parameters printed in the xy cross-section. Therefore, buildings' surface attributes are considered as surface land-use pixels by PALM which is not realistic for the near-surface atmosphere. However, this applies to the pixel of buildings only and can be accounted for when interpreting the results. Another bias results from the choice of resolution: In this case, the first output is given at 10 m NN, respectively for every parameter variable. The WMO standard for the measurement of city climate parameters is at 2 m above the surface.

The spatial distribution of thermal differences is very valuable to detect temperature hot spots in Bayreuth (cf. Fig. 24, 25). In the following, the spatial mean of perceived and air temperature of the surroundings is further observed and compared to the temperatures in Bayreuth. The spatial mean of the perceived temperature in Figure 26 is 34.9 °C. As comparison, the spatial mean for the entire domain including the area of Bayreuth and surroundings is identical (34.9 °C). The spatial mean of only the inner domain cutout (Bayreuth) is 35.1 °C. The sealed areas in the city are much warmer than the spatial mean. In Figure 26 the cool water surfaces clearly stand out. Afternoon temperature deviations reach a difference of + 5 K for the inner-city compared to the spatial mean

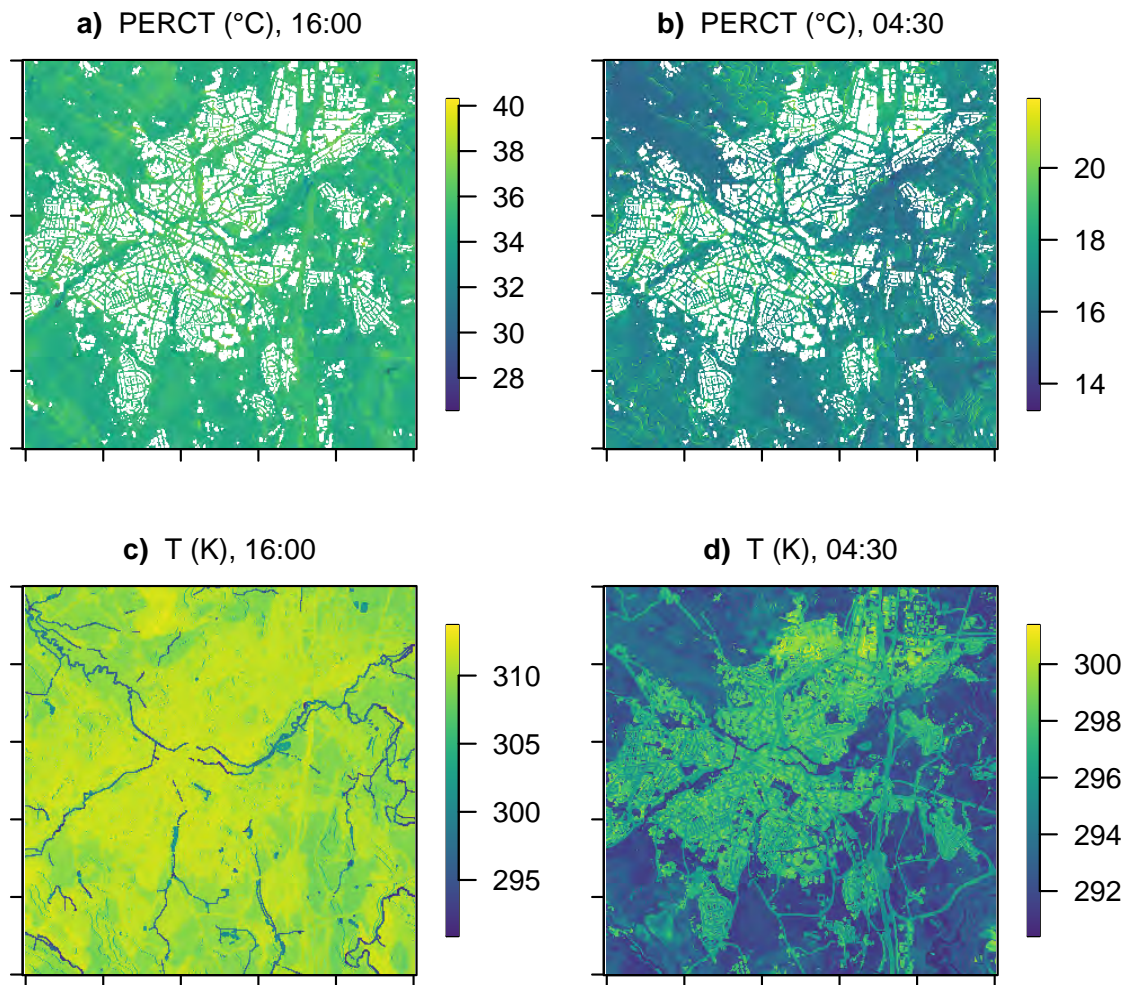


Figure 25: Overview of a) perceived temperature in $^{\circ}\text{C}$ at 16:00 CET, b) perceived temperature in $^{\circ}\text{C}$ at 4:30 CET, c) air temperature in Kelvin at 16:00 CET, d) air temperature in Kelvin at 4:30 CET. The plot area resembles a cutout of the entire domain of the simulation (cf. Fig. 23).

of the domain. Temperature deviations for the elevations in the surroundings reach a difference of up to 10 K. The spatial mean of Figure 26 is 35.5°C , whereas the cutout of Bayreuth has a mean air temperature of 36.5 .

The spatial mean of the surroundings is therefore taken as an eligible metric to compare the perceived and air temperatures within Bayreuth to the respective temperatures of the surroundings. This way, the UHI effect can also be considered. Highest thermal differences in perceived as in air temperature agree with those spots of the surroundings where the warmest temperatures concentrate(cf. Fig. 26). The sites with maximum negative deviation do not follow a particular pattern. Often, they are located at transitions to hilly areas.

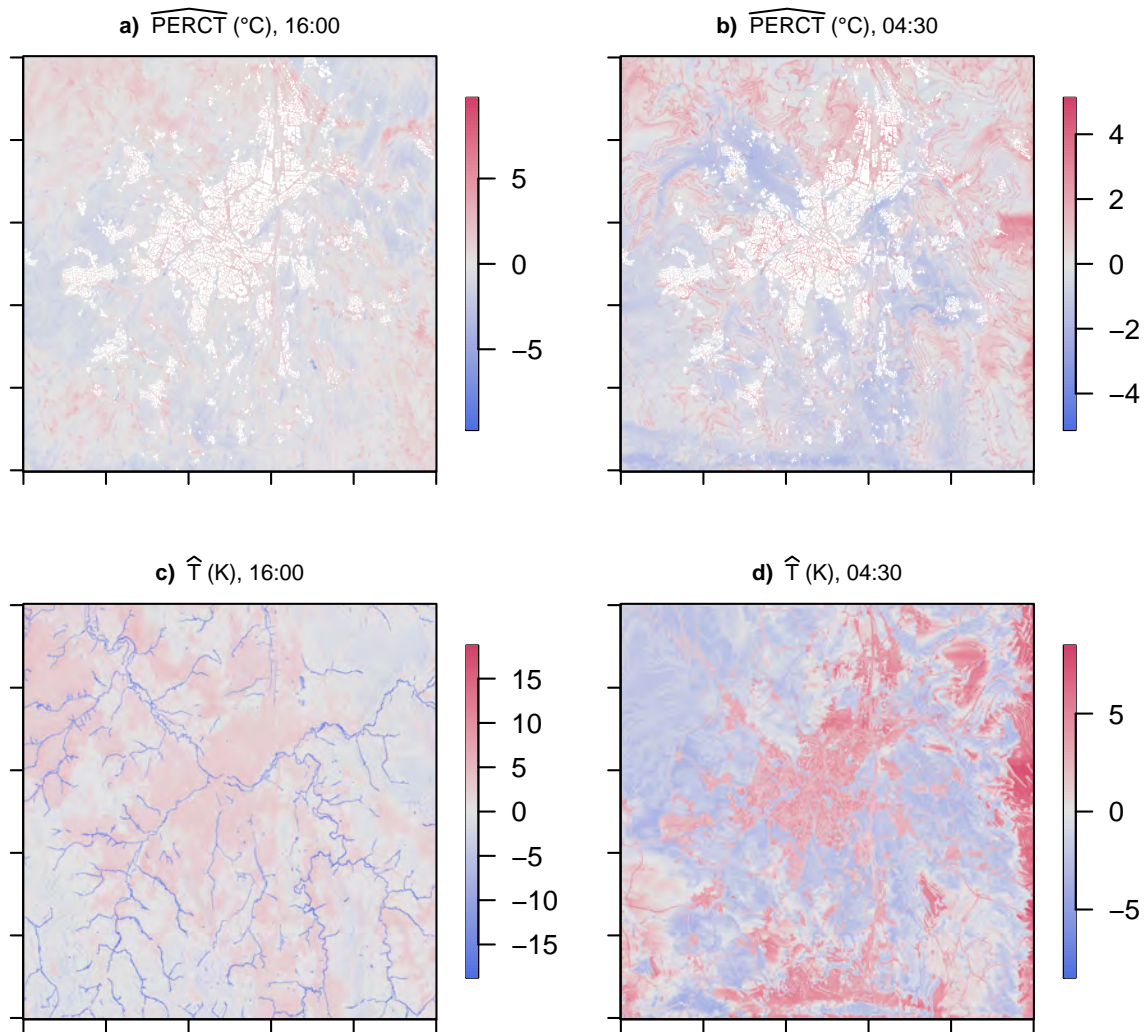


Figure 26: Overview of a) the mean spatial deviation of perceived temperature in °C at 16:00 CET, b) the mean spatial deviation of perceived temperature in °C at 4:30 CET, c) the mean spatial deviation of air temperature in Kelvin at 16:00 CET, d) the mean spatial deviation of air temperature in Kelvin at 4:30 CET. The spatial mean was computed by neglecting the extent of Fig. 25 from Fig 24. This value was then subtracted from each pixel of Fig. 24 and plotted with a scale of the maximum difference values. The plot area resembles the entire domain of the simulation.

For nighttime, thermal differences in perceived temperature reach up to 4 K across the domain. The mean of perceived temperature in Figure 26 is 17.2 °C. It is identical (17.2 °C) for the spatial mean of the entire domain and 17.1 °C for Figure 27. Air temperature distribution across the domain shows a difference of +5 K for Figure 27d. The mean of air temperature across Figure 26 is 20.9 °C, whereas the mean for Figure 27 is 21.0 °C. Figure 27 reflects identical cold air pools for perceived and air temperature. Especially

the industrial area in the northeast from Bayreuth (cf. Fig. 27) experiences higher perceived temperatures than the mean. A comparison of Figure 27a and Figure 27b shows differences in the illustration of the highway. It shows a difference of + 4 K during daytime, whereas it corresponds to the spatial mean during nighttime. Another difference between Figure 27a and Figure 27b can be observed for the simulated perceived temperature above the Hofgarten. This shift is not reproduced in the simulated air temperature (cf. Fig. 27d). The topography of the model is not interpolated at a continuous scale,

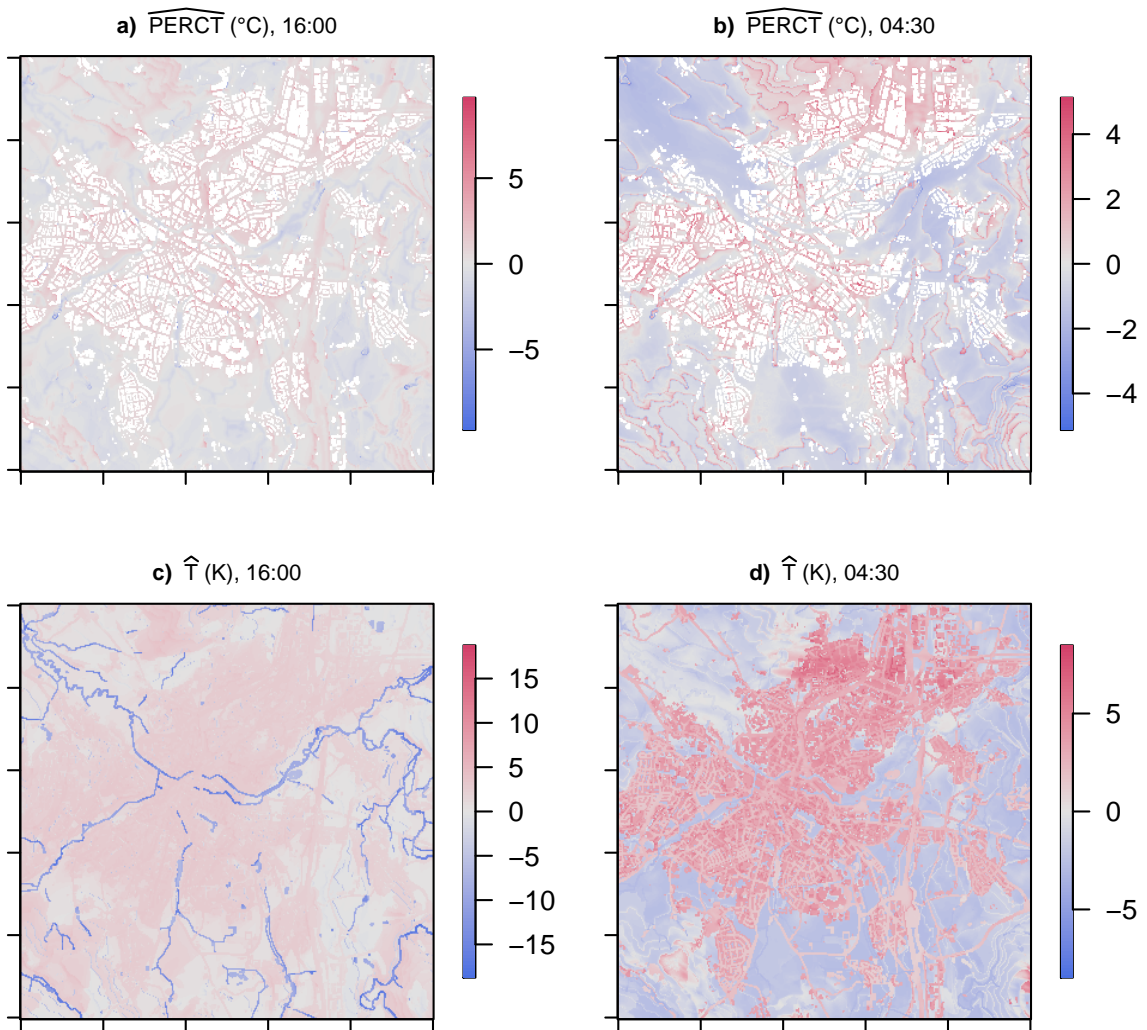


Figure 27: Overview of a) perceived temperature in $^\circ\text{C}$ at 16:00 CET, b) perceived temperature in $^\circ\text{C}$ at 4:30 CET, c) air temperature in Kelvin at 16:00 CET, d) air temperature in Kelvin at 4:30 CET. The plot area resembles a cutout of the entire domain of the simulation.

which leaves differences in altitude highlighted due to sudden high transitions that take effect on the plotted parameters. Thermal differences up to 5 K are above land surfaces,

especially in the core of Bayreuth and the ring road. The effect of elevated temperatures for the highway in Figure 27 is due to high radiative forcing on a concrete and asphalt mix which stores much heat over day (cf. 3.6). The urban effects that are relevant for the temperature differences at the Hofgarten are different. Here, the Hofgarten being encircled by buildings is influenced by the heat capacity of the buildings (cf. 3.6). The Hofgarten in the simulation is not able to effectively develop a park cool island effect, but is instead affected by the energy stored in buildings over day. The buildings consist of materials with a high heat capacity which released heat at night (cf. 3.6). This is an urban effect very much related to the UHI effect.

The UHI of Bayreuth can be distinguished in Figure 26 b, d, and Figure 27 a, b and d. The UHI is especially pronounced during nighttime, where the difference between maximum temperature and minimum temperature is bigger than during the afternoon. This effect is expected as the specific heat capacity of buildings, and densed agglomeration areas such as cities, is very high. This energy, stored in much of the infrastructural material used in Bayreuth, is released once the air temperature is cooling down. As a result, a higher local sensible heat flux persists. Hot spots are especially the northern industrial area and the southwestern part of the city. The river Mistel, which is flowing through this city quarter, does not have much impact on the air and perceived temperature in the simulation. Thus, there it is not providing a cooling effect on the heat in the adjacent city quarter. This is against expectations, as the temperatures directly above the Mistel river are much cooler than its direct environment. Also, the results from the observations of the MiSKOR network (Lueers and Thomas, 2021) proved the Mistel river bed as a cold finger. Supposably, this is one example for the neglection of local urban effects by the coarse resolution of the simulation.

4.2. PALM4U reproduction of physical magnitudes and micrometeorological conditions

For modeling, it is indispensable to create a reliable virtual simulation environment. For the simulation runs to be applicable for city planning measures, the virtual simulation environment built by the PALM4U model must be able to display a biophysical reproduction of Bayreuth in terms of physical output magnitudes.

The results from the thermal spatial deviation across the domain are confirming the

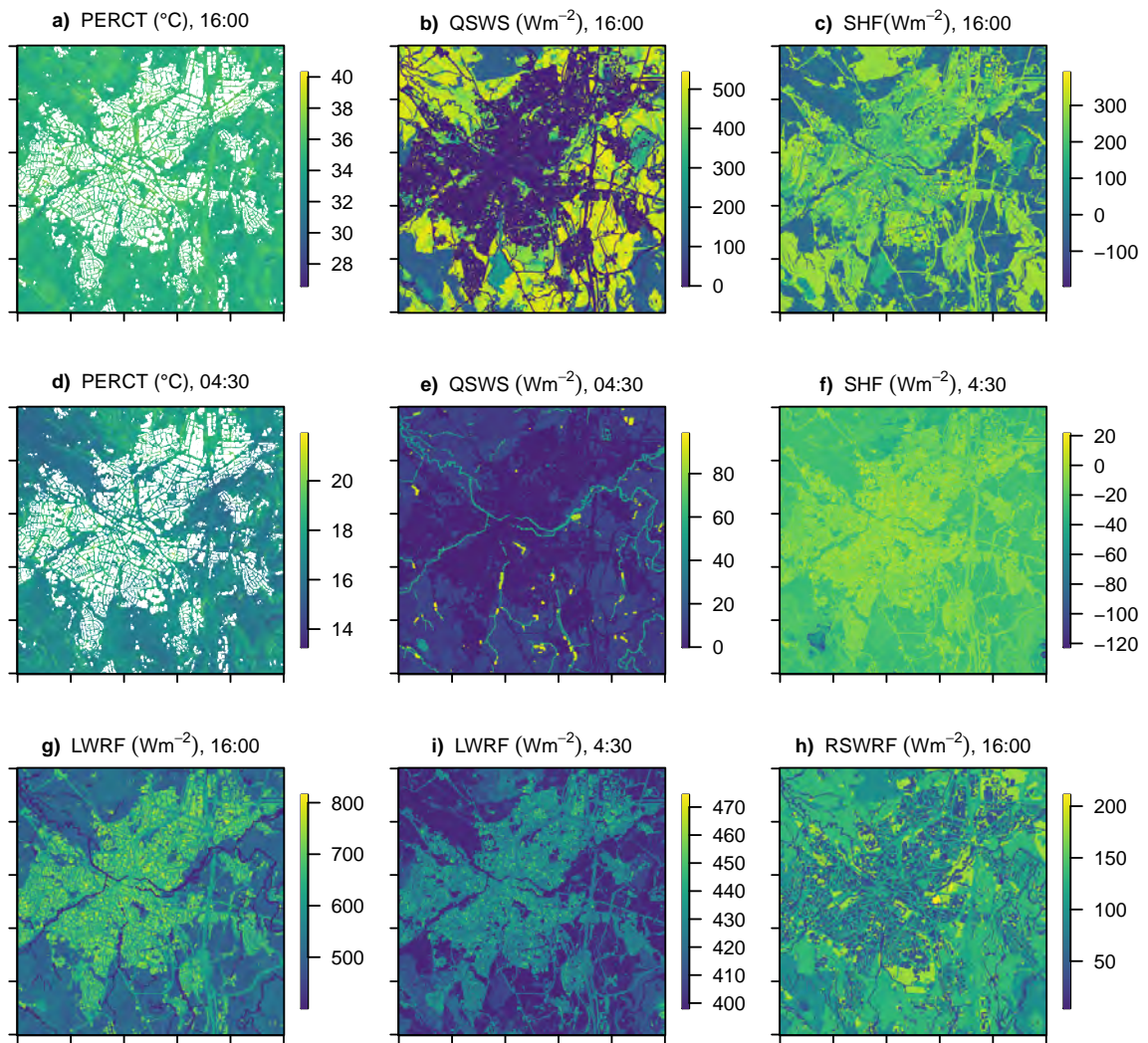


Figure 28: Overview of physical magnitudes of the output data for the base simulation of Bayreuth in 20 m resolution. a) perceived temperature in $^{\circ}\text{C}$ for the simulation at 16:00 CET, b) latent heat flux in Wm^{-2} simulated at 16:00 CET, c) sensible heat flux in Wm^{-2} simulated at 16:00 CET, d) perceived temperature in $^{\circ}\text{C}$ for the simulation at 4:30 CET, e) latent heat flux in Wm^{-2} simulated at 4:30 CET, f) sensible heat flux in Wm^{-2} simulated at 4:30 CET, g) outgoing longwave radiation flux in Wm^{-2} simulated at 16:00 CET, h) outgoing longwave radiation flux in Wm^{-2} simulated at 4:30 CET, i) outgoing shortwave radiation flux in Wm^{-2} simulated at 16:00 CET. A cutout of Bayreuth is presented.

findings of Spies (2019). The absolute and difference values for perceived and air temperature agree with each other and are in line with the report from the DWD DWD (2019, p. 5, 8)). Examining the absolute parameter values of perceived temperature, latent heat flux, sensible heat flux and radiation fluxes in Figure 28 gives information about the physical magnitudes of the quantities simulated for Bayreuth from PALM4U.

At 16:00, the latent heat flux reaches its maxima of 500 Wm^{-2} over agricultural land surfaces. Short grassland surfaces show a latent heat flux of approximately 400 Wm^{-2} , whereas forest areas show 300 Wm^{-2} . The simulated latent heat flux above water surfaces at 16:00 shows $+ 100$ to $+ 200 \text{ Wm}^{-2}$. The latent heat flux is very small above sealed surfaces (cf. Fig. 28b). The outgoing longwave radiation flux at 16:00 shows values of $+ 800 \text{ Wm}^{-2}$ above paved surfaces and building material. It has a minimum of $+ 50 \text{ Wm}^{-2}$ and maximum values of $+ 200 \text{ Wm}^{-2}$ (cf. Fig. 28h). The reflective shortwave radiation flux shows lowest albedo values for buildings and water surfaces (cf. Fig. 28i). For the simulated time at 16:00, pavement and vegetated surfaces reflect $100 - 120 \text{ Wm}^{-2}$ (cf. 28i). The Hofgarten has an elevated reflection rate of $+ 170 \text{ Wm}^{-2}$ (cf. 28).

During nighttime, the latent heat flux reaches a maximum of 80 Wm^{-2} above non-circulating water surfaces (cf. Fig. 28e). Moving water surfaces such as rivers show a latent heat flux of 60 Wm^{-2} , whereas all other open land-use surfaces are distinctively lower (cf. Fig. 28e). The sensible heat flux at 4:30 is largest above building- and sealed pavement area, reaching up to 300 Wm^{-2} (cf. Fig. 28f). It is lower for all vegetated areas, especially the forest and water surfaces. The sealed surfaces of Bayreuth show a positive sensible heat flux value of $+ 20 \text{ Wm}^{-2}$ (cf. Fig. 28f). The longwave radiation flux at night shows maximum values of 470 Wm^{-2} for the sealed area of Bayreuth (cf. Fig 28h).

The flux values above water surfaces seem to be low in absolute numbers and relation to the maxima occurring above the agricultural land surfaces. However, transpiration above agricultural land is expected to be high for extremely dry conditions, which applies to the heatwave period. Therefore, this value is quite reasonable, as is the order of the decreasing latent heat fluxes over land-use types. Cropland (not further differentiated in PALM4U) shows highest latent heat flux values, followed by the areas covered by short grass, followed by deciduous forest. Evergreen needleleaf forest has the lowest latent heat flux values ($+ 100 \text{ Wm}^{-2}$) of the vegetated land surface types and shows very similar values to water surfaces. Still, the water surface would be expected to reach higher latent heat flux values due to evaporation processes. One factor could be the roughness length which is larger above forest and water surfaces than arable land or short grassland. Still, this factor is not expected to have such a high influence, especially since windspeeds were very low within the simulation domain. Another reason could be the relatively

large difference between the very dry and hot air temperature and the cooler water surface temperature. As the ground heats up more quickly than the water, transpiration processes would be driven more quickly and reach higher values than evaporation above water surfaces. The reflective shortwave radiation flux depends highly on the surface material on which it reflects. The most reflective surfaces are open space short grassland areas, such as the EBG, the Wilhelminenaue, and backyards in the housing areas. The elevated reflection rate of the outgoing shortwave radiation flux for the Hofgarten must be considered under the given fact that there are no trees available for the simulation, and therefore PALM4U treats the Hofgarten as a short grass meadow.

During nighttime the water surface has a larger heating capacity and thus takes longer to cool down than the air and the ground surface. Latent heat flux values for 4:30 are reasonable since there is no incoming shortwave radiation that forces the latent heat flux during nighttime. This is an expected process resulting from the surface energy balance (cf. 3.6). During nighttime, the simulated sensible heat flux becomes very low and turns negative for the vegetated land surfaces. Negative sensible heat flux values are related to cool surfaces within atmospheric static stable conditions showing vertical temperature gradients (cf. Fig. 29, 30, 31). At night, the surface has a much smaller longwave downwelling radiation (cf. section 3.6) which causes a positive net radiation at the surface. This in return cools the surface and thus the sensible heat flux turns towards the surface as heat is transported from the air towards the surface. However, for very hot days as simulated, sealed surfaces are still emitting the stored heat from the day until late at night. The values for the outgoing longwave radiation flux are in line with the positive values of the sensible heat flux above buildings and paved areas and the negative values of the sensible heat flux above vegetated or water surfaces (cf. Fig. 28f).

Besides the xy cross-section surface data, the cross-sections for xz and yz show the full height of the domain. PALM4U needs not only to be capable of reproducing valuable magnitudes across the spatial extent for a single time, but moreover it also needs to be capable to reproduce meaningful vertical profiles. In this section, the profiles of potential temperature specific humidity, wind speed, and wind direction for the EBG, St. Georgen, and Wilhelminenaue (cf. Fig. 23) were selected as representatives of a densely vegetated, built, and open green space (cf. Fig. 29, 30, 31). The profiles of Mistel, Eichelberg, the west and the east of Bayreuth can be found in Figures B7, B6, B8 and B5.

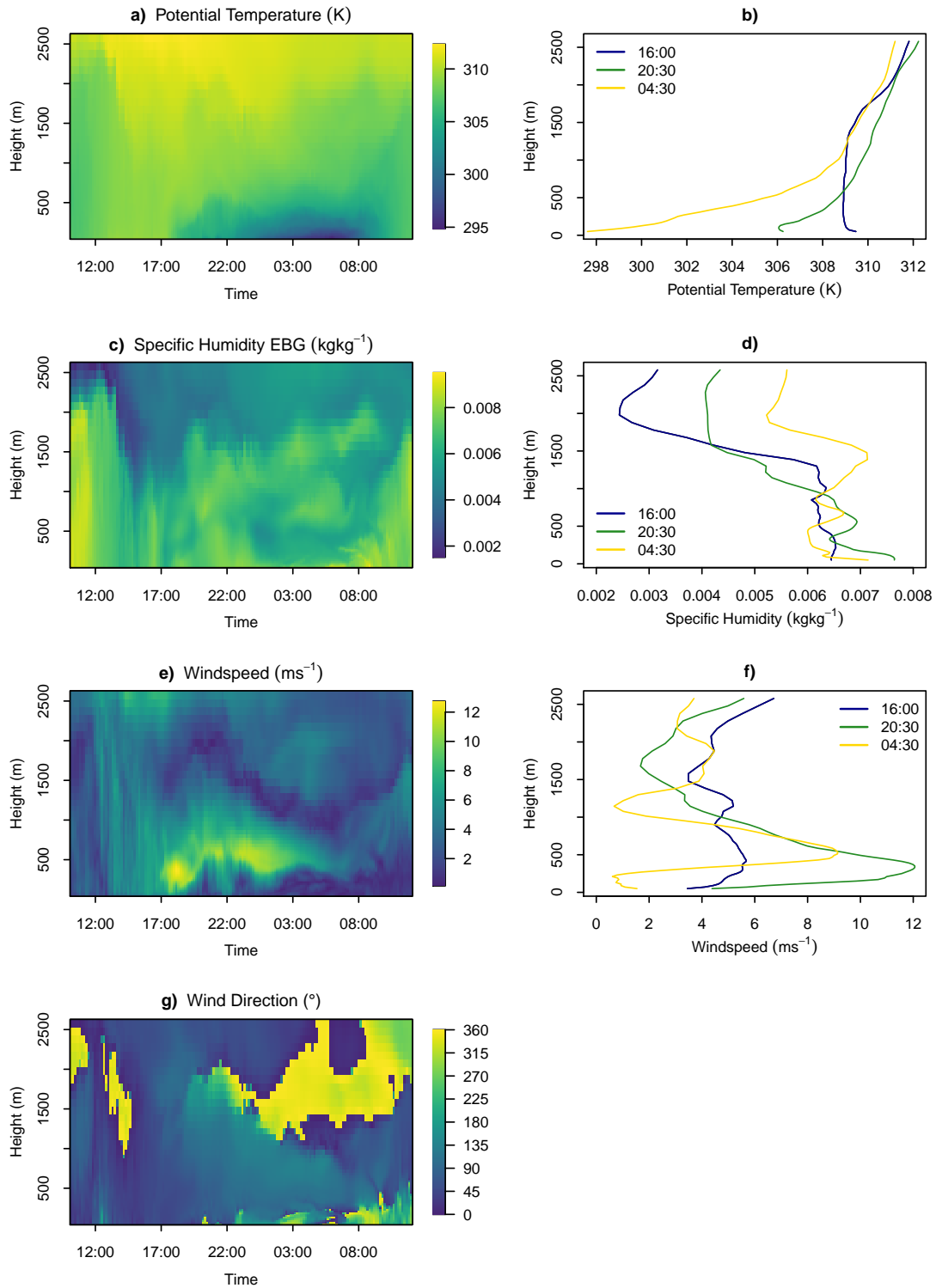


Figure 29: Simulated time height cross section and corresponding 2d profiles of the Ecological Botanical Garden. The profile was computed above a homogenous grassland surface. The time period shows the 26-hour interval of 07.25.2019 from 10:00 CET to 07.26.2019 12:00 CET. The height is referenced to 0 NN from the lowest point of the domain, the profile data starts at the respective height of the profile location. The range of height is selected until the height, where the profiles develop a stable boundary layer. a) potential temperature in Kelvin, b) specific humidity in kgkg^{-1} , c) windspeed in ms^{-1} , d) wind direction in degree.

The potential temperature simulated at the EBG increases until the afternoon and rises up to temperatures of 310 K throughout the complete height of the domain (cf. Fig. 29a). In the late afternoon, cooler air masses develop in the atmospheric boundary layer, but do not extend above 500-600 m above the surface. An arrangement of layers shows during night, forming the stable boundary layer above the surface, which diminishes on the next day's forenoon to a mixed layer again. The two-dimensional (2d) profiles at 16:00 show an unstable convectively mixed layer profile for the first 2000 m and then change to stable non-local static stability (cf. Fig. 29b). The profile for 20:30 is statically stable up from the height of approximately 300 m NN and the profile for 4:30 is statically stable across the entire depth of the domain. The very bottom of the 16:00 and 20:30 profiles is highly unstable. This instability can be explained by the roughness of the city infrastructure and the strong radiative heating that warms the air.

The simulated specific humidity above the EBG shows the transport of humidity up to 2000 m until noon (12:00, cf. Fig. 29c). This transport is capped by the mixed layer height and the mixed layer itself diminishes in the evening. The establishment of the stable boundary layer is during the night and transforms to a mixed layer starting with sunrise. Higher rates of humidity can thus be found in the layers closer to the surface. The 2d profiles depict meaningful height profiles of specific humidity and do not vary strongly between day and night.

The simulated wind speed above the EBG shows a convective mixed layer between 12:00 and 17:00, characterized by more vigorous turbulence than between 10:00 and 12:00 (cf. Fig. 29e). By 17:00 the onset of a low-level jet is at 500 m above the ground. The low-level jet involves higher wind speeds of 12 ms^{-1} closer to the ground (Banta et al., 2002) and a shield layer of very low wind speeds ($0 - 2 \text{ ms}^{-1}$) higher up in the atmosphere. The 2d profiles reflect the building up of the low level jet. The profiles of 16:00 and 20:30 start with a stable atmospheric layering but become unstable through the mixed layer. At the height of 2000 m, static stability is reached. The profile of 4:30 is influenced by the nocturnal jet and forms a stable boundary layer above 2500 m.

The simulated wind direction above the EBG is mostly forced by the wind from the northeast during the daytime. At the beginning of the afternoon, winds from the southwest enfold in the lower 1.5 km and prevail during the nocturnal cycle. Between 3:00 and 10:00, the height between 1.5 km and 2.5 km is mostly influenced by wind directions

from the north. In the lower atmospheric layers, the wind is forced mainly from the south and southeast, whereas the bottommost layer is a mix of wind directions coming from southwest, west, northwest, and north. The surrounding of Bayreuth has several smaller elevations which surely influence the lower local wind profile. Besides physical thermal processes and advection, the topography is likely to have a greater influence on the change of wind directions in the lower atmospheric boundary layer. The eddies in the lower 400 m above the surface are expected to be influenced by the roughness length of the city infrastructure.

A profile of the simulation across St. Georgen has been chosen because this part of the city was found to be one of the warmest of the MiSKOR measurement network. In accordance with the measurement data, the area around St Georgen and the northern industrial area further north of St. Georgen also turned out to be simulated hotter than the spatial mean in the PALM base run. Absolute temperatures of the PT profiles of EBG and St. Georgen share the same maximum but show a slightly higher magnitude of minimum temperature. The 2d profiles are similar for 20:30 and 4:30, whereas the profile at 16:00 shows more distinct unstable conditions compared to the one of the EBG. Given the similar structure of the 2d profiles, the differences between the EBG profile and the profile simulated in St. Georgen are expected to be rather small. Both profiles are captured above a grassland land-use in PALM4U.

The specific humidity time height cross-section is in line with the profile of the one taken above the EBG, as is the respective wind speed and wind direction of both profiles. The cross-section and 2d profiles of the Wilhelminenaue are very much alike the ones taken in the EBG and St. Georgen. This is an expected result, as the plots for once simulate a cross-section above several kilometers and thus look at the general composition of the model output at various locations. On the other hand, the underlying build-up of the domains' surface layers needs to be mentioned here again. The surfaces of the computed profiles were assigned in the static driver file. During the reclassification process of the raw data, several simplifications were made. Even though the overall distribution and relation of the different land surface types to each other are in line with the realistic conditions, not every respective location reflects the actual surface found. In return, local effects such as the ones of low level profiles are needed to be interpreted with respect to the model's setup and in context to the frame of the computing conditions.

Therefore, the similarity among the profiles is evidence for a biophysical distribution of the meteorological magnitudes among the time and height in the atmosphere. For the detection of local differences and effects, examination on a finer scale is needed. This would be the lowermost meters above the surface.

In summary, the absolute values for the base run simulation are valuable. The model thus can represent the proper magnitudes of the physical input parameters applied. The time height cross-section profiles show the mixed layer between 10:00 and 17:00 CET, and the forming of a stable boundary layer overnight. Processes occurring within such as low level jets and nocturnal jets can be observed. The 2d profiles show a convective mixed layer over daytime which is evidence for nonlocal static instability. This condition becomes capped by a static stable layer that develops at approx. 2500 m. PALM4U is forced through the interpolated COSMO model with a much coarser grid of 2 km times 2 km. With respect to external nested synoptic input data and the coarse resolution of 20 m of the domain, the given results seem to be physically plausible.

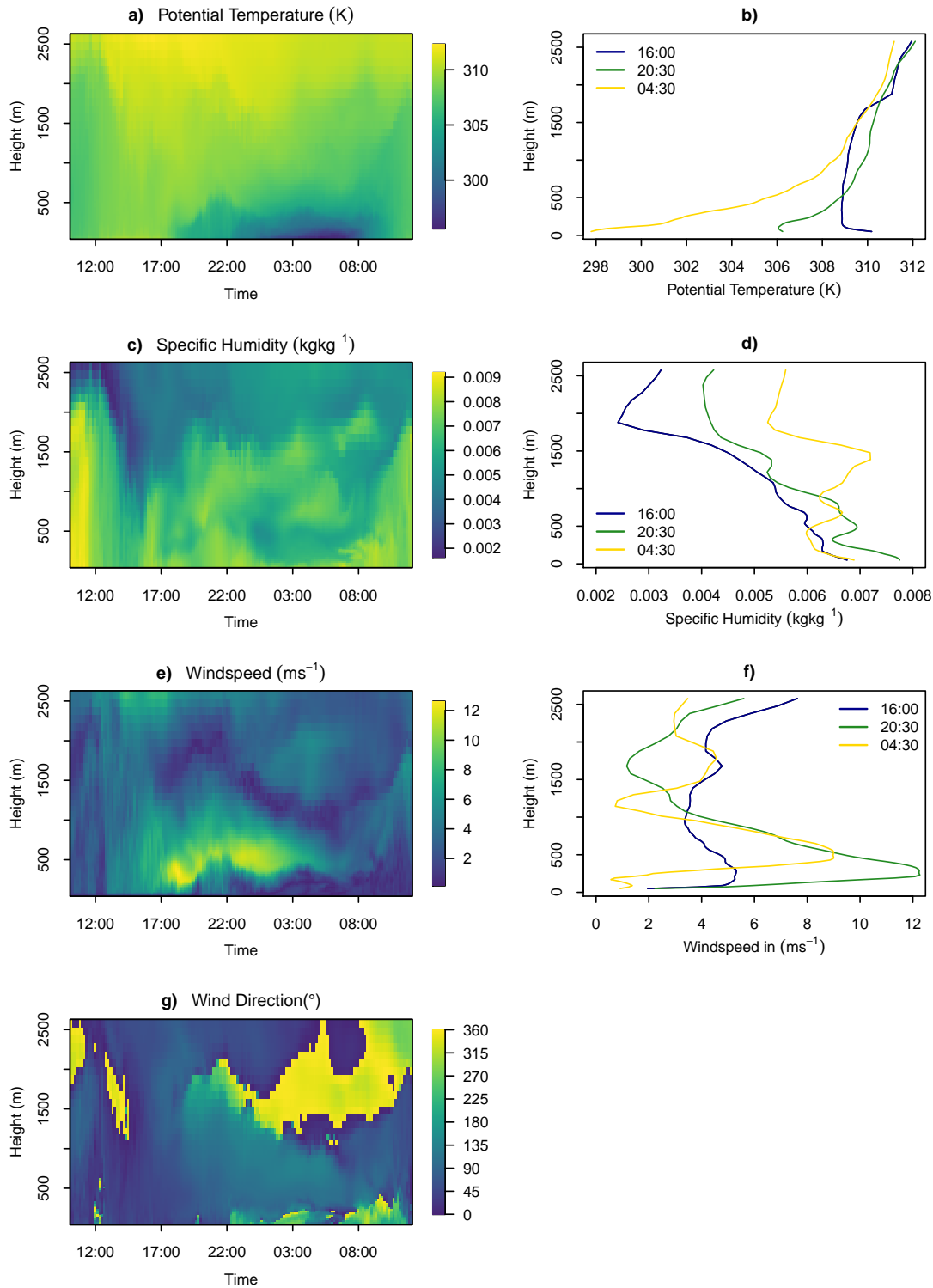


Figure 30: Simulated time height cross section and corresponding and 2d profiles of St. Georgen. The profile was computed above a homogenous grassland surface. The time period shows the 26-hour interval of 07.25.2019 from 10:00 CET to 07.26.2019 12:00 CET. The height is referenced to 0 NN from the lowest point of the domain, the profile data starts at the respective height of the profile location. The range of height is selected until the height, where the profiles develop a stable boundary layer. a) potential temperature in Kelvin, b) specific humidity in kgkg^{-1} , c) windspeed in ms^{-1} , d) wind direction in degree.

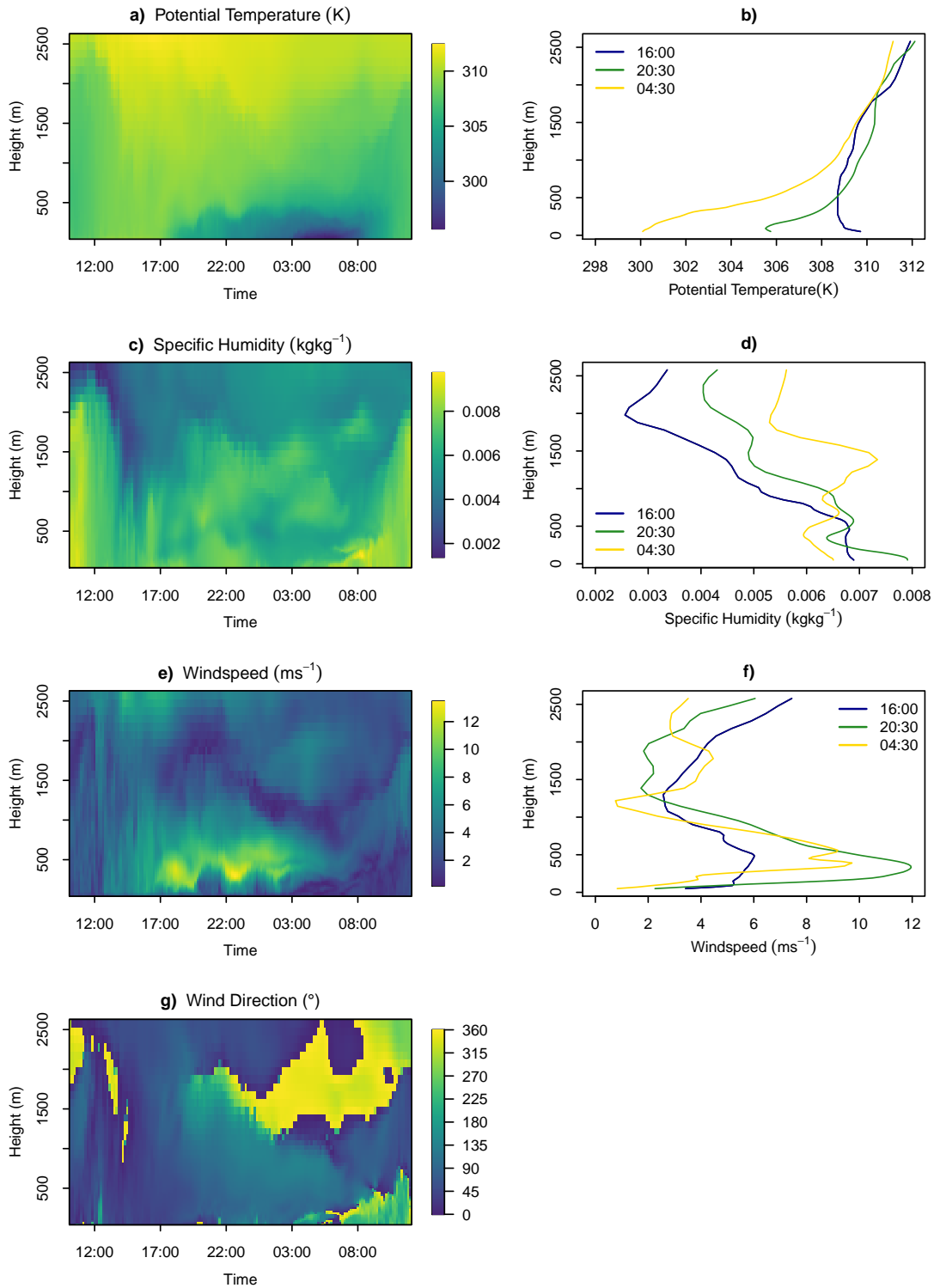


Figure 31: Simulated time height cross-section and corresponding and 2d profiles of the Wilhelminaue floodplain. The profile was computed above a homogenous grassland surface. The period shows the 26-hour interval of 07.25.2019 from 10:00 CET to 07.26.2019 12:00 CET. The height is referenced to 0 NN from the lowest point of the domain, the profile data starts at the respective height of the profile location. The range of height is selected until the height, where the profiles develop a stable boundary layer. a) potential temperature in Kelvin, b) specific humidity in kgkg^{-1} , c) windspeed in ms^{-1} , d) wind direction in degree.

4.3. Tested Scenarios

Scenario A indicates a change in the amount of surface water. This scenario was developed on the idea to simulate a recultivated river bed of the Roter Main. Certainly, the scenario applied in the simulation is much simplified and cannot be equated with the mitigation that would occur if a real recultivation were carried out. However, the application of models allows us to investigate changes to the current surface water bodies. Scenario A shall therefore test, how much of a change the surplus of water surface induces. Results show a large amount of building data within the domain. A possible explanation would be a bias in the layering of land use files while computing the static driver. Except for the blocking of street canyons, there is no direct impact by this bias as scenario A focusses on water surfaces, which are pictured as intended. Nevertheless, the computation of a Bowen Ratio would lead to misleading assumptions and has therefore been omitted.

Scenario B indicates a change in the colour of roofs and outer house walls. A new white coat of paint on all houses is estimated to increase the albedo to 0.8. This scenario is based upon the assumption, that a significant increase in the reflective shortwave radiation flux will prevent a great amount of heat storage in building material. Therefore, this scenario is expected to mitigate heat effects on a city-wide scale and to have a cooling effect on the air and perceived temperature. The simulation of scenario B was realized, but did not show any differences compared with the base run. Hence, scenario B failed its intention due to unknown technical difficulties and thus is not further analyzed.

Scenario C simulates a change of the vegetated land cover in the model domain. It shall aim to adopt extreme drought stress conditions. Local properties like precipitation, irrigation, and the soil moisture of vegetated areas have an important influence on thermal variabilities on a small spatial scale. The thermal effectiveness of green space, especially when it is open-spaced, is influenced as the effect and the factor of cooling by evapotranspiration depends on the water availability. To evaluate the current effect of the vegetated areas in Bayreuth, scenario C shall simulate conditions under extreme drought stress. Additionally, the potential of large urban green spaces such as the Hofgarten shall be investigated. Therefore, a subdivision of the scenario has been undertaken in scenario C: Scenario C.1 represents all vegetated land surfaces as bare soil. Scenario C.2 represents all vegetated land surfaces as bare soil, except for the Hofgarten.

4.3.1. Scenario A

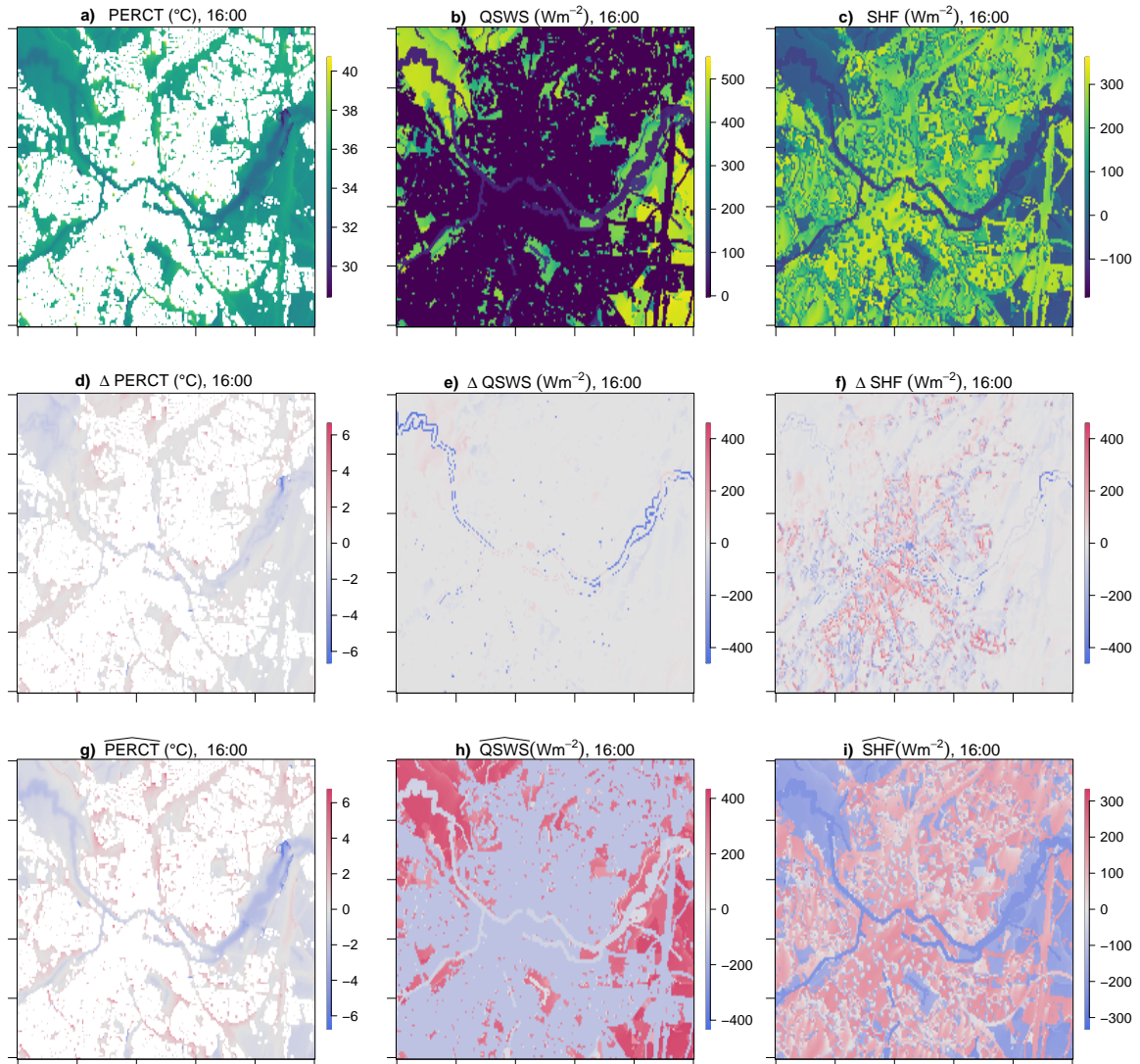


Figure 32: Overview of absolute and difference magnitudes for scenario A. For the difference magnitudes d) - f), the base run matrix is subtracted from the scenario matrix. For the difference magnitudes g) - i), the spatial mean is calculated across the depicted cutout. a) perceived temperature in $^{\circ}\text{C}$ for the simulation at 16:00 CET, b) latent heat flux in Wm^{-2} simulated at 16:00 CET, c) sensible heat flux in Wm^{-2} simulated at 16:00 CET, d) Δ perceived temperature in $^{\circ}\text{C}$ for the simulation at 16:00 CET, e) Δ latent heat flux in Wm^{-2} simulated at 16:00 CET, f) Δ sensible heat flux in Wm^{-2} simulated at 16:00 CET, g) $\widehat{\Delta}$ perceived temperature in $^{\circ}\text{C}$ for the simulation at 16:00 CET, h) $\widehat{\Delta}$ latent heat flux in Wm^{-2} simulated at 16:00 CET, i) $\widehat{\Delta}$ sensible heat flux in Wm^{-2} simulated at 16:00 CET. The cutout represents the core of Bayreuth from the entire simulated domain.

The results of scenario A show perceived temperature ranges between 36°C and 38°C

°C above land surfaces for the simulation at 16:00 (cf. Fig. 17a). The water surface is depicted with a range of 30 °C - 32 °C (cf. Fig. 17). The comparison between scenario A and the base run shows that there is no difference in perceived temperature, latent heat, and sensible heat flux above water surface (cf. Fig. 35, Fig. 32d-f). The edge of the river bed shows a difference of -2 °C in perceived temperature. As the absolute values for the locations with water surfaces of Figure 28 and Figure 32 are the same for perceived temperature, no difference can be depicted in Figure 32d. The thermal difference of the spatial mean of scenario A shows cooler areas of - 4 °C to -5 °C for the Roter Main, and of 0 to -2 °C around the river bed northwest in the cutout and east of the Wilhelminenaue (cf. Fig. 32d). No effect can be recognized for the inner-city area (cf. Fig. 32d). The air temperature in scenario A has the same range and spatial distribution as the air temperature in the base run (Fig. 35). Values of the latent heat flux for scenario A are similar to the distribution of the latent heat flux values from the base run (cf. Fig. 32b, Fig. 28b) for the simulation at 16:00. The difference between scenario A and the base run shows a cooling of latent heat flux by - 400 Wm⁻² above the edge for the missing river bed pixels for the sections outlying the inner-city (cf. Fig. 32e). Latent heat flux values show a warming of + 200 Wm⁻² for missing river bed pixels located in the inner-city area (cf. Fig. 32e). Individual segments do reflect warming on the one side and cooling on the other side of the river bed. The spatial distribution of latent heat flux differences shows no deviation for the Roter Main (cf. Fig. 32h). The cityscape has smaller values of - 200 Wm⁻² compared to the mean. The direct surrounding of the river bed has a positive deviation of 200 Wm⁻² (cf. Fig. 32h). The surrounding vegetated land surface shows a deviation of 400 Wm⁻² (cf. Fig. 32h). The spatial difference of the river bed edges is not pronounced enough to show any effect. The cityscape shows negative latent heat flux values (cf. Fig. 32h). Values of the sensible heat flux are identical to the distribution of those of the base run (cf. Fig. 32c, Fig. 28c) for the simulation at 16:00. The difference in sensible heat flux between scenario A and the base run shows a cooling of - 400 Wm⁻² for the flooded Anney square. The spatial distribution of the sensible heat flux throughout the cutout shows a negative deviation above the Roter Main (cf. Fig. 32i). The values of the simulated perceived temperature regarding water seem to be unrealistic for flowing water (cf. Fig. 32). Hence it is supposed that the perceived temperature is the one temperature above the water surface, but not the water surface itself. For comparison,

Figure 28a shows the water surface in the same range. Therefore, only those pixels are affected that result from the additional buffer of water pixel set in scenario A to enlarge the river bed in the simulation. The effect of unchanged values in neither the amount of perceived temperature nor latent or sensible heat flux directly above water surface is unclear and depends upon the water-atmosphere coupling of PALM4U. This, at this stage, is an unclear effect too speculative to interpret, given the current knowledge of the PALM model behaviour. The negative values for the latent heat flux above the city area are biophysically meaningful. The sealed surfaces induce very little evaporation, values that are smaller than the spatial mean. Consequently, the warm effects in sensible heat flux of the cityscape must derive from the surplus of buildings and can be neglected. Therefore, the negative deviation of sensible heat flux above the Roter Main can also not be considered as absolute as the mean is shifted to a more positive value, due to a large amount of available building material and sealed surfaces.

For the simulation at 4:30, the perceived temperature has smaller values of 16 °C compared to the perceived temperature at nighttime (cf. Fig. 32a and Fig. 33a). At night, the floodplain around the Wilhelminenaue is + 1 °C warmer than the floodplain surrounding the Roter Main in the northwest (cf. Fig. 33a). The perceived temperature above the water surface at night cannot be distinguished anymore from the perceived temperature above the land surface (cf. Fig. 33a). The difference in perceived temperature between scenario A (4:30) and the base run for (4:30) shows no significant differences for the areas of the Roter Main (cf. Fig. 33d and Fig. 28d). One local effect at the height of the Wilhelminenaue floodplain is visible (cf. Fig. 33d). The spatial distribution of thermal differences shows a negative deviation of -3 °C for the floodplain of the Wilhelminenaue in the northeast and the floodplain of the Mainaue in the northwest (cf. Fig. 33g).

The latent heat flux values at 4:30 in scenario A are in line with the distribution of latent heat flux values in Figure 28c. For the simulation of scenario A, the latent heat flux is largest above stagnant water (cf. Fig. 33b). Latent heat flux values above stagnant water reach 80 Wm^{-2} at night, while, at the same time, they reach 50 Wm^{-2} for bodies of flowing water. The difference between scenario A and base run in Figure 33e) shows a latent heat flux of + 40 Wm^{-2} at the edge of the river bed. In contrast, a negative deviation of approximately - 10 Wm^{-2} is shown on the course of the river (cf. Fig. 33e). The spatial variation of scenario A shows a latent heat flux deviation of + 50 Wm^{-2}

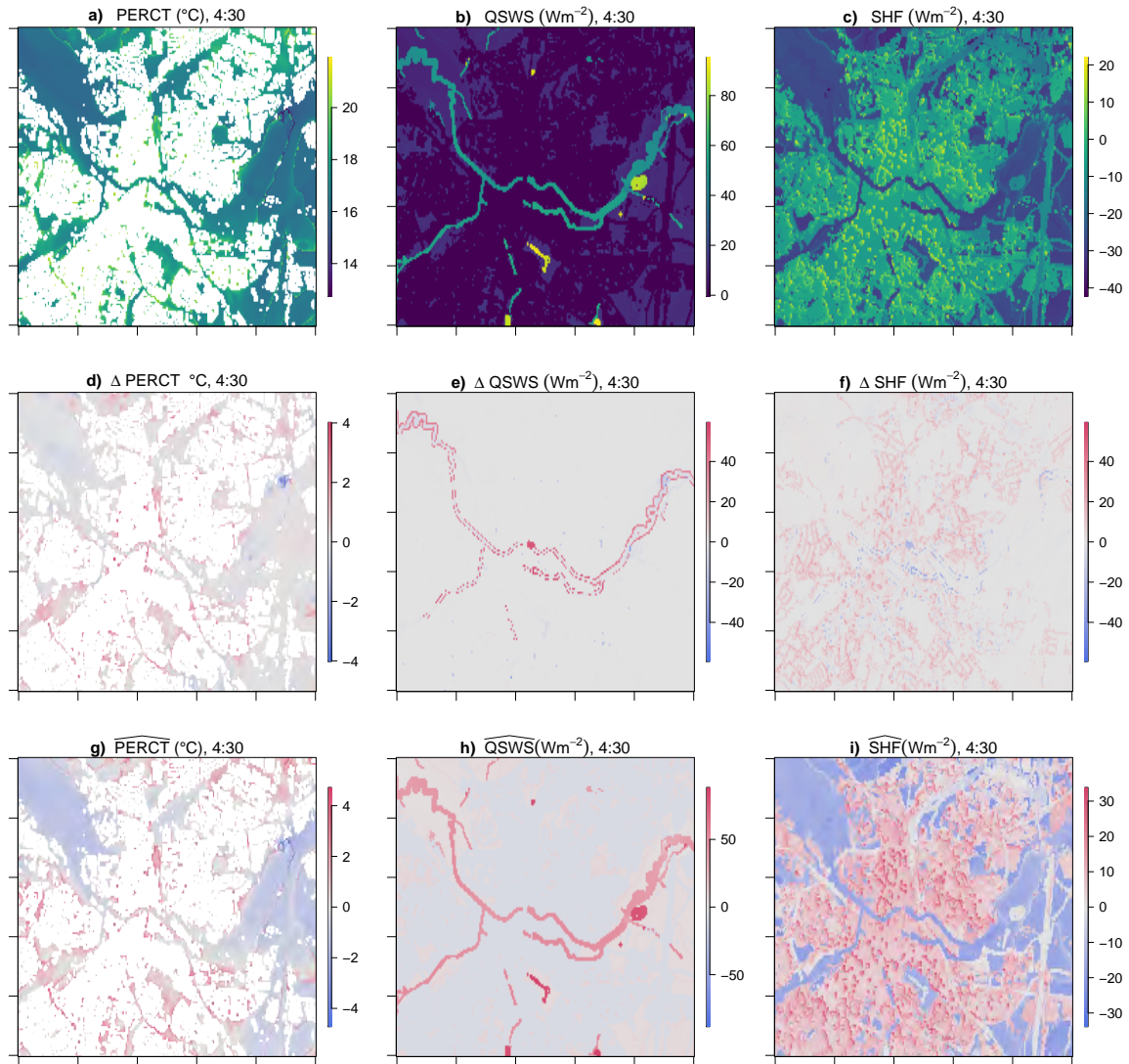


Figure 33: Overview of absolute and difference magnitudes for scenario A at 4:30 CET. For the difference magnitudes d) - f), the base run matrix is subtracted from the scenario matrix. For the difference magnitudes g) - i), the spatial mean is calculated across the depicted cutout. a) perceived temperature in $^{\circ}\text{C}$ for the simulation at 4:30 CET, b) latent heat flux in Wm^{-2} simulated at 4:30 CET, c) sensible heat flux in Wm^{-2} simulated at 4:30 CET, d) Δ perceived temperature in $^{\circ}\text{C}$ for the simulation at 4:30 CET, e) Δ latent heat flux in Wm^{-2} simulated at 4:30 CET, f) Δ sensible heat flux in Wm^{-2} simulated at 4:30 CET, g) $\widehat{\Delta}$ perceived temperature in $^{\circ}\text{C}$ for the simulation at 4:30 CET, h) $\widehat{\Delta}$ latent heat flux in Wm^{-2} simulated at 4:30 CET, i) $\widehat{\Delta}$ sensible heat flux in Wm^{-2} simulated at 4:30 CET. The cutout represents the core of Bayreuth from the entire simulated domain.

above the course of the river (cf. Fig. 33h). The spatial variation of the latent heat flux is negative for the city at night (cf. Fig. 33h). In contrast, the surrounding area of Bayreuth has a small positive deviation, even though the values are close to the spatial

mean (cf. Fig. 33h). The sensible heat flux in scenario A at 4:30 is negative (cf. Fig. 33c). Figure 33f shows the flooded Annecy square as well as the converted pixel of the Roter Main as a negative difference. Figure 33i shows consequently all pixels of water surfaces to be the coldest of the cutout and, together with the residual land surface pixel, these surfaces are significantly colder than the mean value. For the difference of perceived temperature between scenario A and the base run, the warming effects shown in scenario A above the cityscape can be neglected due to the reasons mentioned above. The spatial distribution of the thermal differences at 4:30 demonstrates the establishment of cold air pools covering the area surrounded by the water surfaces. Stagnant water is expected to heat up quicker than floating water at high daytime temperatures. The PALM4U model differentiates water surfaces between river, lake and ponds. However, all bulk table parameters were initially set to the same fixed value of 8 °C water temperature. As first test runs revealed a large underestimation for all water surfaces and latent heat fluxes, this value was increased to 18 °C for flowing water and 20 °C for stagnant water. Therefore, PALM4U does differentiate between stagnant and flowing water for this simulation. The difference in latent heat flux between scenario A and the base run is expected as there is a surplus of $+40 \text{ Wm}^{-2}$ evaporation for those pixels shown that were changed from land surface- to water surface land-use in the scenario. One example in particular is Annecy square (cf. Fig. 33e). Accordingly, this shows that PALM4U simulates the latent heat flux at nighttimes larger above water surfaces than above land surfaces (cf. Fig. 33e). The latent heat flux during the day is smaller above water surfaces than above land surfaces (cf. Fig. 32e). Therefore, evaporation effects above water result in a larger latent heat flux during the night than evapotranspirational effects from vegetated land surfaces, such as grasslands or forests for periods of extreme heat. The results of the sensible heat flux for the simulation of scenario A at 4:30 show that the addition of water surface into the domain would not only increase the amount of surface available for evaporation, but would also lead to the increase of nighttime 'sinks' for air and perceived temperature. For extreme heat periods such as the one depicted in the simulation, the land surface is cooler at night than the air temperature. Consequently, the latent heat flux gets directed towards the surface and thus helps the air and perceived temperature to cool down at night.

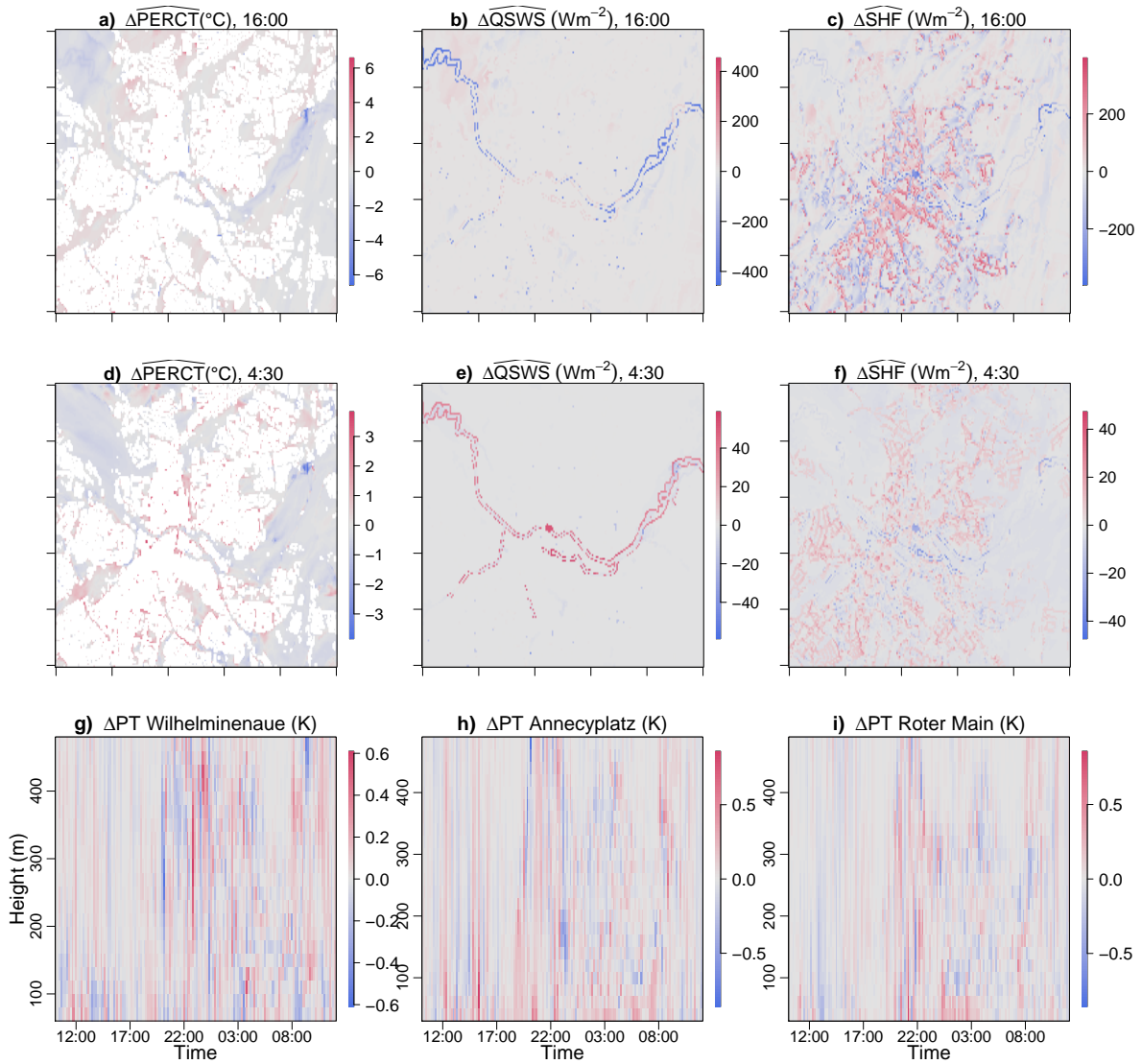


Figure 34: Schematic of the simulated change of magnitudes and their simulated spatial variability for scenario A. a) spatial variability of perceived temperature in °C for 16:00 CET, b) spatial variability of the latent heat flux in Wm^{-2} for 16:00 CET, c) spatial variability of the sensible heat flux in Wm^{-2} for 16:00 CET, d) spatial variability of perceived temperature in °C for 4:30 CET, e) spatial variability of the latent heat flux in Wm^{-2} for 4:30 CET, f) spatial variability of the sensible heat flux in Wm^{-2} for 4:30 CET, g) potential temperature difference of profiles taken at the Wilhelminenaue, h) potential temperature difference of profiles taken at the Annecy Square, i) potential temperature difference of profiles taken at the Roter Main. For the spatial variability magnitudes a) - f), the spatial mean is calculated across the depicted cutout and subtracted from the matrix of scenario A. For the difference magnitudes g) - i), the base run matrix is subtracted from the matrix of scenario A. The profiles were taken above water surface.

The combination of the spatial distribution of the differences between scenario A and base run for the simulations during day- and nighttime in Figure 34 shows the total impact of scenario A. This is based upon the change in latent heat flux and sensible heat flux for the simulation of the scenario compared to the base run. During daytime, the increase in simulated water surfaces leads to less evaporation in scenario A than the simulated evapotranspiration in the base run for the respective land surfaces (cf. Fig. 34b). During nighttime, the increase in simulated water surfaces leads to higher evaporation in scenario A than the simulated evapotranspiration in the base run for the respective land surfaces (cf. Fig. 34e). The increase in simulated water surfaces leads to less transfer of enthalpy above water surfaces in scenario A than in the base run above the respective land surfaces for day- and nighttime.

The application of scenario A shows that the addition of water surfaces leads to the accumulation of cool temperature surfaces during daytime (cf. Fig. 34). Apart from that, the addition of water surfaces has no impact on the increase or mitigation of air or perceived temperature (cf. Fig. 35). For the diurnal cycle of the simulation, no impact on temperature can be detected on the spatial scale. For the nocturnal cycle of the simulation, the addition of water surfaces has a small mitigating impact on the temperature. This nocturnal impact on temperature mitigation does also have an effect on a spatial scale. This spatial scale is not equidistant, but varies in size dependent on the location in the domain. The distribution for this spatial scale and is not uniform throughout the whole domain.

4.3.2. Scenario C

For the overall assessment of the behaviour between scenario C and the base run, scenario C.2 is taken as reference. The simulation at 16:00 of scenario C.2 shows a mean increase in air temperature of $\Delta 0.5$ K compared to the base run (cf. 35). The perceived temperature shows a mean decrease of 0.0 °C with a maximum value of 2.24 °C compared to the base run (cf. Fig. 36). The perceived temperature in scenario C and the perceived temperature of the base run are spatially identical for most parts of the domain (cf. Fig. 36b). The spatial variation of perceived temperature in scenario C.2 (cf. Fig. 36g) has a maximum of 5.0 °C. A sharp transition from the housing area towards the more open space exists (cf. Fig. 36). The latent heat flux has a simulated mean deviation of -91

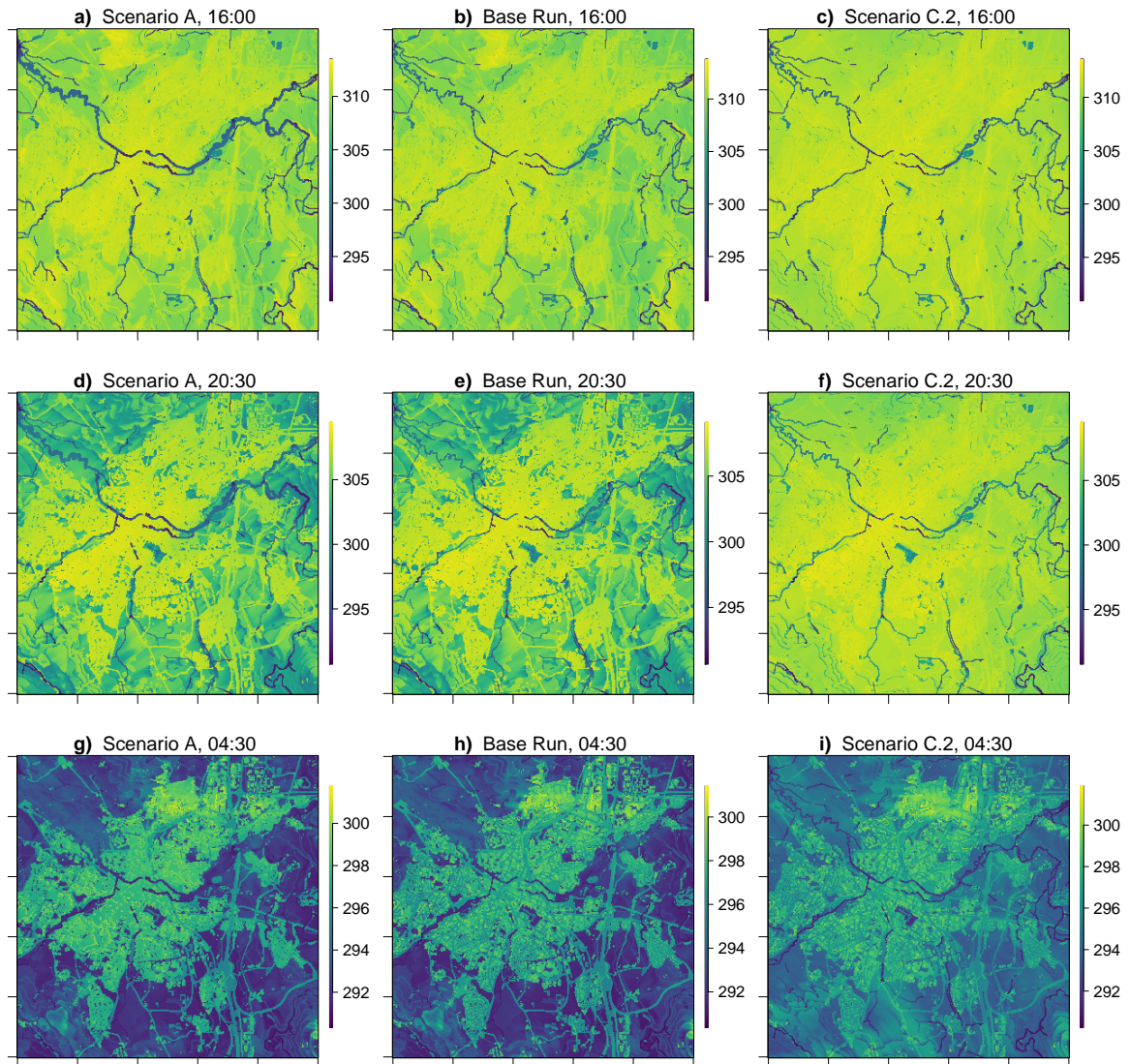


Figure 35: Comparison of simulated air temperature in Kelvin at 16:00, 20:30 and 04:30 CET for the base run and the scenarios. For scenario C, C.2 is taken as reference. The schematic depicts the cutout of the domain of range E-UTM: 682524 - 688024, N-UTM: 5532546 - 5537026 (cf. Fig. 23).

Wm^{-2} between scenario C and the base run. Minimum difference values of the latent heat flux are -377 Wm^{-2} , whereas maximum difference values are 226 Wm^{-2} . The minimum values were found for the land surface types of crops, whereas the differences to short grass shows a higher deviation of -200 Wm^{-2} (cf. Fig. 36e). Maximum values were observed above forest areas. The spatial variation of the latent heat flux shows a clear distribution: the minimum negative deviation is above building and pavement surfaces (70 Wm^{-2}), whereas maximum is above the Hofgarten (381 Wm^{-2}). The sensible heat flux shows an increase in flux values for the converted land surface types (cf. Fig. 28, Fig.

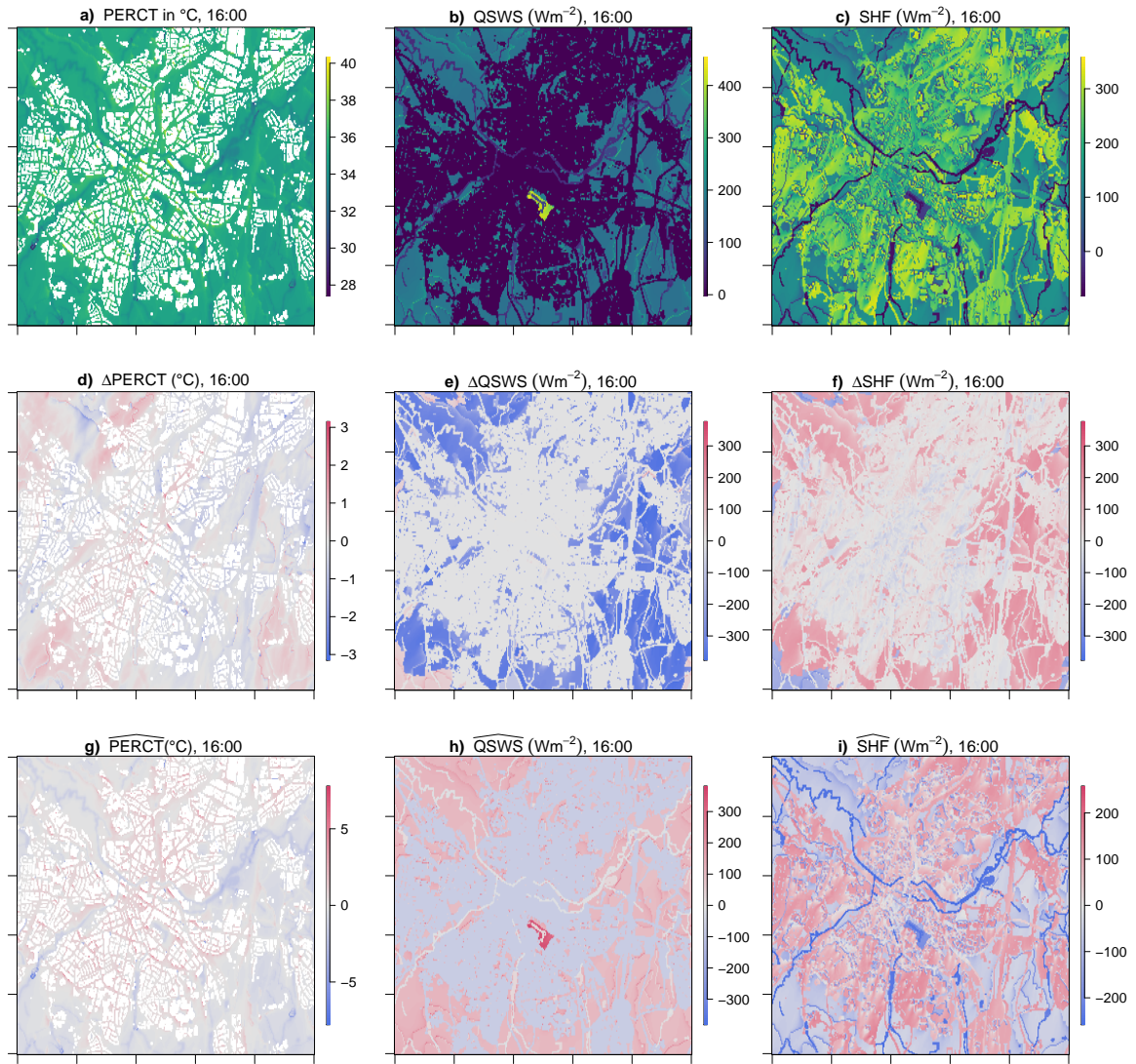


Figure 36: Overview of total and difference magnitudes for scenario C.2. For the difference magnitudes d) - f), the base run matrix is subtracted from the scenario matrix of C.2. For the difference magnitudes g) - i), the spatial mean is calculated across the depicted cutout. a) perceived temperature in $^{\circ}\text{C}$ for the simulation at 16:00 CET, b) latent heat flux in Wm^{-2} simulated at 16:00 CET, c) sensible heat flux in Wm^{-2} simulated at 16:00 CET, d) Δ perceived temperature in $^{\circ}\text{C}$ at 16:00 CET, e) Δ latent heat flux in Wm^{-2} at 16:00 CET, f) Δ sensible heat flux in Wm^{-2} at 16:00 CET, g) Δ perceived temperature in $^{\circ}\text{C}$ at 16:00 CET, h) Δ latent heat flux in Wm^{-2} at 16:00 CET, i) Δ sensible heat flux in Wm^{-2} at 16:00 CET. The cutout represents the map of 21.

36). Figure 36c shows sensible heat flux values for short grass in the Hofgarten and bare soil for the remaining converted land surface pixels by scenario C. The mean increase in sensible heat flux compared to the base run is 41.3 Wm^{-2} . The maximum increase values of $+ 223 \text{ Wm}^{-2}$ are simulated above cropland values. The minimum value between

scenario and base run is -293.0 Wm^{-2} , and is simulated above forest area. Figure 37

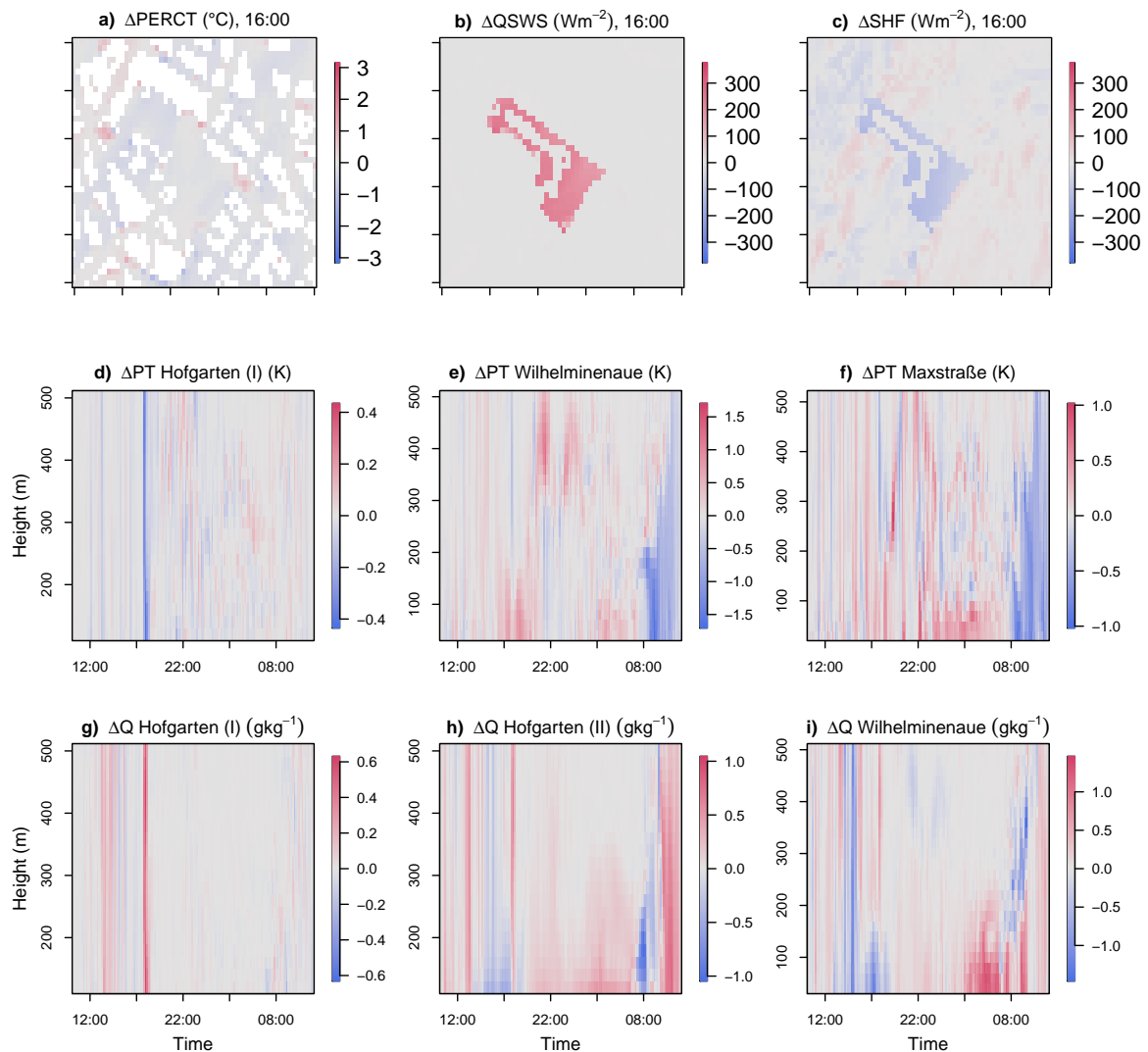


Figure 37: Difference magnitudes for the area and profiles between scenario C.2 and C.1. Scenario C.1 is subtracted from C.2. A) perceived temperature in $^{\circ}\text{C}$ simulated at 16:00 CET, b) latent heat flux in Wm^{-2} simulated at 16:00 CET, c) sensible heat flux in Wm^{-2} simulated at 16:00 CET, d) potential temperature profile in K at the Hofgarten, e) potential temperature profile in K at the Wilhelminenaue, f) potential temperature profile in K at the Maxstraße, g) specific humidity profile in K at the Hofgarten, h) specific humidity profile in K at the Wilhelminenaue, i) specific humidity profile in K at the Maxstraße. The cutout represents the map of 21.

shows the direct comparison between scenario C.2 and C.1. Figure 37a-c is in line with the findings in Figure 36a-f. The difference between the Hofgarten in scenario C.2 and C.1 shows sensible heat flux values of 200 Wm^{-2} .

The insignificant change in perceived temperature in response to the simulated drought

stress (cf. Fig. 36d) is unexpected. The integration of wind, solar and thermal radiation, and humidity might play a crucial role. The simulation period, however, showed extremely dry and windless conditions for the first layer above surface. Thus, factors such as wind and humidity should rather be outweighed by solar and thermal radiation. Back et al. (2021) tested the relation between vegetated space and sealed surfaces on temperature and the universal thermal climate index, as a measure of perceived temperature. They observed surface characteristics to have a strong effect on the values of land surface temperature, mean radiant temperature and the universal thermal climate index. One question that needs to be asked is how well, if at all, the index for PERCT operates on open spaces. The results of Figures 25, 24, 26, 27, show a meaningful biophysical replication of the findings from the MiSKOR observations Lueers and Thomas; Spies; Tschuschke. The spatial variation in Figure 36g shows a clear and reasonable deviation across the cutout of the domain. Information about which feedback processes between the PERCT-index and PALM are taking place is crucial and important. Shading effects, outer wall temperatures, the width of streets, and feedback processes between physical magnitudes and the human body balance are some examples of possible feedback loops taken into consideration for this interconnection of models. Other studies have shown, that urban adaption measures such as the increase in green roofs, urban irrigation, or vegetation have less pronounced cooling effects on human thermal stress than they do on temperature (Li and Norford, 2016; Ma et al., 2018). The spatial variation in Figure 36g) is biophysical meaningful and shows that the core area of Bayreuth is still hotter than the surfaces of the bare soil. There are several factors, already mentioned, which steer the increase of perceived as well as air temperature for the mean of the city area (cf. 4.3.1, 3.6). The grade of sealing and paving material in urban surfaces is relevant for the heating potential (Back et al., 2021). Controlled by absorption, heat storage, and longwave emission, it steers the temperature significantly (cf. Fig. 28h), (Wang et al., 2016). Besides, factors such as urban geometry and the number of vertical surfaces, building density, and the sky view factor have a large impact on the radiational processes and have the potential for heating or cooling effects (Back et al., 2021).

The mechanisms that are most influenced by the change in scenario C are expected to be latent and sensible heat flux (cf. Fig. 36b,c). In his study, Meng (2017) tested a similar simulated scenario of waterlogging during a heatwave period. He found strong

correlation between the water depth and the land surface temperature: during the days when waterlogging occurred, the simulated LST significantly decreased, whereas the days with no waterlogging, the simulated LST showed rapid increase. The results in 4.3.2 are biophysically meaningful. The surfaces above bare soil in scenario C.2 have higher latent heat flux values than above sealed surface areas such as asphalt, concrete, cobblestone, and gravel. Consequently, the values above the bare soil cover deviate from the spatial mean in positive numbers. This is a result of the low amount of permeable surfaces with a capacity for water storage within Bayreuth. With almost no water available for evaporative cooling, the latent heat flux is very low and thus shows negative deviations. The spatial variation of the sensible heat flux shows a distinct pattern (cf. Fig. 36.i): sealed surfaces show a positive deviation from the mean, vegetated and water surfaces show a negative deviation from the mean. Heat transfer can either occur primarily as sensible heat or latent heat. As the transfer of enthalpy, the sensible heat flux is active on surfaces that show no or very little evapotranspiration rates. In contrast to the latent heat flux, the sensible heat flux increases with the change from surfaces with higher roughness length to smoother surfaces with more aerodynamic resistance. For this reason, the Bowen Ratio is a suitable measure to describe that type of heat transfer. The Bowen Ratio for scenario C.1 is 2.58:1, the Bowen Ratio for scenario C.2 is 2.54:1, the Bowen Ratio for the base run is 0.80:1 B6. The Bowen Ratios were computed for the cutout of the domain of scenario C.1/C.2 (cf. Fig. 21). The Bowen Ratios of C.1 and C.2 demonstrate a preponderance of the sensible heat flux towards the latent heat flux. This relation is even more pronounced for Scenario C.1. This behaviour is induced by the application of simulated drought stress.

During nighttime, the mean difference between scenario C.2 and the base run in perceived temperature increases from its initial value of 0.0 °C during daytime to 0.48 °C (cf. Fig. 39a). For air temperature, Figure B14g shows that there is a constant difference between scenario C and the base run. Figure 35d and Figure B14g show an equable difference in air temperature between scenario C and the base run during nighttime. The simulated mean difference in air temperature is 1.03 K for scenario C.2 at 4:30. For perceived temperature, spatial variation is more distinct for the simulation at night (cf. Fig. 38g). Within Bayreuth, strong positive deviations from the mean in perceived temperature are established during nighttime (cf. Fig. 39). The spatial distribution of the latent heat

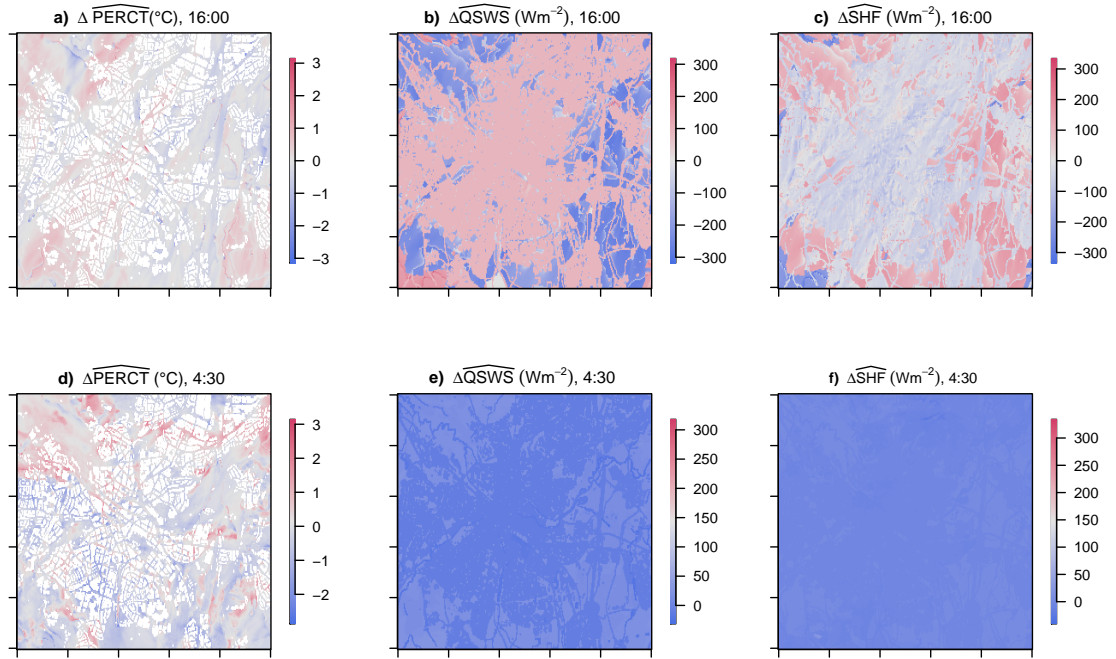


Figure 38: Overview of the spatial distribution of the difference magnitudes for scenario C.2. Scenario C.2 represents all vegetated land surfaces as bare soil, except for the Hofgarten. For the difference magnitudes, the base run matrix is subtracted from the scenario matrix of C.2. The spatial mean is calculated for the difference magnitudes across the depicted cutout. a) perceived temperature in $^{\circ}\text{C}$ for the simulation at 16:00 CET, b) latent heat flux in Wm^{-2} simulated at 16:00 CET, c) sensible heat flux in Wm^{-2} simulated at 16:00 CET, d) perceived temperature in $^{\circ}\text{C}$ at 04:30 CET, e) latent heat flux in Wm^{-2} at 04:30 CET, f) sensible heat flux in Wm^{-2} at 16:00 CET. The cutout represents the map of 21.

flux is very distinct. Negative spatial deviations of -60 Wm^{-2} are observed above the city, whereas the latent heat flux at night is still positive above the bare soil land surface values (cf. Fig. 39). In contrast, the sensible heat flux shows very distinct positive variations for the area where Bayreuth is located (cf. Fig. 39).

During the simulation throughout nighttime hours, the latent heat flux decreased in absolute values and the maximum flux rate shifted from the vegetated land surfaces to the water surface. The sensible heat flux showed positive values for most parts of the city area (cf. Fig. 39c), whereas for surfaces that are not sealed it became directed towards the surface. The Bowen Ratios at night are in line with the small sensible heat flux. However, latent and sensible heat flux become very small at night in comparison to their daytime values. Therefore, the Bowen Ratio for the nighttime may not be biophysically

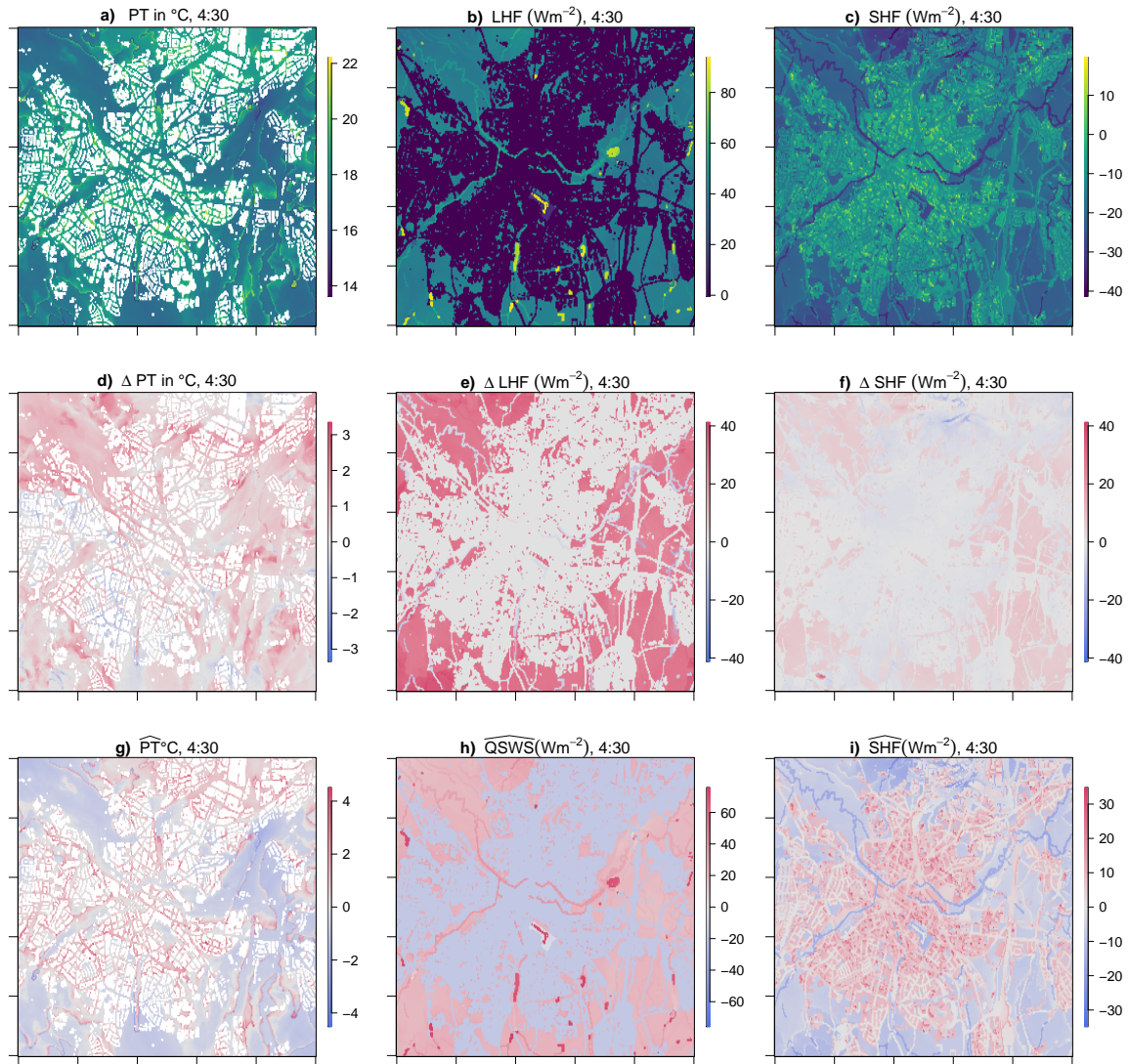


Figure 39: Overview of absolute and difference magnitudes for scenario C.2 at 4:30 CET. For the difference magnitudes d) - f), the base run matrix is subtracted from the scenario matrix of C.2. For the difference magnitudes g) - i), the spatial mean is calculated across the depicted cutout. a) perceived temperature in $^{\circ}\text{C}$, b) absolute latent heat flux in Wm^{-2} , c) absolute sensible heat flux in Wm^{-2} , d) Δ perceived temperature in $^{\circ}\text{C}$, e) Δ latent heat flux in Wm^{-2} , f) Δ sensible heat flux in Wm^{-2} , g) Δ perceived temperature in $^{\circ}\text{C}$, h) Δ latent heat flux in Wm^{-2} , i) Δ sensible heat flux in Wm^{-2} . The cutout represents the map of Figure 21.

meaningful. They were respectively -2.28:1 for the base run, -0.88:1 for scenario C.2, and -1.02:1 for scenario C.1. Consequently, the application of scenario C.1 and C.2 causes stronger effects on air temperature during nighttime. While the difference in air temperature is + 0.5 K for 16:00 in the afternoon, the difference is 1.0 K for the early morning hour at 4:30. The spatial distribution of air temperature for both day- and

nighttime is evenly distributed on the scale of the entire domain.

Strong positive deviations from the mean in perceived temperature are established during nighttime. This finding mainly applies to the core inner-city area (cf. Fig. 38g). The cold air pools centered at the floodplains of Wilhelminaue and Mainaue reach further into the city and show a bigger spatial impact than in Figure 25 for the base run. The deviation between daytime and nighttime differences of scenario C is 0.47 °C. The spatial distribution shows larger spatial spread of the air masses centered at the cold air pools. The lack of vegetated surfaces throughout the city causes larger differences in perceived temperature between the base run and scenario C at night compared to daytime. This finding is in line with the increase in mean air temperature differences between the base run and scenario C for the nighttime.

The application of scenario C shows a spatially even increase in air temperature for the diurnal and nocturnal cycle. The increase in air temperature takes place on the spatial scale of the entire urban area affected by the drought stress. The effect of drought stress on perceived and air temperature increase is larger for the nocturnal cycle than for the diurnal cycle. At the same time, local spatial effects of cold air masses are observed. Cold air pools during drought stress show a bigger spatial impact on the city than for the base run. They cover the spatial extent of streets of houses.

5. Conclusions

In this study, the urban heat effects in a mid-sized city were investigated using an LES model. The motivation of this study was to develop a science-based approach to help cities generate and improve adaptation strategies for heat impacts. The city of Bayreuth was taken as a model for a mid-size European city. In order to evaluate LES model output, a simulation of a past heat wave period was performed. The main intention was to evaluate the biophysical meaningfulness of a control run simulation and apply simple but effective modifications to the cityscape to simulate the effect of city planning measures. A comparative assessment was performed with measurement data from a network of previous studies.

The model approach showed similar magnitudes (max. + 4.8 K vs. max. + 5.1 K) for within city deviations as the measurement network. The control run confirmed the outcome of former studies of the city suffering from a distinct urban heat island effect despite its much smaller size. This effect was observed during daytime and nighttime under dry anticyclonic autochthonous forcing conditions. These findings built the basis for the applications of two scenario simulations. The addition of water inside the city area leads to a surplus of evaporation and to the accumulation of cool temperature surfaces during daytime. For the diurnal cycle, the addition of water has no impact on temperature on a spatial scale. During the nocturnal cycle of the simulation, the addition of water surfaces has a small cooling effect on the temperature. The introduction of drought stress shows a spatially even distributed increase in air temperature at a city-wide scale. This increase is larger for the nocturnal cycle than for the diurnal cycle. A relative change on the impact of cold air pools is observed. For the nocturnal cycle during the drought stress simulation, surrounding cold air pool masses expand to a greater amount into the city and have a cooling effect on the perceived temperature in the city. This effect takes place on the spatial scale of city quarters.

Hypothesis 1 expected PALM4U to show similar urban effects as the observations, taken by the MiSKOR project, have revealed. The control run of the LES model was able to replicate a biophysically meaningful representation for the city of Bayreuth. The bioclimatic output magnitudes agree to a great extent with the general findings from previous studies. However, by far not all investigated effects by previous studies were able to be reproduced, due to the coarser resolution of the model. Hypothesis 1 can be

accepted.

Hypothesis 2 expected an enlargement of the water surfaces of the local river would cool air temperature under anticyclonic weather conditions with small advective forcing at small spatial scale. The spatial impact on air temperature was expected to be larger for the Wilhelminenaue than the inner-city area by the Roter Main. The relative change of absolute temperature was expected to be higher for the inner-city area than the Wilhelminenaue.

The enlargement of water surfaces within the investigation area did not affect a decrease in temperature under the anticyclonic weather condition. The addition of the cool temperature surfaces observed did not lead to a general cooling of air temperature. No clear pattern of a spatial impact was found. The addition of water surfaces had a small mitigating impact on the temperature during nighttime. This impact does show effect on a spatial scale, but no clear pattern was distinguished between Wilhelminenaue and the Roter Main at the height of the inner city area. No relative change of absolute temperature was visible for both locations. Hypothesis 2 is therefore rejected.

Hypothesis 3 could not be investigated. Hypothesis 4 expected drought stress to induce higher air temperatures in city quarters which normally benefit from evapotranspiration from vegetation. Drought stress including the main city park was expected to cause higher Bowen ratios in the inner-city than drought stress simulations excluding the city park. The introduction of drought stress to the city did induce higher air temperatures on the spatial scale of the entire city for air temperature, and on spatial scale of city quarters for perceived temperature. In particular the city quarters next to a floodplain park (Wilhelminenaue) and the city river (Roter Main) were influenced by increased temperatures during nighttime. The Bowen Ratio, for the scenario where drought stress did impact the area of the city park, showed a higher ratio than the one that excluded the city park from drought stress. Hypothesis 3 is therefore accepted.

The results of this thesis show that the LES model approach is capable of reproducing the cityscape of a mid-size city. However, the implementation is very complex and requires a lot of computing power. To give advice to local policy makers or urban management authorities, a fine grid scale is needed in order to observe distinct local effects on the spatial scale of a street of houses. This involves the setup of a grid of 5 m or less which in return, increases the computing power. The access to such computing power is very

limited and thus a big downside for this approach. On the other hand, possibility to study the impact of unknown effects is a great advantage compared to other common approaches of city climate research. It is therefore a very useful tool for researches with access to high performance clusters, to investigate the feedback of urban climatological effects on the city infrastructure.

From the outcome of this thesis, mid-sized European cities shall consider the amount of green space within cities and take account for a regular irrigation if possible. Both urban aspects, the amount and the size of green space can be important to maintain a sustainable urban microclimate. Furthermore, cities should put focus on the adoption of several mitigating strategies and desist from focusing on one spatial and temporal scale.

Acknowledgements

I wish to thank everyone, who supported me very much by contributing to my master thesis. I want to extend special thanks to the ADBV, in particular Stefan Scholz, for providing the georeferenced high resolution data covering Bayreuth and surrounding area, which was used as a baseline for all of my computations. A huge thank you goes to Dr. Wolfgang Babel for permanently guiding and advising me in my work and for his willingness to become acquainted with the PALM model and all supporting software and scripts. Special appreciation must be shown to Julian Zeidler as representative of the DLR who instructed me in the data preparation, provided his scripts and helped me efficiently and regardless of time. I would like to thank the PALM group of Leibnitz University Hannover, especially Prof. Björn Maronga, for providing information and looking into all the issues that came along the way. Special thanks to Prof. Dr. Christoph Thomas, for the advice and mentoring, especially in regards to scientific content, for being supportive and taking time for debate. Furthermore, I am very grateful for contributions from Dr. habil. Johannes Lüers who introduced me to the project and supported me with MiSKOR data. The MiSKOR project, which this thesis is a part of, was supported and funded by the Bayerisches Landesamt für Gesundheit und Lebensmittelsicherheit. Further, I would like to thank the Micrometeorology group, especially Dr. Shравan Muppa, for feedback. My final thanks are offered to Dr. Bernhard Winkler whose time I used extensively for installing the PALM model at the high performance Cluster btrxz3-1.rz at the University of Bayreuth, overseeing the cluster and spending much time on feedback during implementation of the PALM model runs. Thanks to all who have supported me directly and indirectly and whose names are not mentioned here.

References

- Armson, D., P. Stringer, and A. R. Ennos (2013). The effect of street trees and amenity grass on urban surface water runoff in Manchester, UK. *Urban Forestry & Urban Greening*, 12:3, 282–286.
- Back, Yannick et al. (2021). A rapid fine-scale approach to modelling urban bioclimatic conditions. *Science of The Total Environment*, 756: 17.
- Baklanov, Alexander et al. (Mar. 2009). Meteorological and air quality models for urban areas.
- Banta, R. M. et al. (Nov. 2002). Nocturnal Low-Level Jet Characteristics Over Kansas During Cases-99. *Boundary-Layer Meteorology*, 105:2, 221–252.
- Bernard, Jérémy et al. (2017). Urban heat island temporal and spatial variations: Empirical modeling from geographical and meteorological data. *Building and Environment*, 125: 423–438.
- Buchin, Oliver et al. (2016). Evaluation of the health-risk reduction potential of countermeasures to urban heat islands. *Energy and Buildings*, 114: SI: Countermeasures to Urban Heat Island, 27–37.
- Cardoso, Renata Dos Santos et al. (2017). Assessment of Urban Heat Islands in Small- and Mid-Sized Cities in Brazil. *Climate*, 5:1.
- Chandler, T. J. (1962). London's Urban Climate. *The Geographical Journal*, 128:3, 279–298.
- Chandler, T. J. (1964). City growth and urban climates. *Weather*, 19 (6), 170–171.
- Chandler, Tony J. (Aug. 1967). absolute and relative humidities in towns. *Bulletin of the American Meteorological Society*, 48:6, 394–399.
- Clarke, John F. (1972). Some effects of the urban structure on heat mortality. *Environmental Research*, 5:1, 93–104.
- Coates, Lucinda et al. (2014). Exploring 167 years of vulnerability: An examination of extreme heat events in Australia 1844–2010. *Environmental Science & Policy*, 42: 33–44.
- Deardorff, James W. (June 1980). Stratocumulus-capped mixed layers derived from a three-dimensional model. *Boundary-Layer Meteorology*, 18:4, 495–527.
- Debbage, N. and J. M. Shepherd (2015). The urban heat island effect and city contiguity. *Computers, Environment and Urban Systems*, 54: 181–194.

- Delage, Yves and P. A. Taylor (Nov. 1970). Numerical studies of heat island circulations. *Boundary-Layer Meteorology*, 1:2, 201–226.
- Dupuis, D. J. and L. Trapin (Oct. 2020). Structural change to the persistence of the urban heat island. *Environmental Research Letters*, 15:10.
- DWD (Aug. 2, 2019). Großwetterlage. Juni 2019. Tech. rep. Deutscher Wetterdienst, pp. 1–11.
- Edmondson, J. L. et al. (Sept. 2016). Soil surface temperatures reveal moderation of the urban heat island effect by trees and shrubs. *Scientific Reports*, 6: 33708.
- Fanger, P.O. (1970). *Thermal Comfort: Analysis and Applications in Environmental Engineering*. Danish Technical Press.
- Feinberg, Alec (Dec. 2020). Urban heat island amplification estimates on global warming using an albedo model. *SN Applied Sciences*, 2:12, 21.
- Foken, Thomas (2017). *Micrometeorology*. 2nd ed. Springer-Verlag, Berlin, Heidelberg. 362 pp.
- Galmarini, Stefano, jeff vinuesa jeff, and Alberto Martilli (May 2009). Relating Small-Scale Emission and Concentration Variability in Air Quality Models. *Meteorological and Air Quality Models for Urban Areas*, 11–19.
- García-Herrera, Ricardo et al. (Mar. 2010). A Review of the European Summer Heat Wave of 2003. *Critical Reviews in Environmental Science and Technology*, 40: 267–306.
- Gardes, Thomas et al. (2020). Statistical prediction of the nocturnal urban heat island intensity based on urban morphology and geographical factors - An investigation based on numerical model results for a large ensemble of French cities. *Science of The Total Environment*, 737: 139253.
- Gonçalves, Artur et al. (2018). Urban Cold and Heat Island in the City of Bragança (Portugal). *Climate*, 6:3.
- Grimmond, C. S. B. and T. R. Oke (July 2002). Turbulent Heat Fluxes in Urban Areas: Observations and a Local-Scale Urban Meteorological Parameterization Scheme (LUMPS). *Journal of Applied Meteorology*, 41:7, 792–810.
- Harman, I. N. and S. E. Belcher (2006). The surface energy balance and boundary layer over urban street canyons. *Quarterly Journal of the Royal Meteorological Society*, 132:621, 2749–2768.

- Hayhoe, Katharine et al. (2010). Climate change, heat waves, and mortality projections for Chicago. *Journal of Great Lakes Research*, 36: Potential Climate Impacts on Chicago and Midwest, 65–73.
- Hebbert, Michael and Vladimir Jankovic (May 2013). Cities and Climate Change: The Precedents and Why They Matter. *Urban Studies*, 50:7, 1332–1347.
- Hoeppe, P. (Oct. 1999). The physiological equivalent temperature - a universal index for the biometeorological assessment of the thermal environment. *International Journal of Biometeorology*, 43:2, 71–75.
- Hu, Leiqiu and Nathaniel A. Brunsell (2013). The impact of temporal aggregation of land surface temperature data for surface urban heat island (SUHI) monitoring. *Remote Sensing of Environment*, 134: 162–174.
- Juruš, P. et al. (2016). High resolution modelling of anthropogenic heat from traffic in urban canopy: A sensitivity study. 2016 Smart Cities Symposium Prague (SCSP), pp. 1–6.
- LaNasa, Paul J. and E. Loy Upp (2014). 2 - Basic Flow Measurement Laws. *Fluid Flow Measurement (Third Edition)*. Ed. by Paul J. LaNasa and E. Loy Upp. Third Edition. Oxford: Butterworth-Heinemann, 19–29.
- Landsberg, H. E. (1981). *The Urban Climate*. International Geophysics. Elsevier Science.
- Letzel, Marcus Oliver, Martina Krane, and Siegfried Raasch (2008). High resolution urban large-eddy simulation studies from street canyon to neighbourhood scale. *Atmospheric Environment*, 42:38, 8770–8784.
- LfStat (2019). Bayerisches Landesamt für Statistik, Genesis-Online Datenbank. URL: <https://www.statistikdaten.bayern.de>.
- Li, Qi and Zhi-Hua Wang (2018). Large-eddy simulation of the impact of urban trees on momentum and heat fluxes. *Agricultural and Forest Meteorology*, 255: Honoring W.J. Massman's Discoveries: Bringing Physics to Agriculture, 44–56.
- Li, Xian-Xiang and Leslie K. Norford (2016). Evaluation of cool roof and vegetations in mitigating urban heat island in a tropical city, Singapore. *Urban Climate*, 16: 59–74.
- Liu, Nairui and Lidia Morawska (Aug. 2020). Modeling the urban heat island mitigation effect of cool coatings in realistic urban morphology. English. *Journal of cleaner Production*, 264:121560.

- Lueers, Johannes and Christoph Thomas (Mar. 15, 2021). Minderung städtischer Klima- und Ozonrisiken: Final Report. Mikrometeorologie, Universität Bayreuth.
- Ma, Shaoxiu et al. (2018). Evaluating the Effectiveness of Mitigation Options on Heat Stress for Sydney, Australia. *Journal of Applied Meteorology and Climatology*, 57:2, 209–220.
- Majazi, Nobuhle P. et al. (2021). Uncertainty and Sensitivity Analysis of a Remote-Sensing-Based Penman–Monteith Model to Meteorological and Land Surface Input Variables. *Remote Sensing*, 13:5.
- Makido, Y., D. Hellman, and V. Shandas (2019). Nature-Based Designs to Mitigate Urban Heat: The Efficacy of Green Infrastructure Treatments in Portland, Oregon. *Atmosphere*, 10:5.
- Makido, Yasuyo et al. (2016). Daytime Variation of Urban Heat Islands: The Case Study of Doha, Qatar. *Climate*, 4:2.
- Maronga, B. et al. (2015). The Parallelized Large-Eddy Simulation Model (PALM) version 4.0 for atmospheric and oceanic flows: model formulation, recent developments, and future perspectives. *Geoscientific Model Development*, 8:8, 2515–2551.
- Maronga, Bjoern et al. (June 2019). Development of a new urban climate model based on the model PALM ? Project overview, planned work, and first achievements. *Meteorologische Zeitschrift*, 28:2, 105–119.
- Martilli, Alberto (2007). Current research and future challenges in urban mesoscale modelling. *International Journal of Climatology*, 27:14, 1909–1918.
- Martilli, Alberto and Jose Santiago (May 2009). How to Use Computational Fluid Dynamics Models for Urban Canopy Parameterizations, pp. 31–37.
- Mehrotra, S., R. Bardhan, and K. Ramamritham (2019). Outdoor thermal performance of heterogeneous urban environment: An indicator-based approach for climate-sensitive planning. *Science of The Total Environment*, 669: 872–886.
- Memon, Rizwan Ahmed, Dennis Y. C. Leung, and Chun-Ho Liu (2009). An investigation of urban heat island intensity (UHII) as an indicator of urban heating. *Atmospheric Research*, 94:3, 491–500.
- Meng, Chunlei (Aug. 2017). Mitigating the surface urban heat island: Mechanism study and sensitivity analysis. *Asia-Pacific Journal of Atmospheric Sciences*, 53:3, 327–338.

- Mikrometeorologie, University Bayreuth (Apr. 2, 2021). Klimagrafiken der Messungen des Botanischen Gartens. URL: http://www.bayceer.uni-bayreuth.de/meteo/Klimagrafiken/BotG/BotG_2019_barplot_monthlyTA_vio_de.png.
- Mills, Gerald (June 2008). Luke Howard and The Climate of London. *Weather*, 63: 153–157.
- Mills, Gerald (2014). Urban climatology: History, status and prospects. *Urban Climate*, 10: Measurement and modelling of the urban atmosphere in the present and the past, 479–489.
- Mokhtarpoor, Reza and Stefan Heinz (2017). Dynamic large eddy simulation: Stability via realizability. *Physics of Fluids*, 29:10, 105104.
- Monin, Andrei Sergeevich and Alexander Mikhailevich Obukhov (1954). Osnovnye zakonomernosti turbulentnogo peremesivaniya v prizemnom sloe atmosfery. (Basic laws of turbulent mixing in the atmosphere near the ground). *Trudy geofiz inst*, 24: (151), 163–187.
- Mukherjee, Sourav and Ashok Kumar Mishra (2021). Increase in Compound Drought and Heatwaves in a Warming World. *Geophysical Research Letters*, 48:1. e2020GL090617 2020GL090617, 13.
- Nazarian, Negin, E. Scott Krayenhoff, and Alberto Martilli (Mar. 2020). A one-dimensional model of turbulent flow through urban canopies: updates based on large-eddy simulation. English. *Geoscientific model development*, 13:3, 937–953.
- Oke, T. R. (1982). The energetic basis of the urban heat island. *Quarterly Journal of the Royal Meteorological Society*, 108:455, 1–24.
- Oke, T. R. and H. A. Cleugh (May 1987). Urban heat storage derived as energy balance residuals. *Boundary-Layer Meteorology*, 39:3, 233–245.
- Ossenbruegge, J. and B. Bechtel (2010). Klimawandel und Stadt: Der Faktor Klima als neue Determinante der Stadtentwicklung. *Hamburger Symposium Geographie*.
- Parsons, K. (2002). *Human Thermal Environments*. Ed. by Boca Raton. CRC Press.
- Peng, S. et al. (Jan. 2012). Surface Urban Heat Island Across 419 Global Big Cities. *Environmental Science & Technology*, 46:2, 696–703.
- Raasch, Siegfried and Michael Schroeter (Oct. 2001). PALM - A large-eddy simulation model performing on massively parallel computers. *Meteorologische Zeitschrift*, 10:5, 363–372.

- Rehm, Bill et al. (2008). Chapter Two - Situational Problems in MPD. Managed Pressure Drilling. Ed. by Bill Rehm et al. Gulf Publishing Company, 39–80.
- Rizwan, Ahmed Memon, Leung Y. C. Dennis, and Chunho Liu (2008). A review on the generation, determination and mitigation of Urban Heat Island. *Journal of Environmental Sciences*, 20:1, 120–128.
- Rötzer, T. et al. (2019). Process based simulation of tree growth and ecosystem services of urban trees under present and future climate conditions. *Science of The Total Environment*, 676: 651–664.
- Schumann, U. (1975). Subgrid scale model for finite difference simulations of turbulent flows in plane channels and annuli. *Journal of Computational Physics*, 18:4, 376–404.
- Shem, W. and M. Shepherd (2009). On the impact of urbanization on summertime thunderstorms in Atlanta: Two numerical model case studies. *Atmospheric Research*, 92:2, 172–189.
- Sima, Mihaela et al. (2016). Climate Change Projections for a Medium-Size Urban Area (Baia Mare Town, Romania): Local Awareness and Adaptation Constraints. English. Implementing climate change adaptation in cities and communities: Integrating strategies and educational approaches. Ed. by W. L. Filho et al. *Climate Change Management*. Springer Int Publishing AG., pp. 277–301.
- Smagorinsky, J. (Mar. 1963). general circulation experiments with the primitive equations: I. the basic experiment. *Monthly Weather Review*, 91:3, 99–164.
- Spies, Isabel (2019). Urban climate - just warm streets and cool parks? Investigating the variabilities of heat at street-canyon and city-wide scale in Bayreuth. MA thesis. University of Bayreuth - Micrometeorology, 79. 94 pp.
- Staiger, H., K. Bucher, and G. Jendritzky (1997). Gefühlte Temperatur. Die physiologisch gerechte Bewertung von Wärmebelastung und Kältestress beim Aufenthalt im Freien in der Maßzahl Grad Celsius. *Annalen der Meteorologie*, 33: 100–107.
- Staiger, Henning, Gudrun Laschewski, and Angelika Grätz (Jan. 2012). The perceived temperature - a versatile index for the assessment of the human thermal environment. Part A: scientific basics. *International Journal of Biometeorology*, 56:1, 165–176.
- Stewart, Mark G., Xiaoming Wang, and Minh N. Nguyen (2011). Climate change impact and risks of concrete infrastructure deterioration. *Engineering Structures*, 33:4, 1326–1337.

- Tschuschke, Andreas (2019). Einfluss von Topografie, Fließgewässern und Bebauung auf Temperaturverteilung und Luftströme im Bayreuther Becken. Analyse von fahrradgetragenen Temperaturmessungen und Stationsdaten des MiSKOR-Messnetzes im Sommer 2019. Bachelorarbeit. Mikrometeorologie Gruppe, Universität Bayreuth, 116.
- UN (2018). World urbanization prospects: The 2018 revision. United Nations Department of Economic and Social Affairs, Population Division. 126 pp.
- Veena, K., K. M. Parammasivam, and T. N. Venkatesh (Mar. 2020). Urban Heat Island studies: Current status in India and a comparison with the International studies. *Journal of Earth System Science*, 129:1, 85.
- Wang, Chuyuan et al. (2016). Empirical modeling and spatio-temporal patterns of urban evapotranspiration for the Phoenix metropolitan area, Arizona. *GIScience & Remote Sensing*, 53:6, 778–792.
- Wong, Nyuk Hien et al. (2021). An integrated multiscale urban microclimate model for the urban thermal environment. *Urban Climate*, 35: 100730.
- Xie, Zheng-Tong and Ian P. Castro (Oct. 2008). Efficient Generation of Inflow Conditions for Large Eddy Simulation of Street-Scale Flows. *Flow, Turbulence and Combustion*, 81:3, 449–470.
- Xie, Zheng-Tong and Ian P. Castro (2009). Large-eddy simulation for flow and dispersion in urban streets. *Atmospheric Environment*, 43:13, 2174–2185.
- Xie, Zhenqiong and Ian P. Castro (Aug. 2006). LES and RANS for Turbulent Flow over Arrays of Wall-Mounted Obstacles. *Flow, Turbulence and Combustion*, 76:3, 291.
- Yang, Zhiyin (Dec. 2014). Large-eddy simulation: Past, present and the future. *Chinese Journal of Aeronautics*, 91: 11–24.
- Zak, Michal et al. (2020). Influence of synoptic scale atmospheric circulation on the development of urban heat island in Prague and Bucharest. *Urban Climate*, 34:100681.
- Zhu, Xiaoliang et al. (2017). An idealized LES study of urban modification of moist convection. *Quarterly Journal of the Royal Meteorological Society*, 143:709, 3228–3243.
- Zscheischler, Jakob and Erich M. Fischer (Sept. 2020). The record-breaking compound hot and dry 2018 growing season in Germany. English. *Weather and Climate Extremes*, 29:100270.

Appendices

A. PALM4U Model Description

Table A1: Resampling method

class type	resampling method
building height	average
building ID	mode
building type	mode
pavement type	mode
topography	average
vegetation type	mode
water type	mode

Table A2: Alignment of Landuse-Layers

statpid root domain	statpid nesting	scenario Roter Main
soil Layer	soil Layer	soil Layer
vegetation Layer	vegetation Layer	vegetation Layer
water	water Layer	building Layer
building	pavement Layer	pavement Layer
pavement type	building Layer	water Layer

Table A5: List of parameter stored in the dynamic driver

Parameter	Dimensions
initial soil temperature	x, y, zsoil
initial soil moisture	x, y, zsoil
initial potential temperature	z
large-scale forcing for left model boundary for the potential temperature	y, z, time
large-scale forcing for right model boundary for the potential temperature	y, z, time

large-scale forcing for north model boundary for the potential temperature	x, z, time
large-scale forcing for south model boundary for the potential temperature	x, z, time
large-scale forcing for top model boundary for the potential temperature	x, y, time
initial specific humidity	z
large-scale forcing for left model boundary for the specific humidity	y, z, time
large-scale forcing for right model boundary for the specific humidity	y, z, time
large-scale forcing for north model boundary for the specific humidity	x, z, time
large-scale forcing for south model boundary for the specific humidity	x ,z, time
large-scale forcing for top model boundary for the specific humidity	x, y, time
surface pressure	time
geostrophic wind, u component, v component	z, time
initial wind component in x direction	z
large-scale forcing for left model boundary for the wind component in x direction	y, z, time
large-scale forcing for right model boundary for the wind component in x direction	y, z, time
large-scale forcing for north model boundary for the wind component in x direction	xu, z, time
large-scale forcing for south model boundary for the wind component in x direction	xu, z, time
large-scale forcing for top model boundary for the wind component in x direction	xu, z, time
initial wind component in y direction	z

large-scale forcing for left model boundary for the wind component in y direction	yv, z, time
large-scale forcing for right model boundary for the wind component in y direction	yv, z, time
large-scale forcing for north model boundary for the wind component in y direction	x,z,time
large-scale forcing for south model boundary for the wind component in y direction	x,z,time
large-scale forcing for top model boundary for the wind component in y direction	x,yv,time
initial wind component in z direction	zw
large-scale forcing for left model boundary for the wind component in z direction	y,zw,time
large-scale forcing for right model boundary for the wind component in z direction	y,zw,time
large-scale forcing for north model boundary for the wind component in z direction	x,zw,time
large-scale forcing for south model boundary for the wind component in z direction	x,zw,time
large-scale forcing for top model boundary for the wind component in z direction	x,y,time
initial cloud water mixture fraction	z
large-scale forcing for left model boundary for the cloud water mixture fraction	y,z,time
large-scale forcing for right model boundary for the cloud water mixture fraction	y,z,time
large-scale forcing for north model boundary for the cloud water mixture fraction	x,z,time
large-scale forcing for south model boundary for the cloud water mixture fraction	x,z,time
large-scale forcing for top model boundary for the cloud water mixture fraction	x,z,time

Incoming shortwave radiation from the Ecoogical botanical Garden, interpolated from 10min observations	time
Incoming longwave radiation from the Ecoogical botanical Garden, interpolated from 10min observations	time

Table A3: List of minimum required COSMO-D2 parameter to initiate the dynamic driver

COSMO model output	variables
COSMO numerical grid	Longitude in rotated pole grid
COSMO numerical grid	Latitude in rotated pole grid
COSMO numerical grid	Geometric height of layer above NN
COSMO soil map	Soil type of grid
COSMO atmospheric fields	Vertical Velocity
COSMO atmospheric fields	U-Component of Wind
COSMO atmospheric fields	V-Component of Wind
COSMO atmospheric fields	Temperature
COSMO atmospheric fields	Pressure
COSMO atmospheric fields	Specific Humidity
COSMO soil moisture and temperature	Depth below land
COSMO soil moisture and temperature	Soil Temperature
COSMO soil moisture and temperature	Column-integrated Soil Moisture

Table A4: List of PALM4U classification

pavement	code	vegetation	code	water	code
asphalt	2	bare soil	1	river	2
concrete	3	crops	2	lake	1
paving stones	5	short grass evergreen	3	pond	4
cobblestone	6	needleleaf trees deciduous	4		
gravel	9	needleleaf trees evergreen	5		
fine gravel	10	broadleaf trees deciduous	6		
pebblestone	11	broadleaf trees	7		
tartan (sports)	13	deciduous shrubs	16		
		mixed forest	17		

B. Additional Figures and Tables

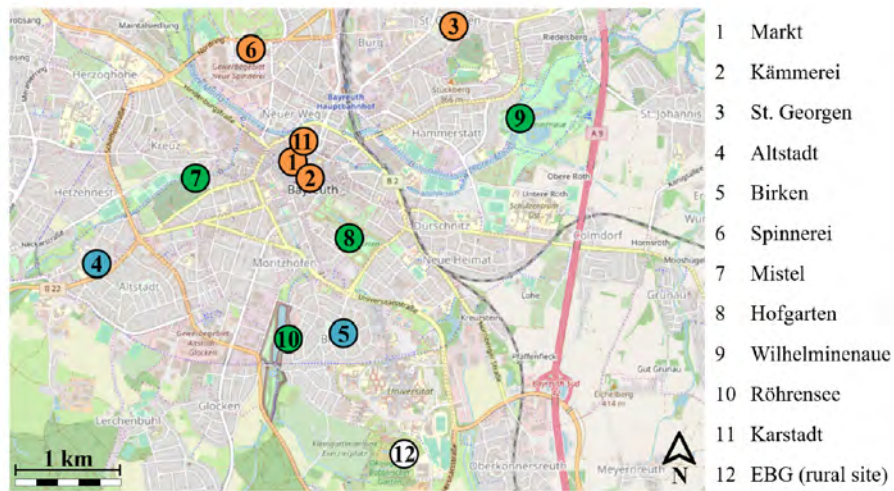


Figure B2: Schematic after (Spies, 2019): Locations of the permanent meteorological measurements in Bayreuth. Highly sealed sites (orange): 1 Markt, 2 Kaemmereigasse, 3 St. Georgen, 6 Spinnerei, and 11 Karstadt; Vegetated sites (green): 7 Mistel, 8 Hofgarten, 9 Wilhelminenaue, and 10 Roehensee; Housing areas (blue): 4 Altstadt and 5 Birken; Rural reference site: 12 EBG (map: OpenStreetMap)

Table B6: Computed Bowen Ratios for C.1, C.2 and the base run

Scenario C.1	Scenario C.2	Base run
2.584:1	2.544:1	0.8:1
-1.02:1	-0.88:1	-2.28:1

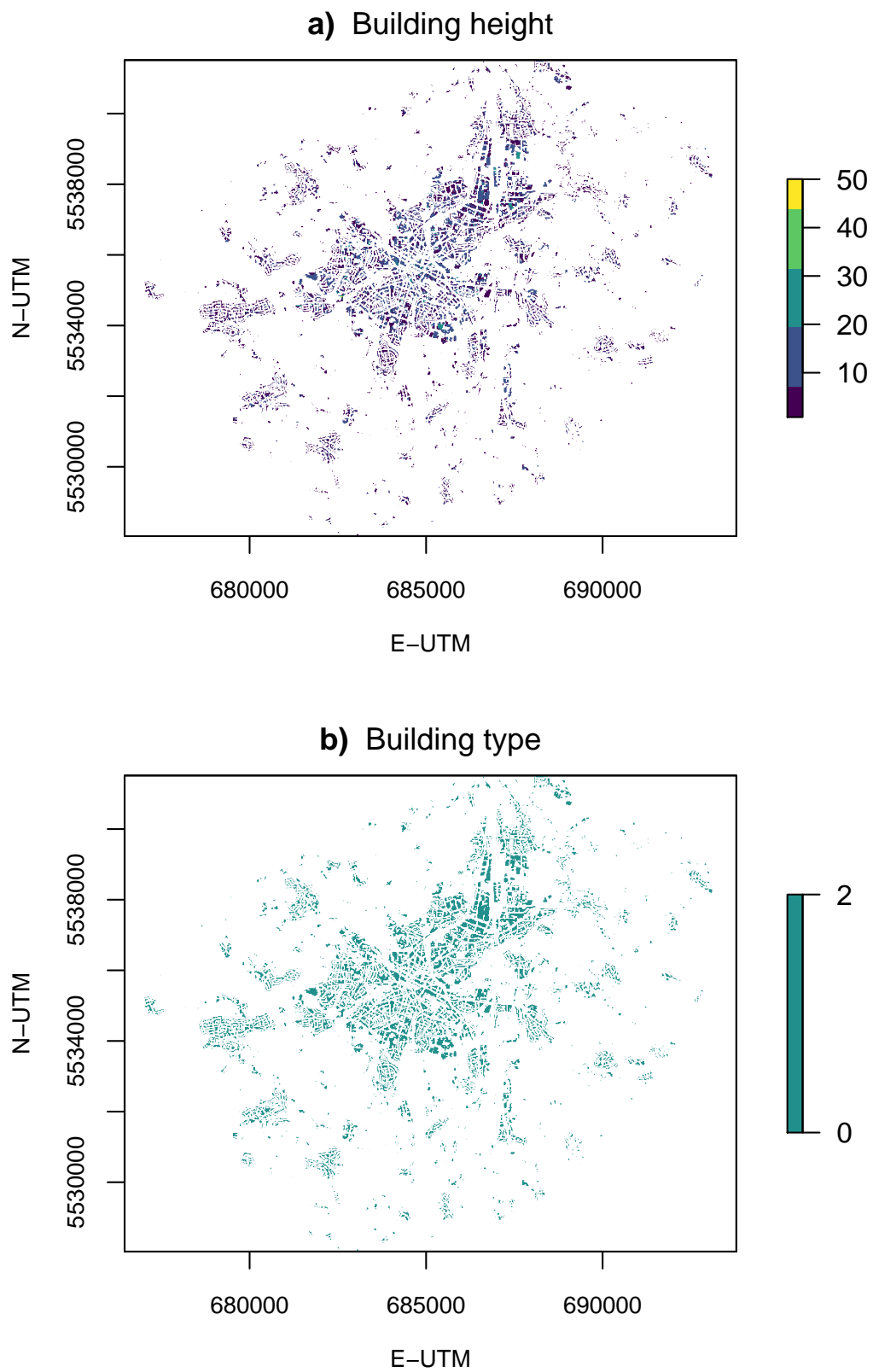


Figure B3: Map of Detail for a) the static driver-building height, b) the static driver-building type. The building height stores information of the LoD2 data, building type is a necessary information to steer the urban surfac module. Building type stores information about the age of the buildings.

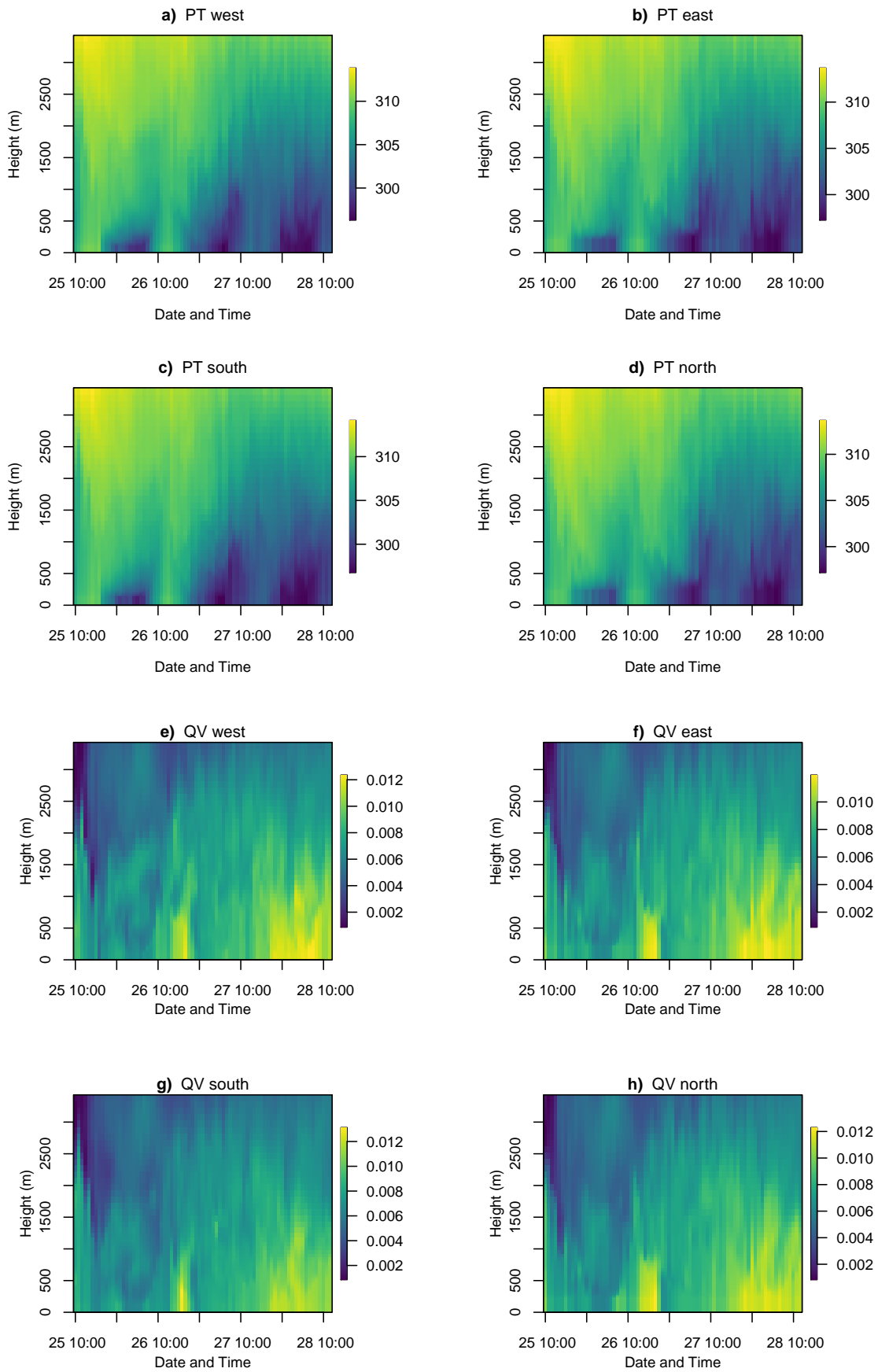


Figure B4: Profile of specific humidity at one random exemplary location of each side of the model domain. The profiles show a more distinct form of the UBL than in Fig.15.

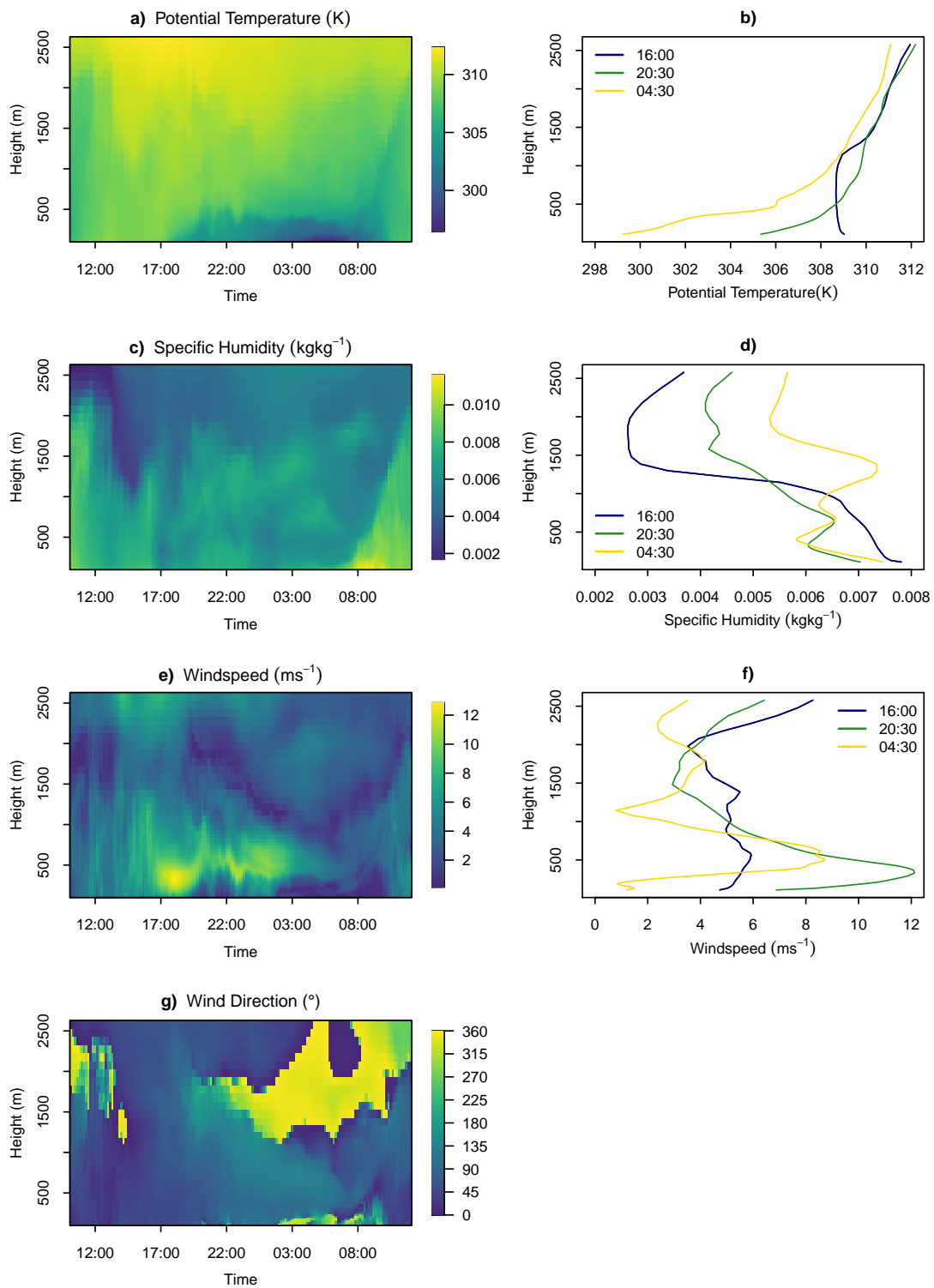


Figure B5: Simulated time height cross section of the very east of Bayreuth. The profile was computed above a cropland surface. The time period shows the 26-hour interval of 07.25.2019 from 10:00 CET to 07.26.2019 12:00 CET. The height is referenced to 0 NN from the lowest point of the domain, the profile data starts at the respective height of the profile location. a), b) potential temperature in Kelvin, c), d) specific humidity in kgkg^{-1} , e), f) windspeed in ms^{-1} , g) wind direction in degree

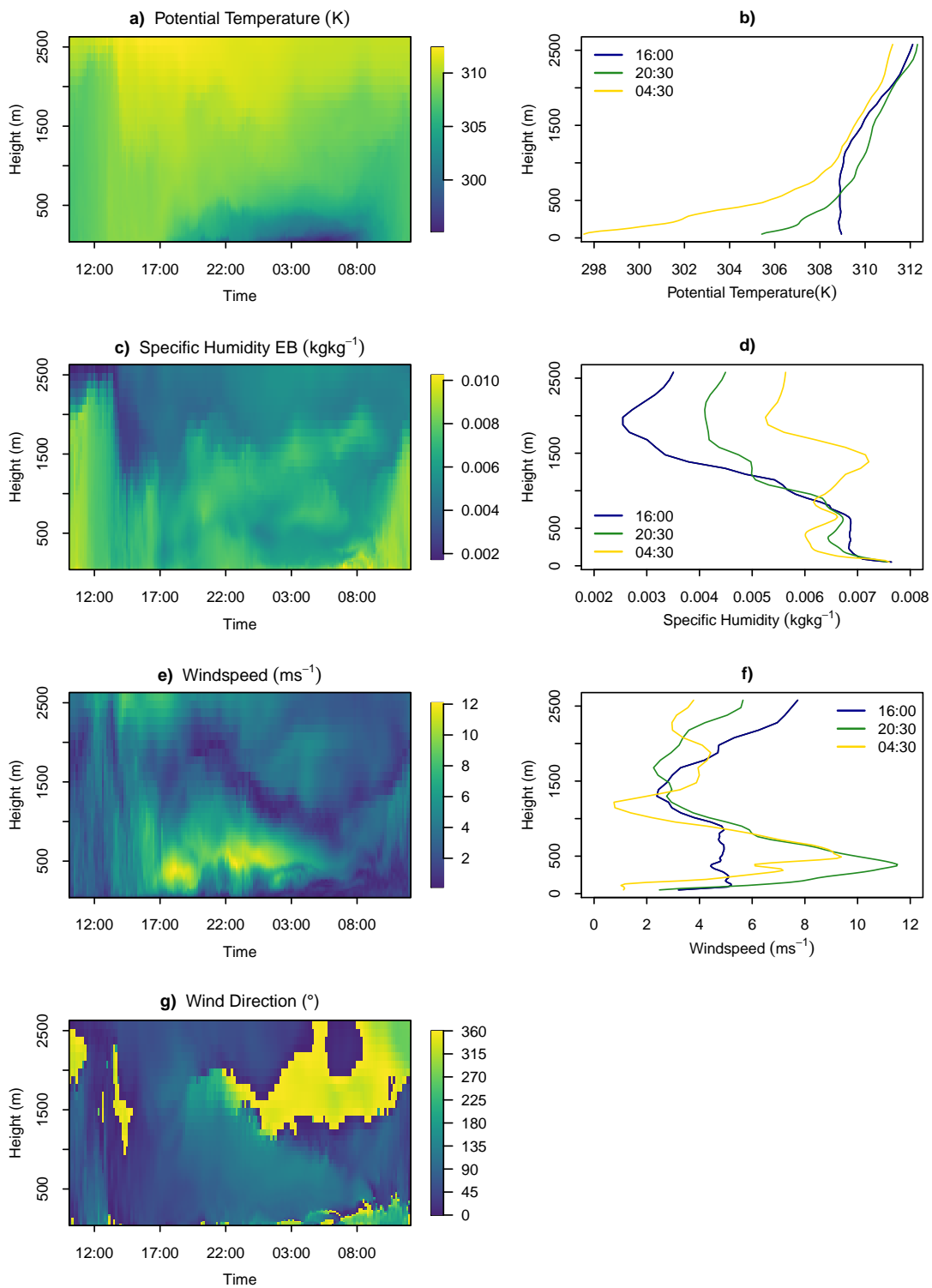


Figure B6: Simulated time height cross section of Bayreuth- Eichelberg. The profile was computed above a homogenous grassland surface. The time period shows the 26-hour interval of 07.25.2019 from 10:00 CET to 07.26.2019 12:00 CET. The height is referenced to 0 NN from the lowest point of the domain, the profile data starts at the respective height of the profile location. a), b) potential temperature in Kelvin, c), d) specific humidity in kgkg^{-1} , e), f) windspeed in ms^{-1} , g) wind direction in degree

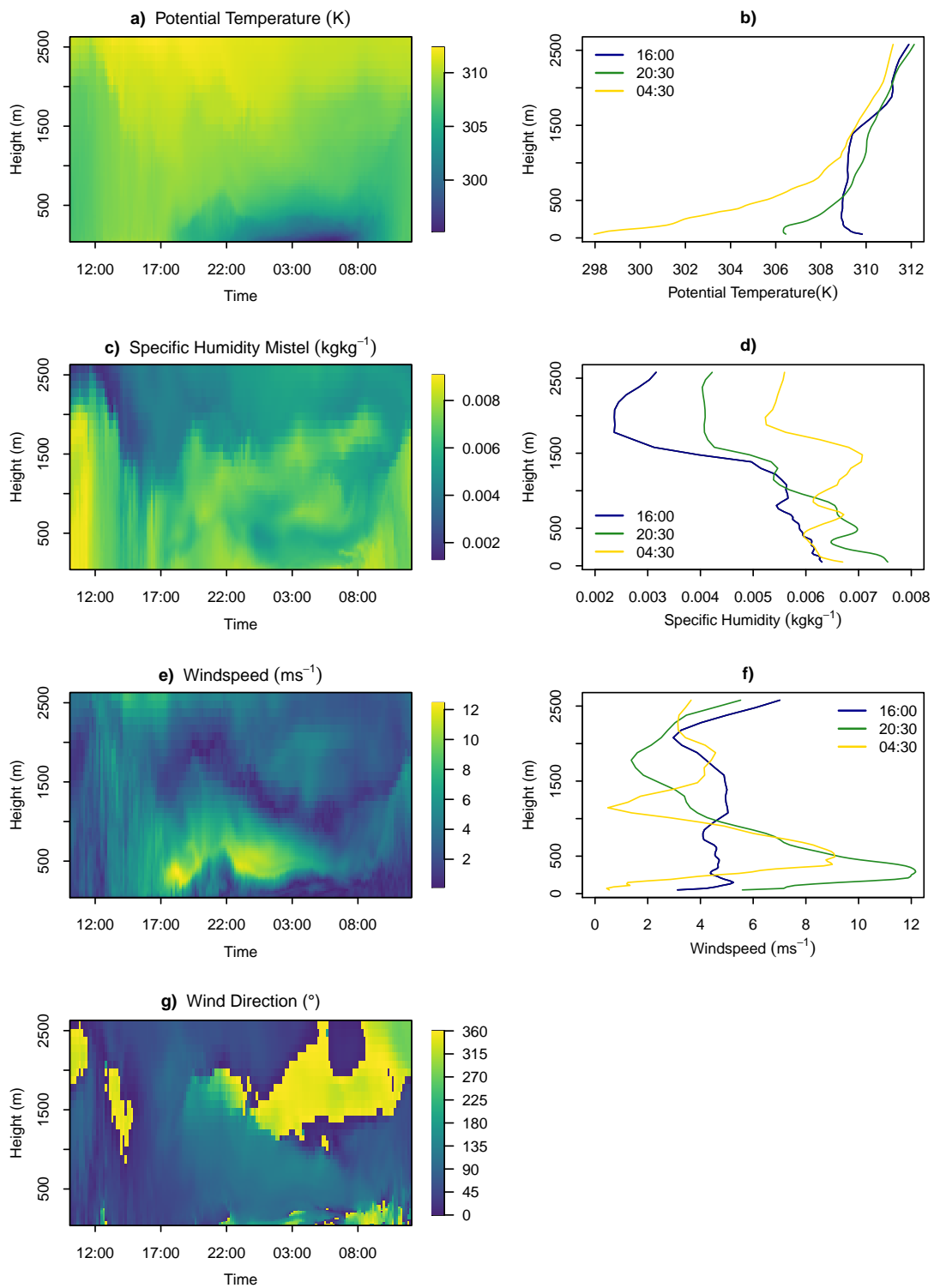


Figure B7: Simulated time height cross section of the Mistelbach. The profile was computed above a homogenous water surface. The time period shows the 26-hour interval of 07.25.2019 from 10:00 CET to 07.26.2019 12:00 CET. The height is referenced to 0 NN from the lowest point of the domain, the profile data starts at the respective height of the profile location. a), b) potential temperature in Kelvin, c), d) specific humidity in kgkg^{-1} , e), f) windspeed in ms^{-1} , g) wind direction in degree

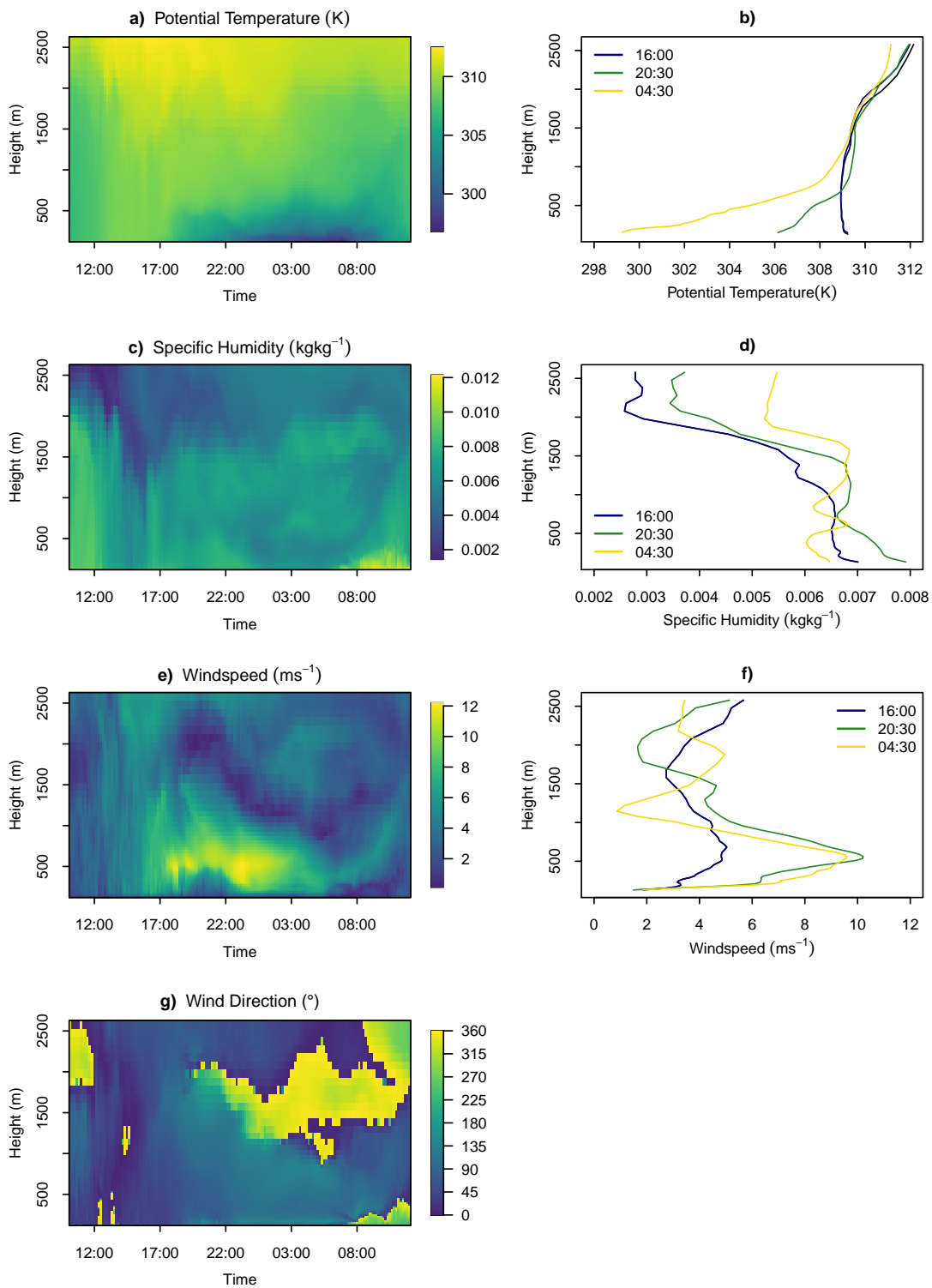


Figure B8: Simulated time height cross section of the very western part of Bayreuth. The profile was computed above a cropland surface. The time period shows the 26-hour interval of 07.25.2019 from 10:00 CET to 07.26.2019 12:00 CET. The height is referenced to 0 NN from the lowest point of the domain, the profile data starts at the respective height of the profile location. a), b) potential temperature in Kelvin, c), d) specific humidity in kgkg^{-1} , e), f) windspeed in ms^{-1} , g) wind direction in degree

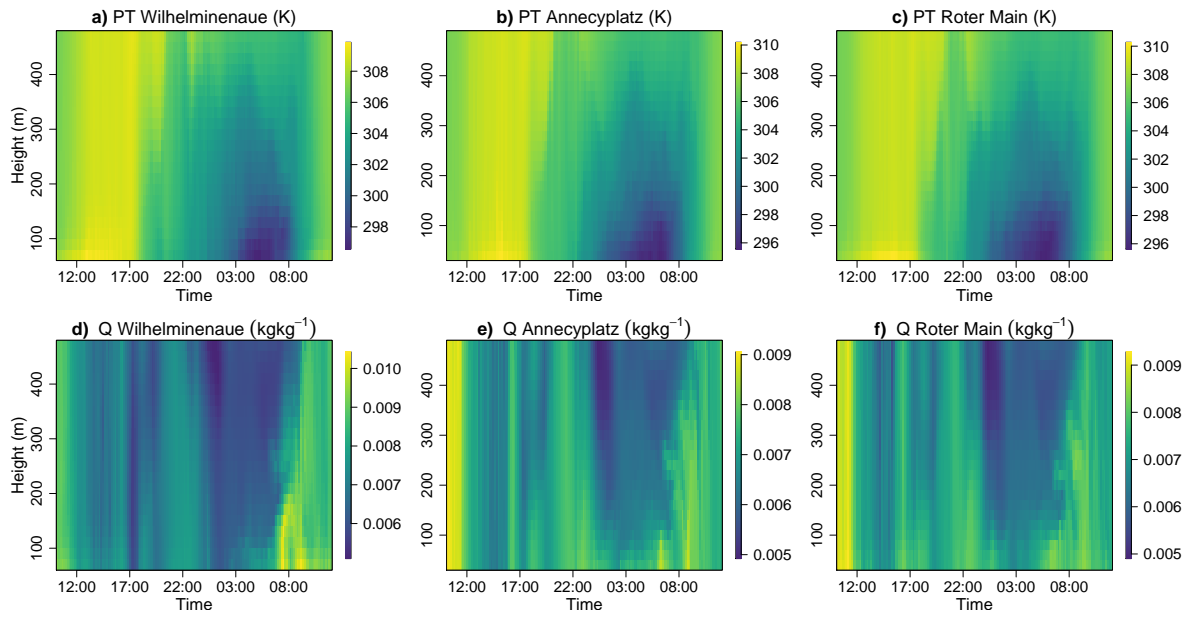


Figure B9: Simulated time height cross section of absolute profiles taken for scenario A. The profiles of a) - f) were computed above a water surface. a) potential temperature in Kelvin above the Wilhelminenaue, b) potential temperature in Kelvin above the flooded Annecy square, c) potential temperature in Kelvin above the Roter Main, d) specific humidity in kgkg⁻¹ above the Wilhelminenaue, e) specific humidity in kgkg⁻¹ above the flooded Annecy square, f) specific humidity in kgkg⁻¹ above the Roter Main. The time period shows the 26-hour interval of 07.25.2019 from 10:00 CET to 07.26.2019 12:00 CET. The height is referenced to 0 NN from the lowest point of the domain, the profile data starts at the respective height of the profile location.

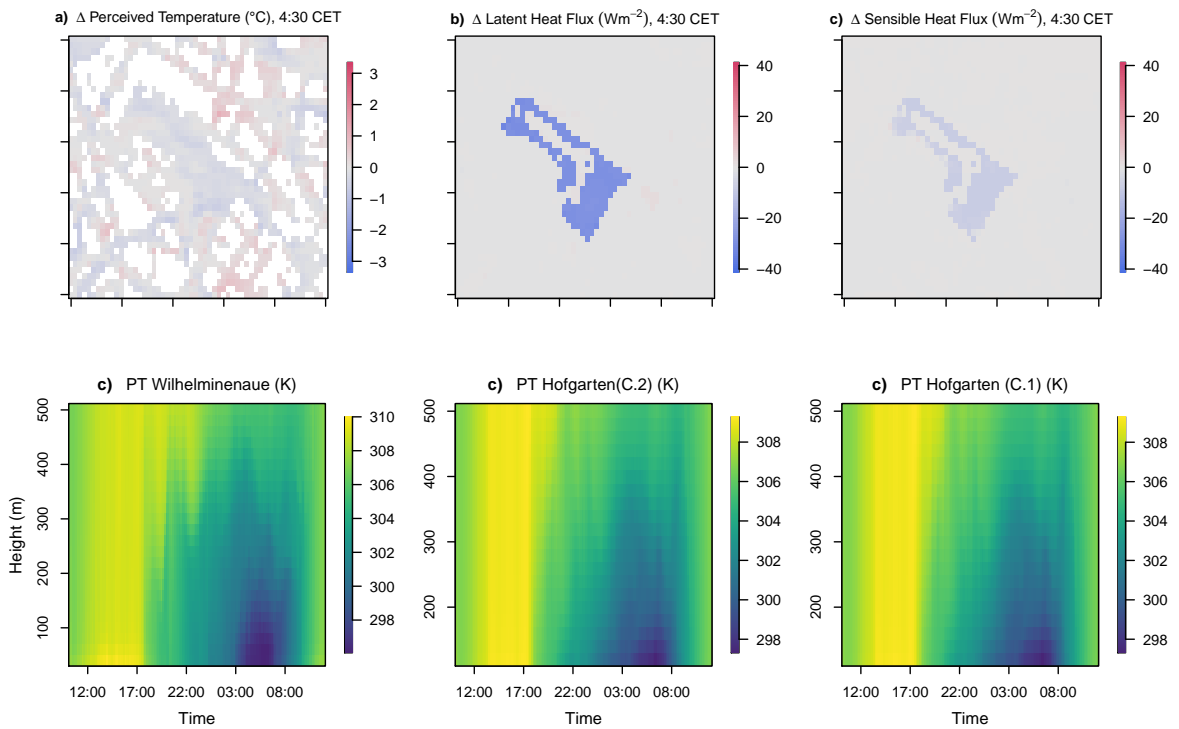


Figure B10: Differences of xy cross section data between scenario C.1 and C.2 and absolute profiles at 4:30 CET. For a)-c) C.1 is subtracted from C.2. a) perceived temperature in $^{\circ}\text{C}$, b) latent heat flux in Wm^{-2} , c) sensible heat flux in Wm^{-2} , d) potential temperature Wilhelminenaue in Kelvin, e) potential temperature Hofgarten,vegetated, in Kelvin, f) potential temperature Hofgarten, bare soil, in Kelvin. The cutout represents the map of the Hofgarten in Fig. 21.

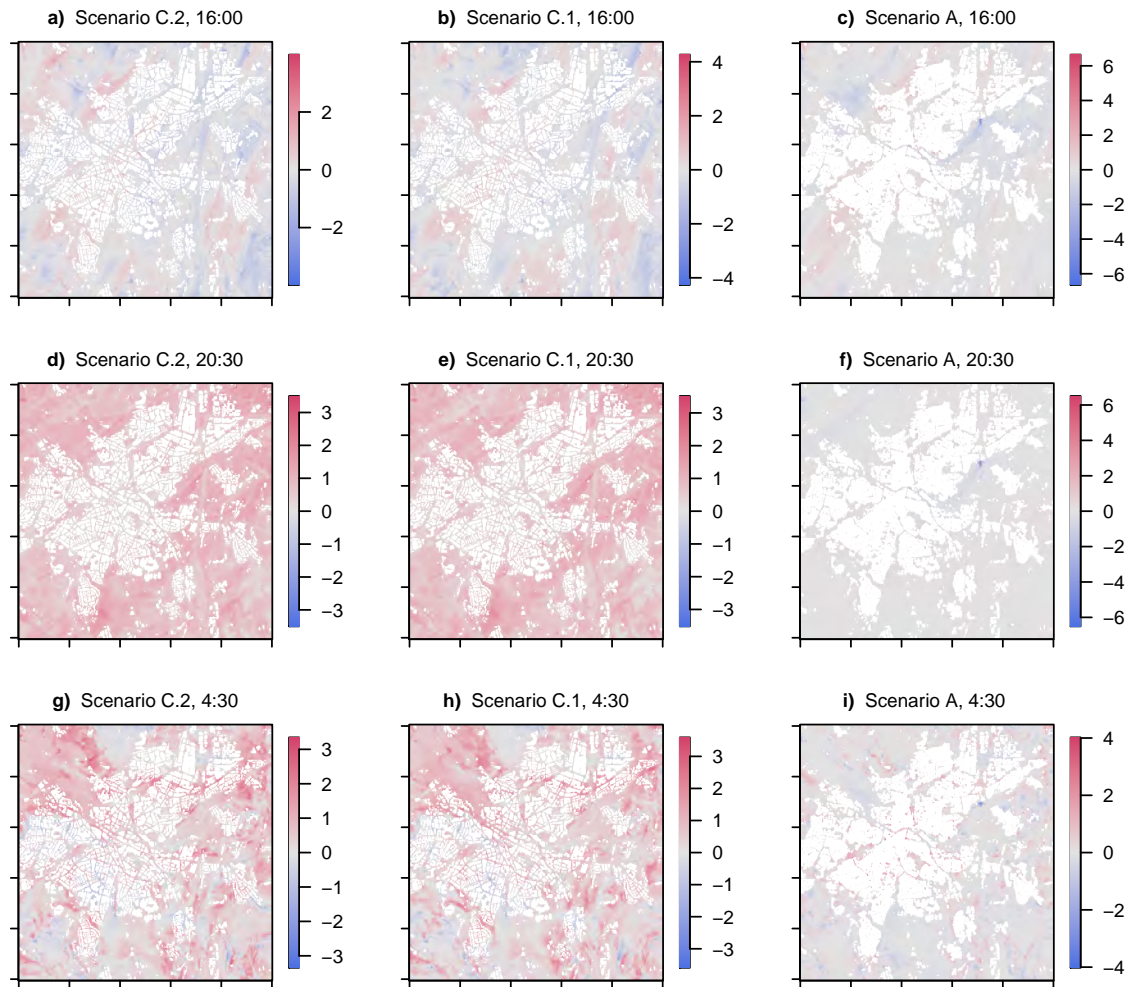


Figure B11: Difference in perceived temperature in °C between the scenario and the base run for the simulation times of 16:00, 20:30, and 4:30 CET. The difference results from the subtraction of the base run from the scenario. Scenario A describes the changes induced by increasing the amount of water surface, scenario C.1 involves the application of the drought stress including the Hofgarten, scenario C.2 involves the application of drought stress excluding the Hofgarten.

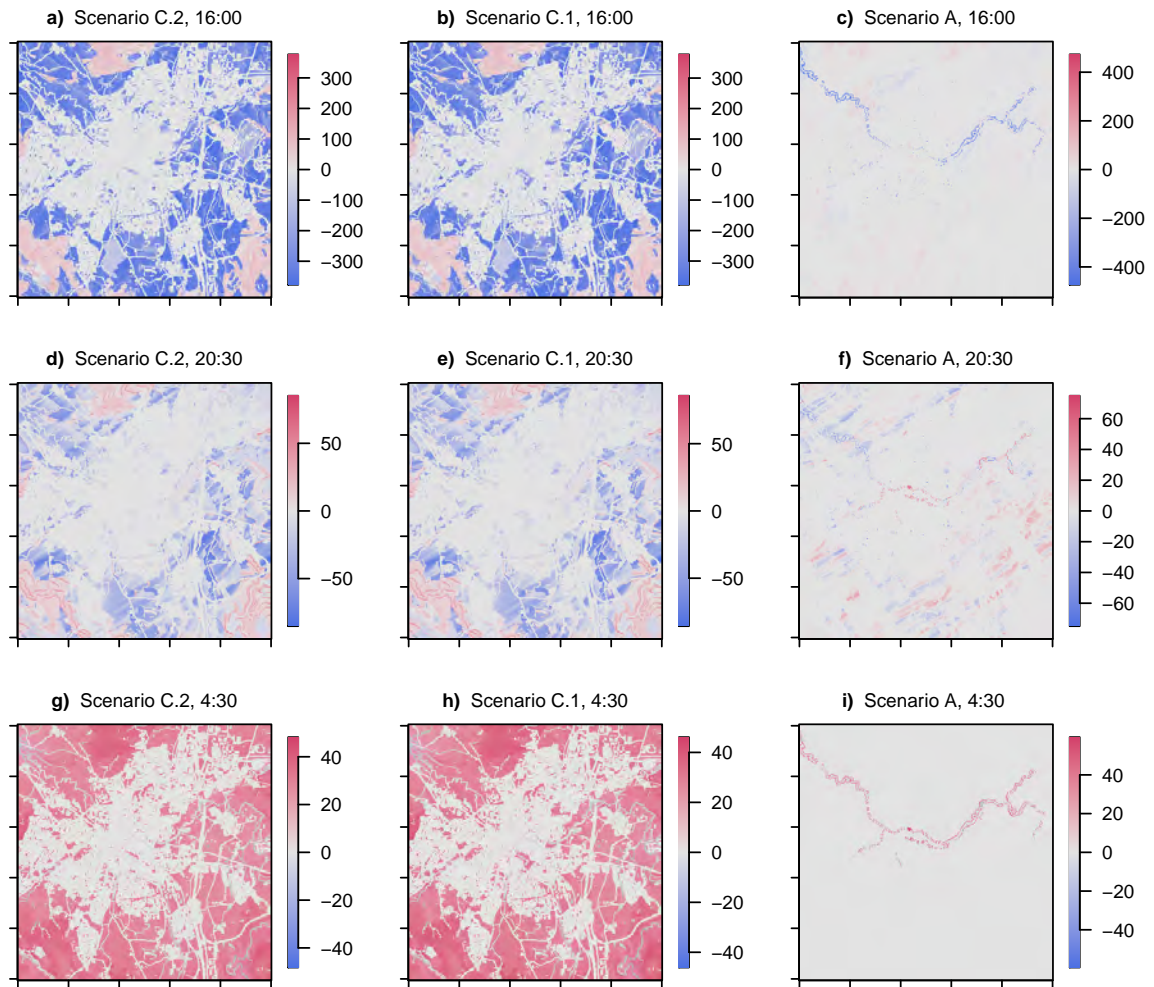


Figure B12: Difference of latent heat flux in Wm^{-1} between the scenario and the base run for the simulation times of 16:00, 20:30, and 4:30 CET. The difference results from the subtraction of the base run from the respective scenario.

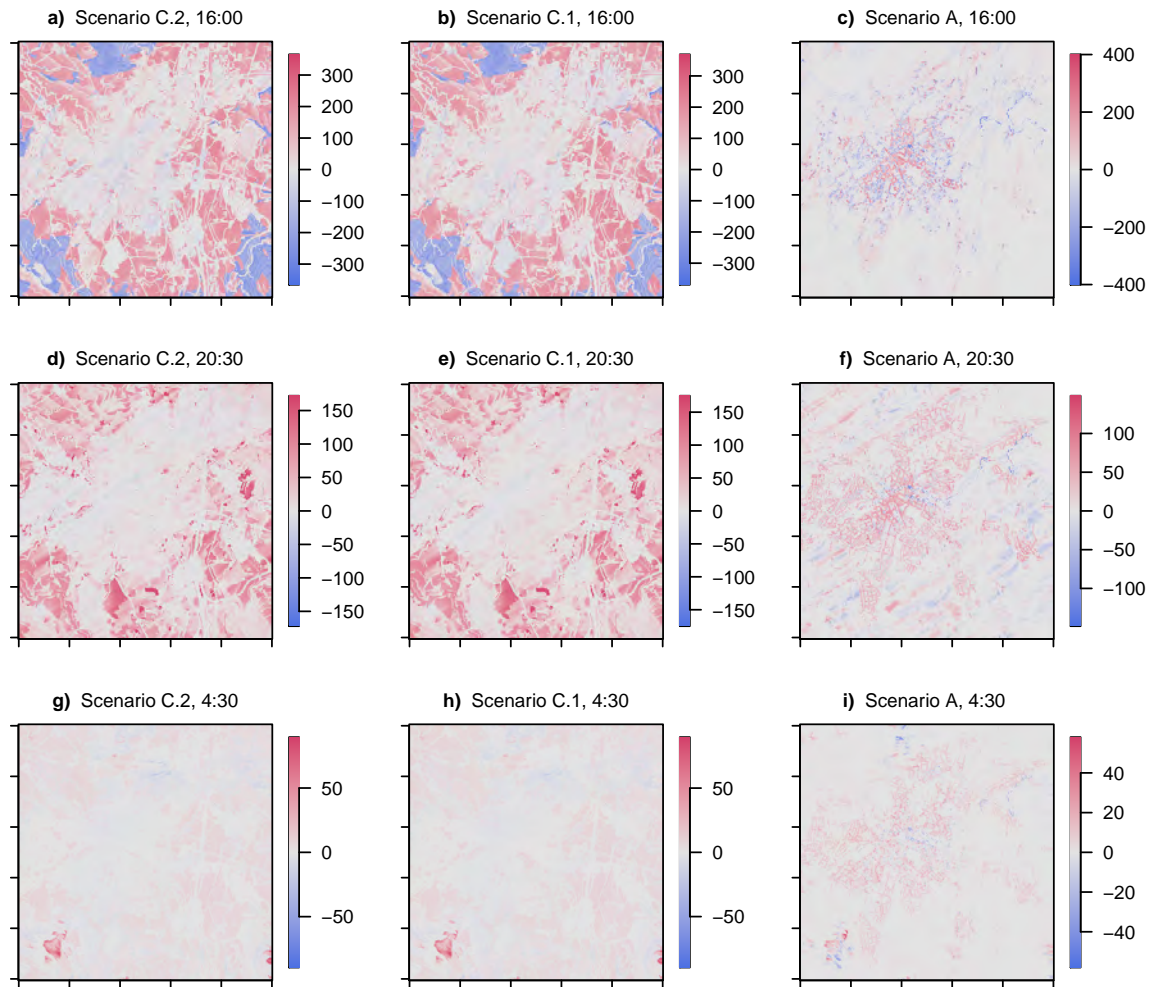


Figure B13: Difference of sensible heat flux in Wm^{-1} between the scenario and the base run for the simulation times of 16:00, 20:30, and 4:30 CET. The difference results from the subtraction of the base run from the respective scenario.

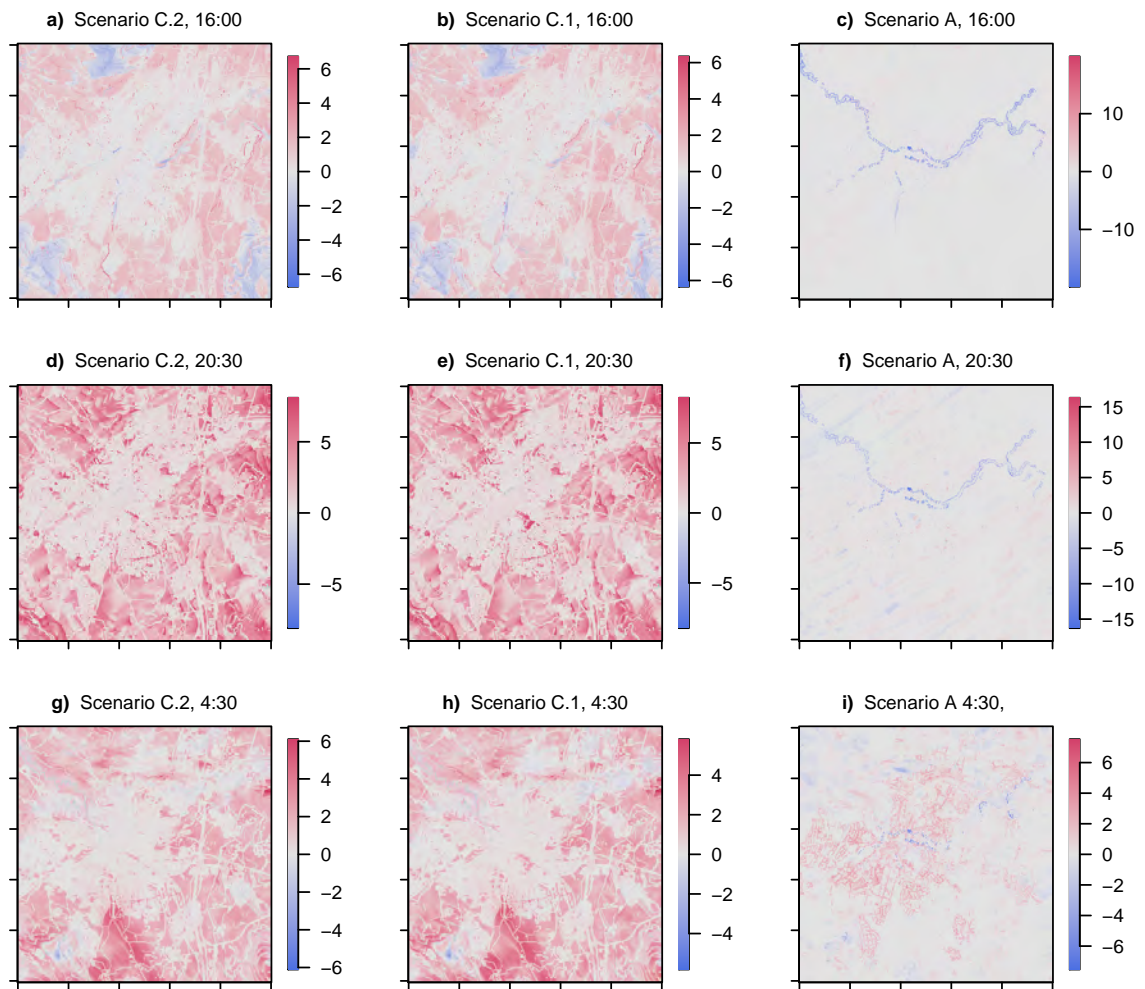


Figure B14: Difference of the potential temperature in Kelvin between the scenario and the base run for the simulation times of 16:00, 20:30, and 4:30 CET. The difference results from the subtraction of the base run from the respective scenario.

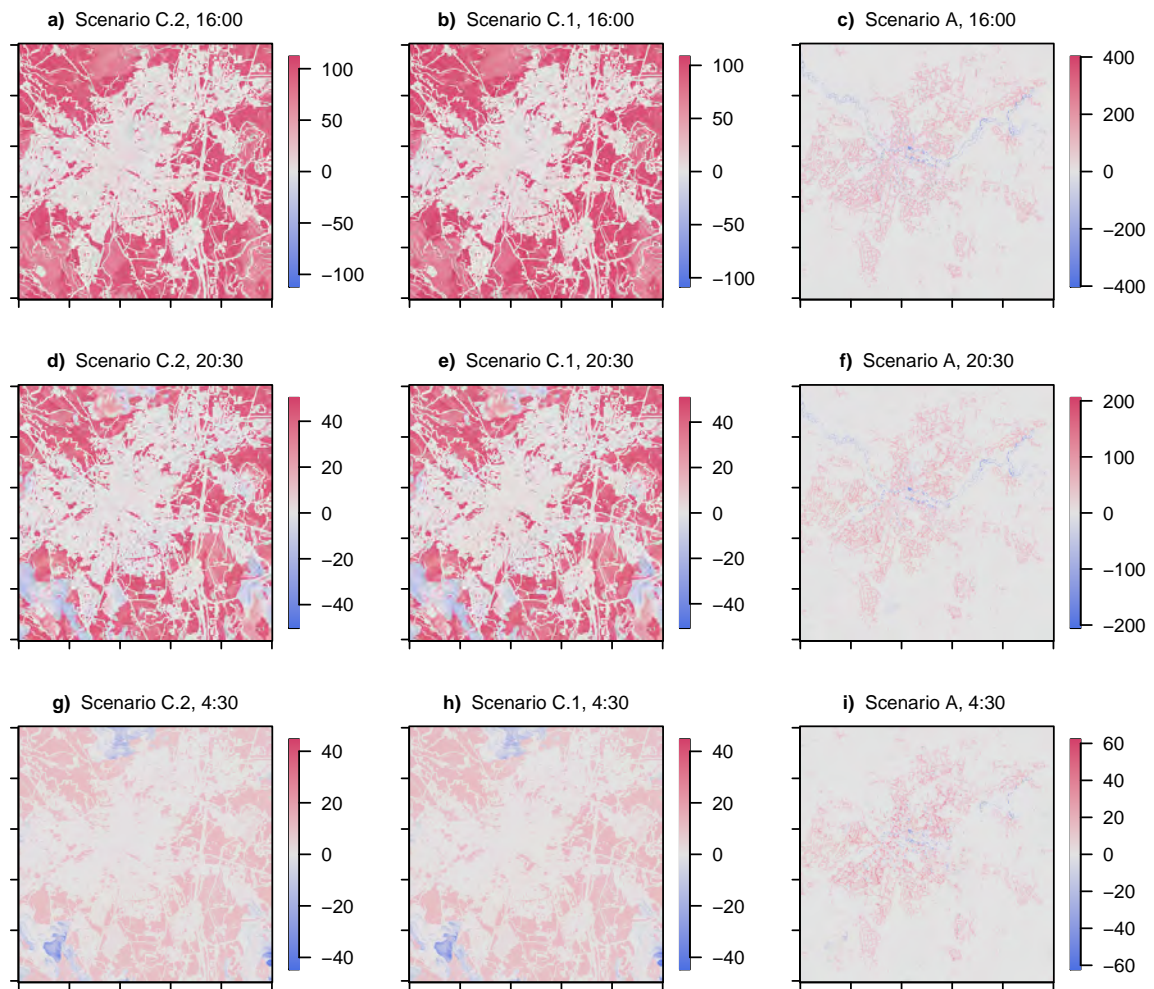


Figure B15: Difference of the outgoing longwave radiation flux in Wm^{-1} between the scenario and the base run for the simulation times of 16:00, 20:30, and 4:30 CET. The difference results from the subtraction of the base run from the respective scenario.

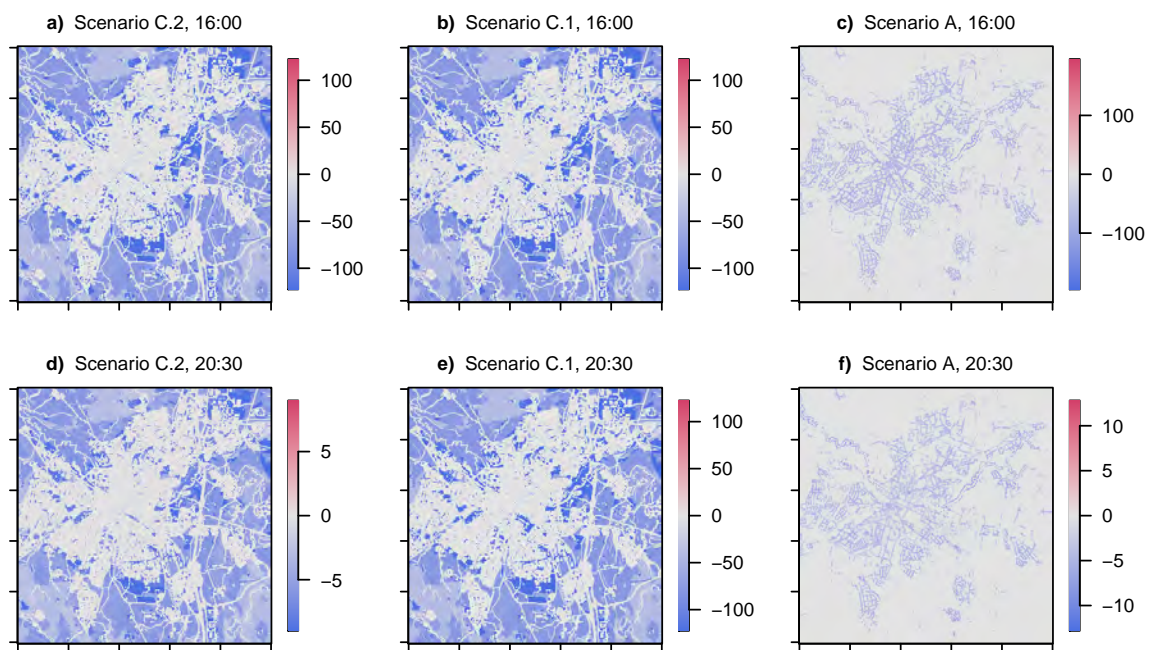


Figure B16: Difference of the outgoing shortwave radiation flux in Wm^{-1} between the scenario and the base run for the simulation times of 16:00, 20:30, and 4:30 CET. The difference results from the subtraction of the base run from the respective scenario.

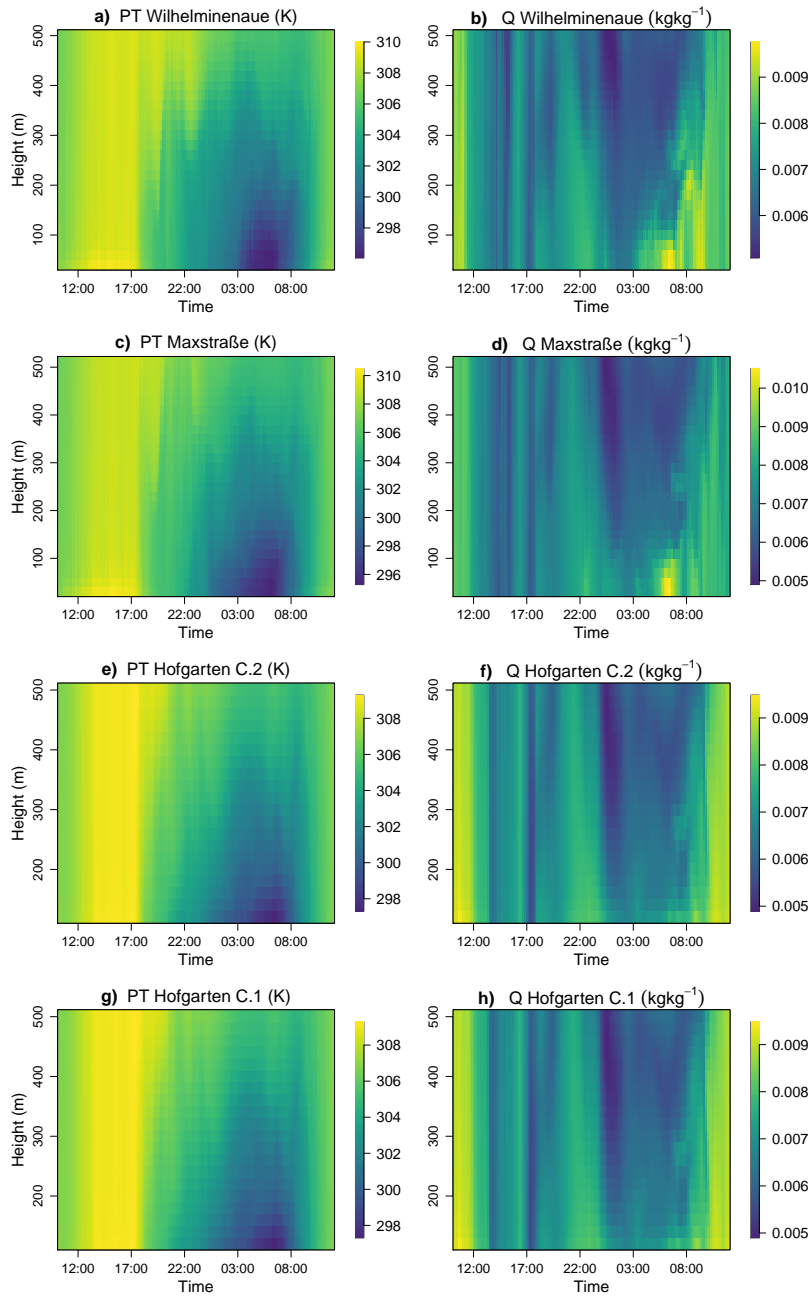


Figure B17: Simulated time height cross section of absolute profiles taken for scenario C. The profiles were taken from a homogenous surface, a) potential temperature in Kelvin above the Wilhelminenaue, b) specific humidity in kgkg^{-1} above the Wilhelminenaue, c) potential temperature in Kelvin above the Maxstraße, d) specific humidity in kgkg^{-1} above the Wilhelminenaue, e) potential temperature in Kelvin above the Hofgarten, f) specific humidity in kgkg^{-1} above the Hofgarten (short grass), g) potential temperature in Kelvin above the Hofgarten (bare soil), h) specific humidity in kgkg^{-1} above the Hofgarten (bare soil). The time period shows the 26-hour interval of 07.25.2019 from 10:00 CET to 07.26.2019 12:00 CET. The height is referenced to 0 NN from the lowest point of the domain, the profile data starts at the respective height of the profile location.

Declaration of Authorship

Hereby, I declare that I have authored the master thesis titled

"Mitigating heat accumulation in a mid-size urban area: Applying micrometeorological flow-resolving simulations to assess climate effects of urban planning measures"

independently based on my own work. All direct or indirect sources used are acknowledged as references. This thesis has not been published or previously submitted to any other examination board. This work does not claim to be complete.

Date, Leyla Sungur

